Sensitivity of simulated boundary-layer flow to the representation of forest canopies in complex terrain

John Tolladay

Thesis submitted to the University of Hertfordshire in partial fulfilment of the requirement of the degree of Doctor of Philosophy

July 2021

Thank you...

...to my supervisor Charles; my parents Pam and Keith; my friends Tayaab, Eheda, Ingrid, Dave C, Matt, Rachael, Dave G, Ryan and Chris; the fine members of 2E68 Ryan, Tracy, Gareth, Mike, Luke and even Tab; and to all of the undergraduate and post-graduate students and staff members who have supported me during my time at the University of Hertfordshire. Studying for this degree has been tumultuous at times but your motivation, help, support, kindness and distraction have helped me in many ways to get to where I now am.

Contents

Abstract

Complex terrain covers a large fraction of the land surface of the Earth. Due to the limited uses of steeply sloped terrain a lot of this is undeveloped and often covered with a canopy of trees or shrubs. Vegetation canopies are historically modelled using a roughness length at the surface, in line with Monin-Obukhov similarity theory. While this approach has been shown to be effective for shallow canopies such as crops and grasses, for deep canopies such as mature trees this method does not replicate the within and above canopy flows accurately. New approaches were developed in the 1990s to model the canopy explicitly and with a true vertical extent. These models account for the sink of momentum and turbulent kinetic energy within the canopy. In the present work, terms representing these effects are added to these equations in the open-source Weather Research and Forecasting model so that numerical simulations can be performed. This implementation of the canopy model is then tested against a benchmark, idealised case of measurements from a wind-tunnel experiment with an artificial canopy on a ridge with a two-dimensional profile. The model is found to provide significant improvements over simulations using an identical setup but with the canopy parameterised using increased roughness at the surface. The impact of resolution on the effectiveness of the model is also explored, with higher resolutions providing a more accurate representation of the flow over the forested ridge. The model is then applied to a real-world scenario using a case study of the flow over two parallel ridges that form a valley system in the area around Perdigão, Portugal. A 3-hour period during the night is simulated and in this case the canopy model still outperformed the surface roughness method. Many features of the flow were only reproduced properly by simulations using a canopy model. In particular the likelihood of recirculation in the lee of the ridges and the mean flow within the valley. Use of high resolution input data characterising properties and distribution of the canopy did not provide significantly better results than using lower resolution land use datasets with averaged canopy properties. The canopy model is shown to provide significantly better results than the surface roughness parameterisation but does require finer spatial and temporal resolution, leading to a higher computational cost. There is however scope for the implementation of the model that is used here to be improved to avoid instabilities at shorter time steps. When studying the flow over truly complex terrain covered in a canopy, it is difficult to disentangle the effect of the canopy from the effect of the terrain. Further experimental work is therefore suggested that could help to improve the understanding of canopy dynamics in complex terrain and also provide further benchmarks against which canopy models could be tested in numerical simulations. Please note that Chapters 3 and 4 are based on an article co-authored with my supervisor Charles Chemel and Chapter 4 was also co-authored by Robert Menke, who assisted with the processing of the lidar measurements. The author of this thesis carried out all simulations and analyses presented in these chapters as well as writing the text.

SECTION 1

Introduction

1.1 Forest canopies in complex terrain

Complex terrain, with features such as hills, ridges, valleys and mountains, accounts for almost 40% of the land surface of the Earth. Mountainous areas alone account for more than half of this coverage, with 26% of the global population living in these areas (Meybeck et al., 2001). The steep slopes and difficulties in accessing such terrain cause significant obstacles to construction. Some hilly terrain is used for grazing livestock but is rarely used for arable crop planting, unless sufficient flat terrain is available and the land can be terraced. Due to the limited uses of these areas, they are often left untouched and much more likely to be naturally vegetated. The lack of development on steeply sloped terrain can be seen clearly in Fig. 1, showing a photograph of the town of Riva del Garda and the surrounding area in the Italian Alps.

Figure 1: A photograph showing the town of Riva Del Garda, Italy and the surrounding area

Forest canopies (specifically areas with $> 10\%$ tree cover) make up 19% of the land surface of the Earth (Bastin et al., 2019a). This can range from sparse tree canopies in grassy or shrubby areas to dense woodland with closely packed large trees and an under-storey of shrubs. Given that tree cover is so prevalent in the landscape, understanding the effect that forested terrain has on the dynamics of the atmosphere is important. This is especially true when studying mesoscale and microscale phenomena, but could also play a part in larger scale phenomena. For example, some of the remaining rainforests and the large boreal forests in the taiga of the northern hemisphere cover huge areas.

Woodland cover has long been in decline worldwide as demand for wood has grown exponentially. Historically, large areas of trees were removed to be used for construction, fuel and even shipbuilding. In modern times a burgeoning global population led to a much greater need for wood in construction, furniture and fuel. There is also pressure to remove rainforest to create land for crops and livestock. However, governments and organisations worldwide are beginning to take deforestation seriously due to the impacts that it has on climate change and air quality.

The European Union has set a target to stop the loss of global forest cover by 2030 (COM(1998) 0649). The United Nations strategic plan for forests includes many goals, including halting deforestation, encouraging reforestation and afforestation and making current woodlands sustainable and resilient in the face of climate change. It also sets a target to increase the forested area of the world by 120 million hectares by 2030. Research suggests that ecosystems could support a 25% increase in forested area, equating to almost 1 billion hectares of potential woodland. Such an increase would provide an additional 200 gigatonnes of carbon storage once it reached maturity, around 25% of the current atmospheric carbon pool (Bastin et al., 2019b).

Whether these targets (or others set worldwide) can be met is a matter of politics but it seems clear that a large part of the land surface of the Earth will always be forested. Experimental studies have shown that interaction with a tall forest canopy can have significant effects on the flows present in complex terrain, as will be explored in Sect. 1.2. The representation of the surface interaction between the atmosphere and forested terrain is therefore important for numerical weather and climate prediction systems to give accurate results. Woodland canopies are rarely modelled explicitly in numerical weather prediction systems. Where they are modelled explicitly, little work has been done so far to test these models in forested and truly complex terrain (Fernando, 2010).

1.2 Experimental background

As an undisturbed flow meets the edge of a forest canopy, the wind speed below the height of the canopy is rapidly reduced as momentum is lost through interaction with the leaves, branches and stems of the trees. Above the canopy, there is nothing to reduce the momentum of the flow and so shear is produced at canopy top at the interface between the slower canopy flow and the faster above canopy flow, leading to Kelvin-Helmholtz instabilities. These instabilities develop in to

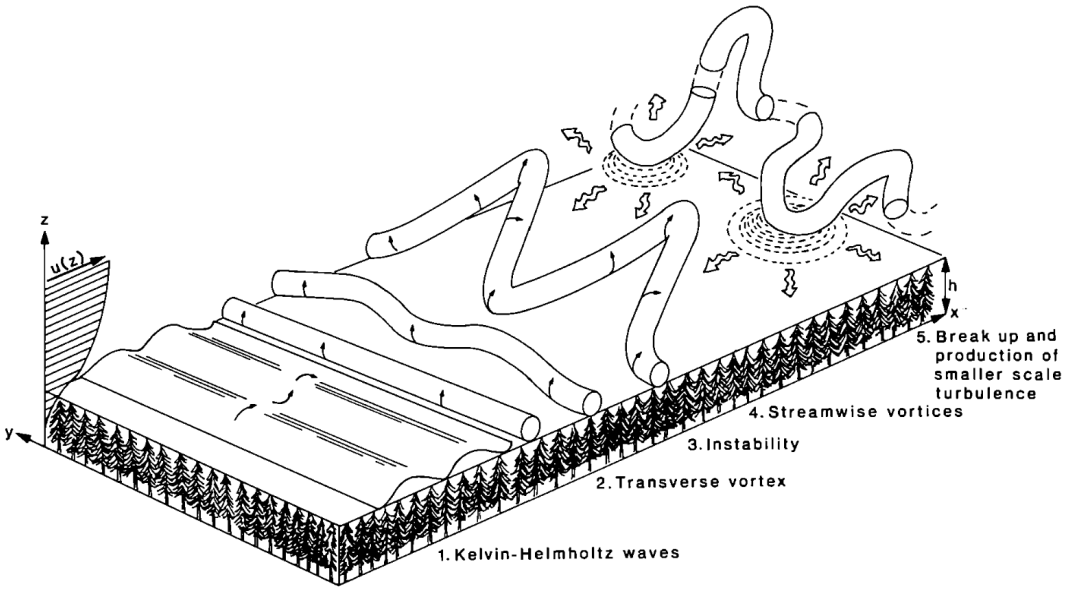

Figure 2: Diagram showing the formation of turbulence over a homogeneous forest canopy. An adaptation by Quine et al. (1995) of schematics from Finnigan and Brunet (1995)

vortices normal to the direction of the flow that roll over the top of the canopy. Further instabilities then distort these vortices aligning them in the stream-wise direction and eventually lead to more complex turbulence in a layer just above the canopy top. This turbulence can force gusts of wind down in to the canopy that are then dissipated by interaction with the canopy elements or draw the air and scalars out of the canopy in to the turbulent air above. A graphical representation of these processes can be seen in Fig 2. Over flat ground with homogeneous forest cover, a stable vertical profile of the mean stream-wise component of the wind develops.

Belcher et al. (2012) found that the distance over which the flow adjusts to a canopy edge is between 4.5 and $6L_c$, where $L_c = 1/(C_d a)$ is the inverse product of the leaf area density a (see Fig. 3 for an example) and a drag coefficient C_d. In a study of the flow over an artificial canopy in a wind tunnel, Raupach et al. (1987) measured the adjustment to occur over $10h_c$, where h_c is the height of the canopy. However, the adjustment length scale L_c has proven to be a more reliable scale for predicting the distance required for a flow to adjust to a forest canopy. The vertical length scale for turbulence generated near the canopy top was identified by Raupach et al. (1996) as $L_s = U_h/U_h'$, where U_h is the mean stream-wise velocity at canopy top and U_h' is the vertical gradient at the same location. This vertical length scale was found to be inversely proportional to the density of the canopies considered in the study. Measurements of the adjustment length for canopies of different densities are not generally available, but increasing canopy density was shown to significantly decrease the distance required for flow to adjust to a forest edge in numerical simulations by Dupont and Brunet (2008a). Using the density to calculate L_c has therefore proven a better predictor of the length scales of adjustment and turbulence around canopies than the canopy height.

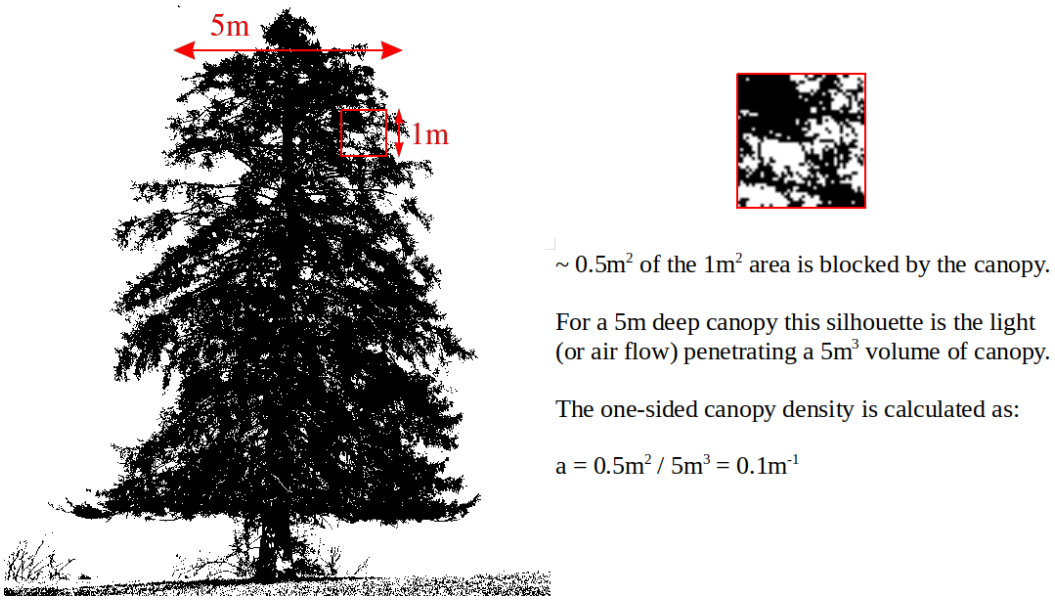

Figure 3: A simplified example of the calculation of leaf area density a. This is usually calculated over the entire canopy, rather than the simple example of a 1m^2 cross-section of the canopy used here. It can then be averaged horizontally and/or vertically, depending on the way in which it is to be used

Another feature of the flow as it interacts with a forest edge is an 'enhanced gust zone' (EGZ) that was identified by Raupach et al. (1987) in wind-tunnel observations over a canopy of nylon stalks. While the mean velocity profile adjusted smoothly to the canopy edge, gusts of wind with velocity almost twice that seen typically above the canopy were observed approximately 3 to 7 times the canopy height downstream near the top of the canopy. The enhanced gust zone was also identified in wind-tunnel experiments by Tischmacher and Ruck (2013) at a distance of 1.5 to 4 tree heights downstream of the leading edge. Gusts were injected in to the flow upstream of a canopy of artificial conifers (polystyrene stems each mounted with a crown) and the horizontal deceleration of this high-speed air induced vertical ejection in to the faster moving air above the canopy. This process was found to generate a vortex that moves downstream over the top of the canopy. As this vortex proceeds downstream it enhances intrusion of high-momentum air from the gust down in to the canopy. The processes leading to increased turbulence at canopy top may therefore be more complex than a pure Kelvin-Helmholtz instability, at least within close proximity to the canopy edge under gusty conditions. The canopy density of the two artificial canopies used in these experiments were $11.28\,\text{m}^{-1}$ and $22.73\,\text{m}^{-1}$ for Raupach et al. (1987) and Tischmacher and Ruck (2013), respectively. The EGZ was therefore 0.4 to $0.93L_c$ downstream of the canopy edge for the former and 0.94 to $2.5L_c$ downstream for the latter. For these two experiments it does not appear that either L_c or h_c provide a suitable length scale for predicting the distance to the EGZ, but the two canopies used were of different scale and morphology and exposed to different flows. However, predicting the length scales of flow interaction using any single quantity is highly ambitious given the drastic differences between one forest canopy and another.

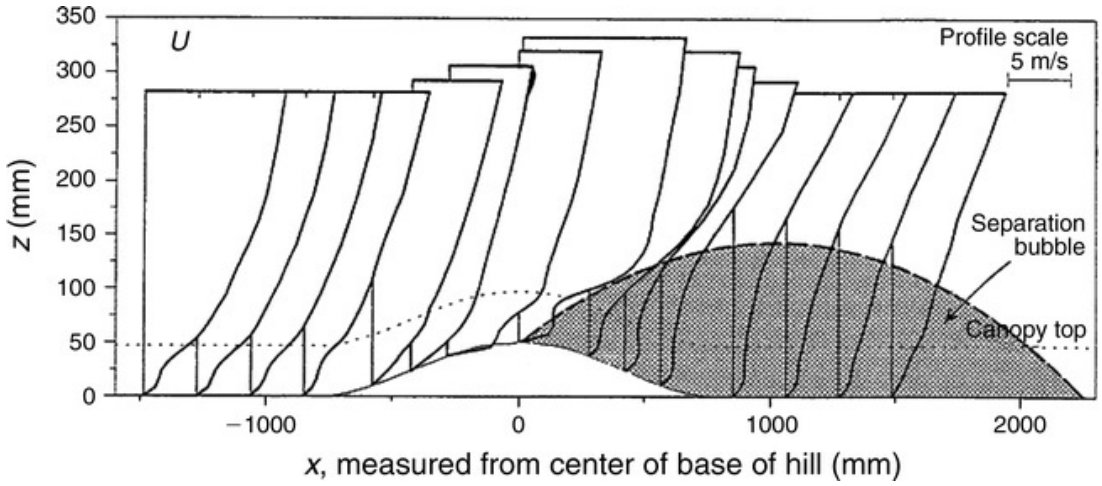

Figure 4: An adaptation by Belcher et al. (2008) of a figure showing vertical profiles of mean stream-wise velocity from the wind-tunnel experiment of Finnigan and Brunet (1995). The shaded region downstream of the hill marks the separation bubble, where recirculating flows are occurring

The constant vertical profile of mean stream-wise velocity that develops over flat forested terrain becomes distorted where the flow encounters a forested hill. On the leading slope of the hill a negative stream-wise pressure gradient is present within the canopy that leads to immediate acceleration of the within canopy flow. The flow above the canopy continues to decelerate upstream of the hill until a point after the pressure gradient becomes negative. This process reduces the inflection at the canopy top to the point where the profile becomes more like that seen in a typical boundary layer over a smooth surface. The stream-wise flow within the canopy reaches maximum velocity a short distance upstream of the top of the hill where the pressure gradient within the canopy is most negative and begins to decelerate. Conversely, the flow above the canopy reaches maximum speed-up above the top of the hill and this leads to a strengthening of the canopy inflection at the hill-top (Finnigan and Brunet, 1995). The increased shear this produces near the top of the canopy leads to greater instability and a turbulent wake reminiscent of a mixing-layer forms downstream of the hill. Such a wake would also be seen over flat forested terrain except the lower portion is absorbed as it descends in to the canopy. Near the peak of a hill the shear at canopy top is increased and the canopy then descends with the terrain on the lee slope. A wake with much greater vertical extent can then form above the canopy and spread vertically downstream above and below the height of the hill-top.

Where a hill is steep enough the pressure minimum that is generated immediately downstream of the hill-top can lead to flow separation and recirculation, where the flow can reverse and move back up the lee slope of the hill. An example of this from the wind-tunnel experiment of Finnigan and Brunet (1995) is shown in Fig. 4. Hills covered with a forest canopy create a stronger pressure minimum and so flow separation can occur over shallower hills than those with a smoother surface. The recirculation zone was studied in more detail in water flume experiments carried out by Poggi and Katul (2007) for a flow over a train of shallow hills covered with an artificial canopy representing

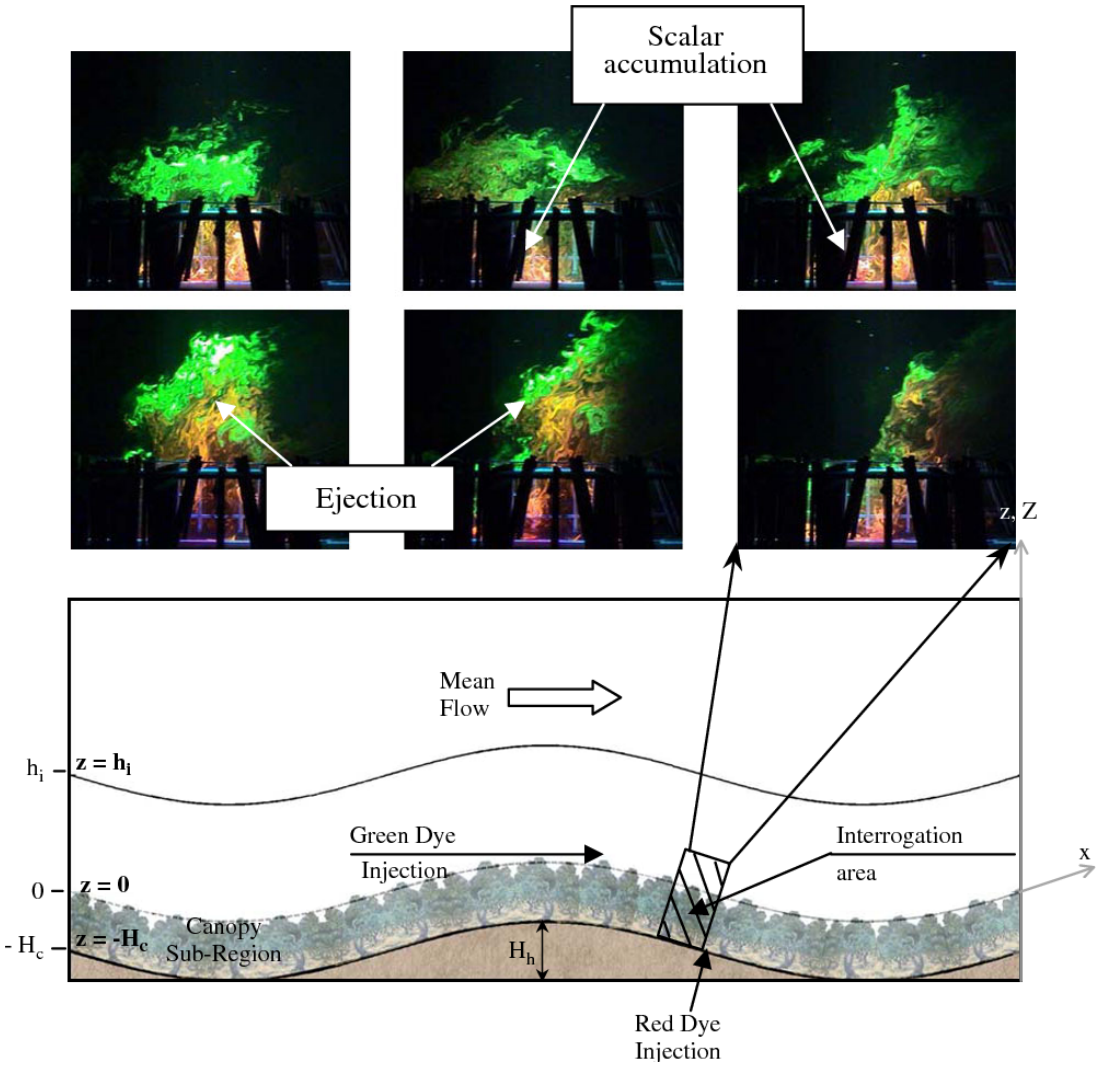

Figure 5: A figure from Poggi and Katul (2007) showing images from the recirculation region taken at $1\,\mathrm{s}$ intervals with a graphical representation of the experimental setup beneath. The green dye is injected above the canopy upstream of the imaged area. The red dye is injected downstream near the ground but is moved up the slope by recirculating flow and periodically ejected from the top of the canopy

a hardwood forest. The reversed flows occurring within the canopy were found to be intermittent in nature and thus not characterised by a classical rotor structure. It was also found that scalars built up within the canopy in the recirculation zone before being ejected from the canopy top over short time scales, as illustrated in Fig. 5. This indicates that variations in the pressure field over short time scales have a more significant impact in the recirculation zone than the mean adverse pressure gradient.

Finnigan and Hughes (2008) investigated the effects of stable conditions on the flow over a shallow hill covered with a canopy by heating the base of the wind tunnel in which they performed their experiment. Figure 6 shows a comparison between mean velocities measured in this experiment with the heating turned on or off, corresponding to stable or neutral conditions, respectively. At a free stream wind speed of $0.3\,\mathrm{m\,s^{-1}}$, down-slope gravity flows were found to form within the canopy

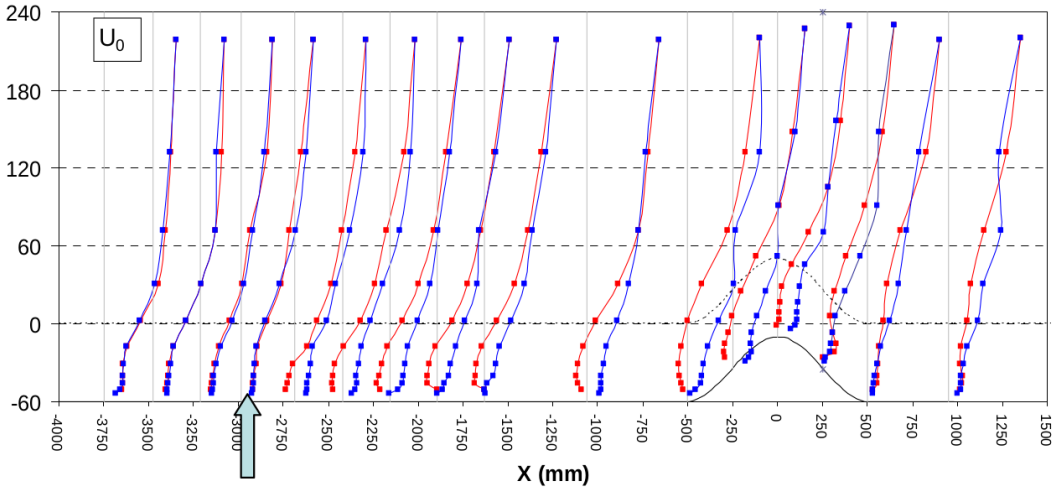

Figure 6: Comparison of mean velocity profiles normalised by wind-tunnel free-stream velocity ($U_0 = 0.3\,\mathrm{ms}^{-1}$, left to right) for neutral (blue profiles) and stable (red profiles) conditions from Finnigan and Hughes (2008). The arrow marks the upwind penetration of reversed flows caused by the down-slope gravity flow at the hill for the stable case. The y-axis of this plot represents the vertical dimension, also in units of millimetres. The hill is marked with a solid line centred at $X = 0$ and the canopy height is marked with a dotted line

on both sides of the hill. On the windward side, the flow within the canopy was opposing the mean flow above to a position nearly $12L$ upstream of the hilltop, where L is the half-height length scale of the hill. The down-slope current on the lee side of the hill was less pronounced but stopped any reversed flows from occurring in the region where recirculation occurred under neutral conditions. In a study of the flow over an area of forest canopy on a sloping sub-alpine site Burns et al. (2011) also found down-slope gravity flows were common in stable conditions, occurring for 90% of the time during the night. Flows up and down the slope were found to be equally likely during the day time. Under near-neutral and unstable conditions, when the air above the canopy was flowing down the slope, flow up the slope was measured within the canopy. These up-slope flows were found to occur only in locations where a canopy was present. This study also looked at scalar mixing and found that scalars tended to build up near the ground where the surrounding canopy was dense, with a leaf area index ≈ 4. Where the leaf area index is the vertically integrated leaf area density over the full height of the canopy.

Experimental data has clearly shown that forested terrain can substantially modify the dynamics of flows within close proximity to the canopy. Developing an understanding of canopy flows enables professionals in the forestry and woodland management industries to better predict and ameliorate potential wind damage to trees. The increased turbulence over forested terrain, the tendency for flow recirculation and production of strong gusts of wind are also important factors to be taken in to account when selecting sites for wind farms that depend on near-surface flows. Modification of processes such as drainage flows and flow recirculation by a canopy have also led air quality researchers to consider canopies and their effect on scalar distribution over forested complex terrain.

Numerical weather prediction systems are widely used to predict such flows and replicating canopy dynamics in these systems is an active area of research. The methods used by these numerical models are outlined in Sect. 2.1, with methods relating to the representation of a forest canopy given in Sect. 2.2 and the canopy model that was used herein explained in Sect. 2.2.4.

The implemented canopy model is initially used in Sect. 3 to confirm that the model provides sensible results and improves upon the default methods when used to reproduce a benchmark wind-tunnel experiment. An investigation in to the sensitivity of the model to horizontal resolution is also provided for neutral flow over a two-dimensional ridge for the first time. This wind-tunnel experiment is scaled up so that the forested ridge was of a more realistic size. However, the resolutions used are still much higher than those used in simulations of real-world case studies. The overall aim of this thesis is to determine whether the canopy model can still provide benefits over default methods when used in simulations of a larger scale with real complex topography. In such cases the vertical and horizontal resolutions are constrained by the overall size of the area being simulated and the complexity of the terrain, respectively. Simulations of a real-world case study for a semi-idealised ridge are presented in Sect. 4 using a range of methods to represent the canopy and using coarser resolutions that are closer to those commonly used in weather simulations. Further discussion about these works and their implications, along with concluding remarks, are then given in Sect. 5.

SECTION 2

Modelling flows over forested terrain

2.1 Turbulence closures for numerical weather prediction

2.1.1 Reynolds-averaged Navier-Stokes equations

The Navier-Stokes (NS) equations were first derived by Claude-Louis Navier in the early 19th century (Navier, 1821, 1827). Navier expanded upon the work of Leonhard Euler, who had previously derived the Euler equation of motion for non-viscous fluids. Experimental data had shown that viscosity played a significant role in the behaviour of fluids and could not be ignored if the dynamics of a fluid was to be predicted accurately. Navier was the first to include viscosity in the theory in a mathematically rigorous way. It is not clear whether George Gabriel Stokes derived the same equations independently (Stokes, 2009) but he performed many experiments to test the theory scientifically and so his name has also been attached to the equations. If air is assumed to be an incompressible Newtonian fluid then the NS equations can be written using Einstein summation notation as

$$\frac{\partial u_i}{\partial x_i} = 0, \tag{1}$$

$$\frac{\partial u_i}{\partial t} + u_j \frac{\partial u_i}{\partial x_j} = \nu \Delta u_i - \frac{1}{\rho} \frac{\partial p}{\partial x_i}, \tag{2}$$

where u_i is the component of the velocity vector in the direction x_i, t is time, ν is the kinematic viscosity, ρ the density and p is the pressure. These equations are non-linear partial differential equations and are therefore difficult to solve for most problems and in some cases entirely unsolvable. Even without a complete solution, the equations allow for a fluid to be modelled and understood in a way that would not be possible otherwise. The inertia of a fluid under convective acceleration gives rise to chaotic behaviour that is collectively described as turbulence. Turbulent structures can exist from molecular scales up to the size of the container that a fluid is within. This makes direct numerical simulation incredibly difficult even for small containers but currently impossible in the case of the atmosphere.

Due to the impracticalities of modelling every scale of motion, the NS equations are often averaged over time using a decomposition first proposed by Osborne Reynolds to give the Reynolds-averaged Navier-Stokes (RANS) equations (Reynolds, 1895). Reynolds decomposition is a process

of separating a time-averaged component of the flow from the fluctuations around this value, in such a way that the time average of the fluctuations is assumed to be equal to zero. After the Reynolds decomposition has been applied, the RANS form of equation 2 can be written as

$$\frac{\partial \bar{u}_i}{\partial t} + \bar{u}_j \frac{\partial \bar{u}_i}{\partial x_j} = \nu \frac{\partial^2 \bar{u}_i}{\partial x_j x_j} - \frac{1}{\rho}\frac{\partial \bar{p}}{\partial x_i} - \frac{1}{\rho}\frac{\partial \overline{u_i' u_j'}}{\partial x_j}, \tag{3}$$

where $\bar{u}_i$ and $\bar{p}$ are the time averaged components of velocity and pressure respectively. This decomposition introduces an additional non-linear term in the equations $\partial \overline{u_i' u_j'}/\partial x_j$ that is formed from the velocity fluctuations in the i and j directions and is commonly called the Reynolds stress term R_{ij}. This term must be modelled for the RANS equations to be solved and many such turbulence closures have been devised for a range of applications. Those that have been used more commonly for atmospheric applications are discussed below.

2.1.2 Eddy viscosity

The first attempt to resolve the closure problem was made by Joseph Valentin Boussinesq, who introduced the concept of an eddy viscosity to model the momentum transfer by turbulent eddies within a fluid (Boussinesq, 1877). The concept of eddy viscosity is similar to that of molecular viscosity, whereby momentum can be transferred through a fluid by molecular motions within. The Boussinesq hypothesis is that the Reynolds stress tensor is proportional to the mean strain rate tensor multiplied by an eddy viscosity, such that

$$-\overline{u_i' u_j'} = \nu_t \left(\frac{\partial \bar{u}_i}{\partial x_j} + \frac{\partial \bar{u}_j}{\partial x_i} \right) - \frac{2}{3} k \delta_{ij}, \tag{4}$$

where ν_t is the kinematic turbulence eddy viscosity, $k = \overline{u_i' u_i'}/2$ is the turbulence kinetic energy (TKE) and δ_{ij} is the Kronecker delta. By using this approximation the Reynolds stress tensor can be related to the mean strain rate tensor and hence the velocity gradient. The resulting form of equation 3 is then

$$\frac{\partial \bar{u}_i}{\partial t} + \bar{u}_j \frac{\partial \bar{u}_i}{\partial x_j} = \frac{\partial}{\partial x_j} \left((\nu + \nu_t) \frac{\partial \bar{u}_i}{\partial x_j} \right) - \frac{1}{\rho} \left(\frac{\partial \bar{p} + \partial \frac{2}{3} \rho k}{\partial x_i} \right). \tag{5}$$

The turbulent eddy viscosity must then be calculated and is often derived from dimensional arguments by combining velocities and length and time scales of turbulence to arrive at the units of viscosity. In this formulation the eddy viscosity is also assumed to be isotropic and scalar, but this is not the case in many situations such as flows with strong vorticity, anisotropic flows with secondary motions and flows where separation is occurring. For attached flows, a simple calculation for the eddy viscosity was devised by Ludwig Prandtl by introducing the concept of a turbulence mixing length l_m (Prandtl, 1925). This mixing length is assumed to be proportional to the distance to the boundary to which the flow is attached and used to calculate the eddy viscosity as

$$\nu_t = \frac{\partial u}{\partial y} l_m^2, \tag{6}$$

where u is the velocity in the stream-wise direction and y is the direction normal to the boundary. While this method performs well with attached flows, it is still not applicable to separated flows.

Further development of the Boussinesq hypothesis has led to various methods of calculating the eddy viscosity. The Spalart-Allmaras model uses a single transport equation that is solved for the kinematic eddy turbulent viscosity. This model will not be discussed in detail here as it was designed for engineering applications and does not perform well in free-shear flows. The second order $k-\epsilon$ and $k-\omega$ models are much more commonly used for atmospheric purposes. Each of these uses two equations to calculate the TKE k and the rate of dissipation of TKE ϵ (or ω). For the $k-\epsilon$ method we have

$$\frac{\partial k}{\partial t} + \frac{\partial (k u_i)}{\partial x_i} = \frac{\partial}{\partial x_j}\left(\frac{\nu_t}{\sigma_k}\frac{\partial k}{\partial x_j}\right) + 2\nu_t E_{ij} E_{ij} - \epsilon, \tag{7}$$

$$\frac{\partial \epsilon}{\partial t} + \frac{\partial (\epsilon u_i)}{\partial x_i} = \frac{\partial}{\partial x_j}\left(\frac{\nu_t}{\sigma_\epsilon}\frac{\partial \epsilon}{\partial x_j}\right) + C_{1\epsilon}\frac{\epsilon}{k} 2\nu_t E_{ij} E_{ij} - C_{2\epsilon}\frac{\epsilon^2}{k}, \tag{8}$$

where E_{ij} represents the rate of deformation in the corresponding direction, eddy viscosity $\nu_t = C_\nu k^2/\epsilon$ and σ_k, σ_ϵ, $C_{1\epsilon}$, $C_{2\epsilon}$ and C_ν are constants. Despite the extra computational cost of calculating these two new transport equations, this model is widely used for atmospheric numerical simulations due to being effective at modelling free-shear flows and recirculating or separated flows. The cost of this method is sometimes reduced by using only local properties of the flow to calculate the rate of dissipation ϵ, commonly called a one-and-a-half order closure. The $k-\omega$ closure similarly uses two transport equations for TKE and the rate of dissipation thereof and is also designed more for engineering applications of wall bounded flows. Due to the success of each method under different conditions, the shear stress transport (SST) model was developed to apply the $k-\epsilon$ closure in regions of free-shear flow and then switch to the equations of the $k-\omega$ closure when closer to the boundaries (Menter, 1994).

2.1.3 Sub-grid-scale turbulence models

With the availability and rapid advancement of computational numerical simulations, it was possible to simulate flows on grids that could resolve smaller and smaller scales of turbulence explicitly. Joseph Smagorinski proposed that only turbulent motions with length scales smaller than the resolution of a simulation required modelling when the most energetic eddies present within a flow are being resolved (Smagorinski, 1963). A method of modelling only turbulence with length scales smaller than the resolution of the simulation was devised, now commonly called sub-grid-scale turbulence modelling. The smallest scales of turbulence are eliminated from the calculations of the NS equations through a process of low-pass filtering, but the stress produced by these sub-grid-scale (SGS) motions are

still modelled using an eddy viscosity. More recently this scale depends on the cube root of the grid cell volume $\sqrt[3]{\Delta x \Delta y \Delta z}$ but Smagorinski (1963) relied only on the horizontal grid size to calculate the eddy viscosity as

$$\nu_t = \Delta x \Delta y \sqrt{\left(\frac{\partial u}{\partial x}\right)^2 + \left(\frac{\partial v}{\partial y}\right)^2 + \frac{1}{2}\left(\frac{\partial u}{\partial y} + \frac{\partial v}{\partial x}\right)^2}, \tag{9}$$

where u and v are the horizontal components of the wind vector and x and y are the respective dimensions. Numerical simulations that utilise this method of resolving the most energetic turbulent structures and modelling only the viscosity caused by sub-grid-scale motions are referred to as large eddy simulations (LES). The filtered equivalent of equation 2, where an over-bar represents a filtered quantity is

$$\frac{\partial \bar{u}_i}{\partial t} + \frac{\partial \overline{u_i u_j}}{\partial x_j} = -\frac{1}{\rho}\frac{\partial \bar{p}}{\partial x_i} + \nu \frac{\partial}{\partial x_j}\left(\frac{\partial \bar{u}_i}{\partial x_j} + \frac{\partial \bar{u}_j}{\partial x_i}\right). \tag{10}$$

The term $\overline{u_i u_j}$ requires knowledge of the unfiltered velocity field and must therefore be modelled. Leonard (1975) achieved this by splitting the term such that $\overline{u_i u_j} = \tau_{ij} + \bar{u}_i \bar{u}_j$, where τ_{ij} is the 'residual' stress tensor. By splitting this term the filtered NS equations can be written in the form

$$\frac{\partial \bar{u}_i}{\partial t} + \bar{u}_j \frac{\partial \bar{u}_i}{\partial x_j} = -\frac{1}{\rho}\frac{\partial \bar{p}}{\partial x_i} + \nu \frac{\partial}{\partial x_j}\left(\frac{\partial \bar{u}_i}{\partial x_j} + \frac{\partial \bar{u}_j}{\partial x_i}\right) - \frac{\partial \tau_{ij}}{\partial x_j}. \tag{11}$$

All of the terms which still require closure are now contained within τ_{ij} and can be decomposed in to three terms representing the sub-grid-scale, larger scale and cross-scale interactions. Work to understand the closure of these terms to handle all scales of motion is ongoing. The time averaging of RANS models only allows for the simulation of steady turbulence, where fluctuations are assumed to average to zero over the time-averaging period. LES models are able to resolve the time evolution of turbulence and hence can be used to explore unsteady features of turbulence such as vortex shedding and separated or recirculating flows. Using LES in atmospheric applications does however come at a much higher computational cost than RANS models because the resolution required to resolve all of the most energetic scales of motion is much higher. Both RANS and LES methods have been applied to the field of canopy flows. In the following section the various studies involving numerical simulation of canopy flows is discussed. Each study acknowledges the shortcomings of the type of model used but provides a deeper understanding of the flow in and around a tall plant canopy regardless of the method of closure.

2.2 Methods of modelling a forest canopy

2.2.1 Representing a canopy with surface roughness

When numerical models are used to simulate flows over surfaces covered with vegetation, canopies are often parameterised using a roughness length, in line with Monin-Obukhov similarity theory (Monin and Obukhov, 1954). It is important to recognise that this relies on the assumption of horizontally homogeneous and flat terrain, so there are limitations in using such methods directly where the terrain is complex. However, in the absence of a better description, this theory is commonly used by researchers regardless of the complexity of the terrain being considered.

This method has long been used to model the effects of surface roughness (Jackson and Hunt, 1975), waves over open water (Charnock, 1955; Cheng et al., 2014), sub-grid-scale orography (Mason, 1985) and shallow canopies such as those of arable crops or grasslands (Tan and Ling, 1960; Tani, 1963; Uchijima and Wright, 1963). Due to success in replicating flows over canopies of vegetation, the method is also commonly used to represent even tall forest canopies in numerical prediction systems. The basis of this method is a relation between the horizontal wind speed (u), a scale of the surface elements present called a roughness length (z_0), the height above the ground (z) and the zero-plane displacement height (d) where wind velocity is expected or approximated to reach zero, defined as

$$u \propto ln\left(\frac{z-d}{z_0}\right). \tag{12}$$

Jackson and Hunt (1975) pioneered the modelling of flows over shallow hills in recognising that the flow could be divided in to two distinct layers. Close to the surface is an 'inner layer', where turbulent stresses are important and an 'outer layer' is present above, where perturbations of the flow are almost entirely inviscid. To achieve a more accurate prediction of the acceleration of the flow at hill crests, Hunt et al. (1988) incorporated more sub-divisions of these layers. A thin 'surface layer' is added beneath the 'inner layer' to better model the stream-wise pressure gradient induced by the hill. The 'outer layer' is divided in to a 'middle layer' where vorticity has a significant effect on the dynamics and an 'upper layer' where vorticity does not have a significant effect. Belcher et al. (1993) included the effect of upstream shear and showed that a thickening of the boundary layer in the lee of shallow hills was the main cause of momentum loss in the flow. Later improvements provided predictions of the hill geometries for which flow separation will occur on the lee slope (Wood, 1995) and the extra drag that can be caused by gravity waves in stratified conditions (Belcher and Wood, 1996). These works provided a framework for which flows over complex terrain could be more accurately re-produced and understood. Wind-tunnel experiments such as that of Finnigan and Brunet (1995) and flume experiments such as those by Poggi and Katul (2007) combined shallow hills with artificial canopies to test these methods. It was found that flow separation would occur over the lee slope even when hills were not steep enough for these theories to predict recirculation.

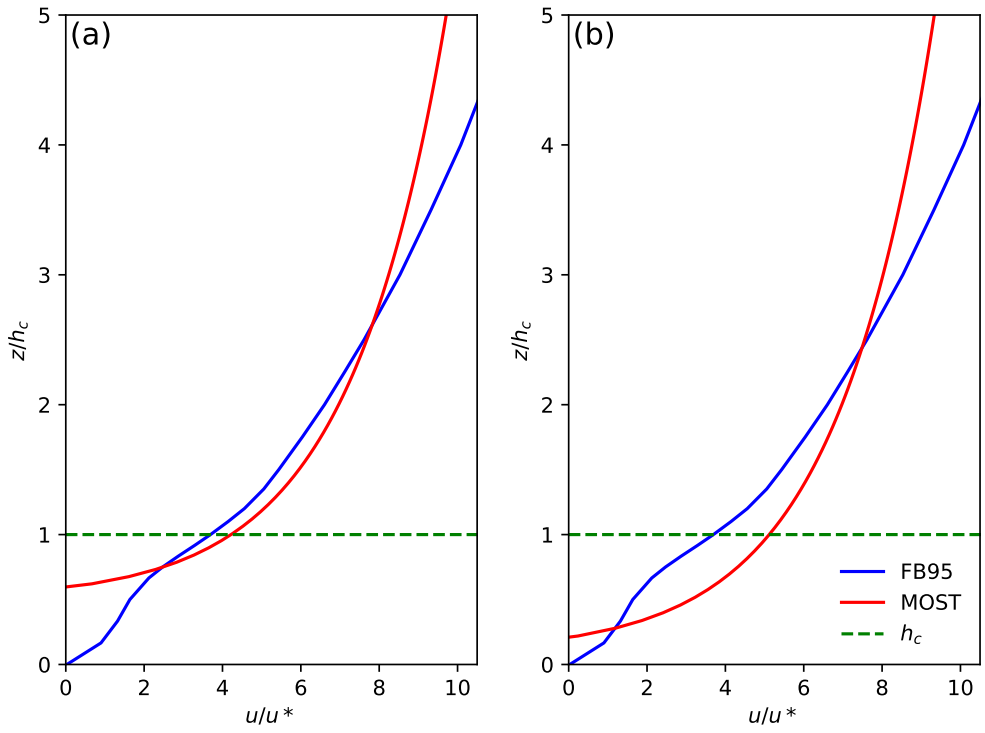

Figure 7: Example wind profiles from the wind-tunnel experiment of Finnigan and Brunet (1995) (blue) and the closest fit for equation (12) (red), where $h_c = 1$ is the height of the canopy (marked with a green dotted line). Panel (a) shows the best fit to the measured profile above the displacement height and panel (b) shows the best fit with the entire profile over a range of $0 \leq z_0/h_c \leq 0.2$ and $0 \leq d/h_c \leq 1$

The parameters z_0 and d must be obtained by fitting equation (12) to wind profiles that have been measured or those that have been generated in a numerical simulation. Given that such a process would be very intensive in a large-scale numerical simulation of a real-world scenario, these values are usually pre-defined for different surface types. Verhoef et al. (1997) found that values of $z_0/h_c = 0.046$ and $d/h_c = 0.67$, where h_c is the height of the canopy, tended to be appropriate over a range of different canopy types. However, these values vary depending on the canopy being considered and larger canopies can have a displacement height closer to $d/h_c = 0.75$ (Martano, 1999). It is also the case that fitting a logarithmic wind profile to that of a tall canopy is less sensible, given the inflection that is often present near the top of the canopy. As an example, the wind profile measured over the artificial canopy of Finnigan and Brunet (1995) in a wind-tunnel experiment is best fit by equation (12) with $d/h_c = 0.5$ and $z_0/h_c = 0.093$ when the fit is applied to the portion of the profile above the selected displacement height, as in Fig 7(a). If the fit is applied to the whole profile, as in Fig. 7(b), then values of $d/h_c = 0.09$ and $z_0/h_c = 0.117$ provide closer agreement with the measured profile.

The effect of this relationship is to reduce the wind speed to $0\,\mathrm{m\,s^{-1}}$ at the displacement height with wind speed increasing logarithmically above. The measured profile presented in Fig 7 clearly does not take this form, with non-zero wind speeds down to ground level and the logarithmic profile

over-estimating wind speeds above $h/h_c = 2.5$. As this use of equation (12) moves the no-slip boundary condition to the displacement height, it does not allow for flow or turbulence within a canopy. When used for canopy elements of small scales, such as crops and surface roughness, the differences in the flow statistics above the canopy are negligible. However, when dealing with canopy elements on the scales of mature trees ($10 - 30$ m in height), turbulence within the canopy can have an effect on the flow above and so can not be ignored (Ross, 2012). Applying drag at the surface also fails to induce the increased turbulence seen at canopy top, caused by shear between the uninterrupted flow above the canopy and the rapidly decelerated flow within the canopy. Studies using a roughness length approach to simulate flow near forest canopies have also shown that various features of the flow above the canopy are not recreated successfully (Finnigan and Brunet, 1995; Ross, 2012). Theoretical (Finnigan and Belcher, 2004) and numerical (Ross and Vosper, 2005) studies have shown that a large roughness length does not accurately recreate the results of wind-tunnel experiments. It was therefore necessary to develop new models that simulate the flows through and above a forest canopy more realistically.

2.2.2 Modelling a forest canopy explicitly

Where a canopy is modelled using an increased roughness length at the surface the turbulence induced by the shear layer at the canopy top, the dissipation of turbulence within the canopy and features of the flow such as separation or drainage flows within the canopy are not modelled. The basis of most canopy models that take such effects into consideration is the formulation developed by Shaw and Schumann (1992). This work was the first to apply the modifications to momentum and turbulence within a canopy of true vertical extent in a numerical modelling system in a large-eddy simulation (LES) mode. As the air interacts with the various elements of the canopy, frictional forces reduce the momentum of the flow. It is therefore necessary to add a drag force to the equation for momentum to model this process, which is found to be the most significant effect of the canopy on the flow. This force is consistently modelled with a sink term added to the momentum equation by Shaw and Schumann (1992), namely

$$\mathbf{F}_c = -C_d a |\mathbf{u}| \mathbf{u}, \tag{13}$$

where C_d is a dimensionless bulk drag coefficient, a is the leaf area density in $\mathrm{m}^2/\mathrm{m}^3$ (m^{-1}) and $|\mathbf{u}|\mathbf{u}$ is the product of the resolved velocity $\mathbf{u}$ and its magnitude. For the model described in Sect. 2.2.4 and used in Sect. 3 and Sect. 4, the eddy viscosity for momentum K_m is defined as

$$K_m = C_k \lambda k_{SGS}^{1/2}, \tag{14}$$

where C_k is a diffusion coefficient, k_{SGS} is the TKE per unit mass and λ is a length scale defined algebraically. A one-and-a-half-order turbulence closure is used, in which k_{SGS} is specified with a

transport equation but the dissipation ϵ is only specified algebraically using local statistics. Closures of higher order have been used to simulate turbulence to a high level of detail (Lumley, 1978; Ayotte et al., 1999). These more complex specifications of turbulence require considerably more computing power in large-scale numerical simulations and provide comparable results to first order closures for canopy flows (Katul et al., 2004). Pinard and Wilson (2001) also found that second-order closures do not simulate the fundamental properties of the flow above the canopy any more accurately than first-order closures. For locations in free space, where no canopy is present, the SGS TKE dissipation is modelled as

$$\epsilon_v = C_\epsilon k_{SGS}^{3/2}/\lambda, \tag{15}$$

where C_ϵ is a dissipation coefficient. As a flow interacts with canopy elements of small scales, such as the leaves and branches of a forest canopy, the scale of turbulent eddies present within the canopy are reduced. As turbulence cascades down to smaller scales it eventually reaches the Kolmogorov scale and the energy is dissipated by molecular forces (Kitamura, 2014). The dissipation of SGS TKE within the canopy is modelled as

$$\epsilon_c = 2C_d a|\mathbf{u}|k_{SGS}, \tag{16}$$

For locations that are within the canopy, the maximum is taken of the two terms ϵ_v and ϵ_c such that $\epsilon = max(\epsilon_v, \epsilon_c)$.

For LES simulations the length scale λ is based on the grid resolution and is usually set as the cube-root of the volume of a grid cell $\lambda_g = (\Delta \mathrm{x}\, \Delta \mathrm{y}\, \Delta \mathrm{z})^{1/3}$. The length-scale of turbulence is reduced within and in close proximity to the canopy. Where RANS equations are used, or if the grid dimensions are of the order of the canopy height, the equations of Wilson et al. (1998) can be used to determine the most energetic scales of turbulence close to the canopy, namely

$$\frac{1}{\lambda_i} = \frac{1}{\kappa z} + \frac{1}{\lambda_c} \tag{17}$$

$$\frac{1}{\lambda_o} = \frac{1}{\kappa(z-d)} + \frac{1}{L_\infty} \tag{18}$$

where

$$\lambda_c = \frac{|\mathbf{u}|(h_c)}{\partial|\mathbf{u}|/\partial z(h_c)} \tag{19}$$

and where $\kappa = 0.4$ is von Kármáns constant, h_c is the height of the canopy, d is the zero-plane displacement height of the canopy and L_∞ is a length scale used represent the restricted depth of the inertial sub-layer for wind-tunnel experiments. This scale is set to infinity for simulations not covered with a solid surface. The maximum of λ_i and λ_o is then taken as the canopy length scale λ_c. For eddy-resolving simulations with grid resolutions not much smaller than the canopy height,

λ is taken as the maximum of λ_c and the grid scale λ_g.

2.2.3 Canopy properties

The two parameters that are required to model the canopy explicitly are the drag coefficient C_d and the leaf area density (LAD) a. These parameters take on quite different values in the various studies carried out using this model. They are often extrapolated from wind speed measurements and sometimes chosen arbitrarily. Treuhaft et al. (2002) measured values of $0.02 - 0.18\,\mathrm{m}^{-1}$ in three forests located in Central Oregon, USA, using airborne radar and spectrometer systems and compared to field measurements of the geometry of the trees in twenty $100 \times 100\,\mathrm{m}$ plots. An average error of $0.02\,\mathrm{m}^{-1}$ and maximum error of $0.06\,\mathrm{m}^{-1}$ was found between the airborne and direct measurements, within a 1–2 standard error range. Maximum LADs of up to $2.2\,\mathrm{m}^{-1}$ were obtained in several studies of different types of woodland and presented together by Lalic and Mihailovic (2004). These included pine forests with maximum values of 0.15–$1.4\,\mathrm{m}^{-1}$, maple forests with maximum values of 1.1–$2.2\,\mathrm{m}^{-1}$, a silver birch forest with a maximum of $1.9\,\mathrm{m}^{-1}$ and an oak forest with a maximum of about $1.6\,\mathrm{m}^{-1}$. Similar values were measured by Hosoi and Omasa (2009) using a ground based lidar system on a $4\,\mathrm{m}$ by $8\,\mathrm{m}$ plot of broadleaved zelkova woodland. The maximum LAD measured was approximately $1.8\,\mathrm{m}^{-1}$ and a root-mean-squared error between lidar and direct measurements was $0.26\,\mathrm{m}^{-1}$. This study also found that the LAD decreased by approximately $0.4\,\mathrm{m}^{-1}$ throughout the upper half of the deciduous forest in the winter months due to the senescence of the leaves.

Lalic and Mihailovic (2004) used their measurements to formulate an equation to calculate vertical LAD profiles based on the leaf area index (LAI) L_m, canopy height h_c, height of maximum LAD z_m, sample height z and an arbitrary parameter n of the form

$$L(z) = L_m \left(\frac{h - z_m}{h - z}\right)^n exp\left[n\left(1 - \frac{h - z_m}{h - z}\right)\right], \tag{20}$$

$$\text{where } n = \begin{cases} 6, 0 \leq z < z_m \\ \frac{1}{2}, z_m \leq z \leq h_c. \end{cases} \tag{21}$$

Use of this formula requires pre-existing knowledge of the LAI, which is commonly found in land usage datasets. However, it also requires the height at which the LAD is at a maximum level. This can be assumed for different tree species, but could vary depending on climate or in woodlands of mixed species. This method becomes impractical if modelling large areas with only low resolution land usage fields that may or may not be fully forested and where species information may not be available. However, a combination of aerial scanning methods to determine LAI and formulae to estimate vertical LAD profiles currently provide the best methods for determination of LAD a.

With respect to the value for the drag coefficient C_d, some studies reference Brunet et al. (1994)

or Raupach et al. (1996) as giving a value of 0.25 for natural canopies (Finnigan and Belcher, 2004; Ross and Vosper, 2005). Brunet et al. (1994) found a similar value of 0.28 (given as 0.56 but using an extra factor of $1/2$ in their equations) when they ran their wind tunnel at full speed with an artificial canopy inside. Dupont et al. (2008) used a value of $C_d = 0.2$ sourced from Kaimal and Finnigan (1994), which states this as a mean value for typical vegetation canopies. In the LES study carried out by Shaw and Schumann (1992), the value 0.15 was used on the basis of data from a deciduous woodland (Shaw et al., 1988). Gillies et al. (2002) measured C_d for several species of plant by mounting specimens on a force balance and placing them in a wind tunnel. A range of values $C_d = 0.25$ to 0.5 were found for different flow velocities and, hence, Reynolds numbers Re. The measured C_d for fountain grass (*Pennisetum setaceum*) was found to decrease from 0.46 to 0.3 as Re increased from 55480 to 525687. However, this relation was found to be different for the other two species studied, burning bush (*Euonymus alatus*) and Colorado blue spruce (*Picea pungens glauca*), which are of a form more in line with species found within a forest. For burning bush, C_d increased from a minimum of 0.31 at $Re = 46662$ to a maximum of 0.48 at $Re = 139127$, reducing to 0.4 for $Re = 200000$ and remaining at this value as Re increased further. For the Colorado blue spruce, C_d increased from 0.28 at $Re = 57525$ to 0.41 at $Re = 175517$ and again remained relatively constant at this value for increasing Re.

As can be seen from this investigation of the literature, the density of the canopy and the drag that different species produce in different conditions vary considerably. Where intensive studies are performed for a canopy covered site before numerical simulations are carried out, it is now fairly common for aerial lidar studies to characterise the vegetation that is present. For instance, at the site of the Perdigão field campaign that is used as a case study in Sect. 4, high-resolution lidar scans by Palma and Batista (2019a,b) retrieved measurements of the LAI and canopy height across a $4 \times 4\,$km area around the location that was studied. Where numerical simulations are to be used to predict weather for an area that has not been studied so intensely, accurate and high resolution data on canopy height and LAI/LAD is less likely to be available. It therefore becomes necessary for canopy properties to be assumed based on LAI and canopy height data from land use datasets such as those provided by the United States Geological Survey (USGS) or the coordination of information on the environment (CORINE) dataset provided by the European Environment Agency. Random sampling of canopy height and density for forested locations across the site could also be used to improve the representation of the canopy in numerical simulations.

2.2.4 Implementation of a canopy model

Canopy models are not widely available in numerical weather prediction systems and so it was necessary to find a suitable system in which the model described in Sect. 2.2.2 could be implemented. The Weather Research and Forecasting (WRF) model is an open source piece of software that has been in development for several decades and is commonly used by researchers for weather prediction

and modelling (Skamarock et al., 2019). Below is a description of the WRF model as provided by its curators at the Mesoscale and Microscale Meteorology (MMM) Laboratory (WRF, a).

"The Weather Research and Forecasting (WRF) Model is a next-generation mesoscale numerical weather prediction system designed for both atmospheric research and operational forecasting applications. It features two dynamical cores, a data assimilation system, and a software architecture supporting parallel computation and system extensibility. The model serves a wide range of meteorological applications across scales from tens of meters to thousands of kilometres. The effort to develop WRF began in the latter part of the 1990's and was a collaborative partnership of the National Center for Atmospheric Research (NCAR), the National Oceanic and Atmospheric Administration (represented by the National Centers for Environmental Prediction (NCEP) and the (then) Forecast Systems Laboratory (FSL)), the (then) Air Force Weather Agency (AFWA), the Naval Research Laboratory, the University of Oklahoma, and the Federal Aviation Administration (FAA)."

As explained above, WRF is capable of carrying out meteorological simulations over a wide range of scales. The support for parallel computation also means the model can be run efficiently on high powered computing clusters. This allows complex simulations to be run on high powered, distributed computing systems in far less time than it would take even a highly specified personal computer. The fact that WRF is a freely available community model means that the implementation of the canopy model can be made available to a wide audience. The WRF Users website (WRF, b) has several tutorials where the user can run through test cases for different situations and types of simulation. These cover a range of scenarios from real world simulations to idealised cases. There is also a wide range of documentation on the usage of the WRF model and of the various physics options which are built in to the software. Given the open-source nature and extensive documentation of the model and the large and supportive community, this was seen as a perfect candidate for the implementation of the canopy model.

The WRF model is written in the commonly used FORTRAN90 programming language. Although the physics used in the model is thoroughly documented, documentation regarding the structure of the code is limited. A considerable amount of investigation and testing was therefore required to locate and modify the sections of code relevant to the canopy model. One of the most useful aspects of the way the WRF model is coded is the registry system. Registry files contain a list of all the variables used in the model, their dimensions, input/output (IO) settings and given name in the output files that are created during simulations. To add a new variable to the model (or to the configuration options) is as simple as adding a new line to this file. It also makes it very easy to include or exclude variables from the output files for testing purposes. This allows the user to output extra data or to reduce the size of output files where required. The registry is also very useful to keep track of what the variables represent. Although there are some exceptions, most variables have a short description of what they represent and their units. Due to the large number of variables required in the model the names that they are given do not always clearly reflect the names

or symbols commonly given to their physical counterparts. Having them listed with descriptions in the registry this way is therefore very useful for the user.

The canopy model described in Sect. 2.2.2 was initially implemented in WRF version 3.9.1.1, as this was the latest available version at the start of the project. This version was used for the work presented in Sect. 3, but the relevant code was later transferred to version 4.1.1 for use in the work presented in Sect. 4. The changes to WRF between these two versions did not require that any of the code was substantially changed and the modifications to the flow dynamics resulting from a canopy are implemented identically in each version. While WRF contains a module for simulations involving an urban canopy, it relies on surface properties such as roughness length to model a forest canopy. It was therefore necessary to implement entirely new code to explicitly model the canopy over several vertical levels. There are three equations and one constant that require modification in order to achieve this, as described in section 2.2.2.

The momentum equations are processed in the WRF model by the `solve_em` subroutine. Many of the variables in this subroutine are coupled with the mass of the column of air above the grid cell being processed (`mu`). Variables are also converted to perturbation values while they are advanced in a series of small time steps for each model time step. Care must therefore be taken to ensure that any new code handles these variables correctly and at the correct time. To double check this, a series of variables were added to extract the various terms of the momentum equation and check that everything added up correctly. The canopy momentum sink term described in equation (25) was added to the momentum equation in the script `module_first_rk_step_part2` after the update of physical tendency terms in subroutine `update_phy_ten` and before the script goes on to calculate TKE in `tke_rhs`. TKE dissipation is already handled in the WRF model by the subroutine `tke_dissip`. New code was added here to calculate the dissipation term from equation (16) where a canopy is present. The larger of this term and the default dissipation term is then subtracted from the TKE budget.

Numerical weather prediction systems such as the WRF model handle turbulence of a scale larger than a grid cell explicitly. For this reason the turbulence length scale is usually set to the cube root of a grid cells volume. However, if the Brunt-Väisälä frequency (N) exceeds $1 \times 10^{-3}\,\mathrm{s}^{-1}$ then the length scale is set as $0.76\sqrt{k}/N$. All of this is handled by the subroutine `calc_l_scale`, where the Wilson et al. (1998) length scale calculations (see equations (17), (18) and (19)) were implemented. Due to the the fact that the length scale is limited by the size of the grid cells, λ_o only tends to apply within close proximity of the canopy top. Beyond this, and in areas where no canopy is present, the standard WRF methodology is used to calculate the turbulence length scale. A new subroutine called `calc_vl_scale` was also implemented to use these equations to calculate a vertical length scale. This scale is only used by WRF in calculating the exchange coefficients for the TKE turbulence parametrisation.

Lastly, there is a coefficient relating to the Prandtl number of the flow, used by Wilson et al. (1998) to define an eddy diffusivity for the transport term of the TKE equation. This coefficient

has been implemented in the `horizontal_diffusion_s` and `vertical_diffusion_s` subroutines, such that it is only applied when they are used to calculate TKE transport within the canopy. Wilson et al. (1998) state that the optimal value for this coefficient for free flowing and boundary layer flows is approximately unity, according to Launder and Spalding (1972, 1974). However, in testing different values, they came to the conclusion that a value of 0.2 is preferable. Finnigan (2000) states that this coefficient falls from approximately 1.0 to 0.5 at the canopy top but does not describe whether this value is reduced further as one descends in to the canopy. A value of 0.2 therefore seems acceptable and has been added as an optional modification, but has been shown to have an insignificant effect in test simulations.

2.3 Modelling studies

2.3.1 Flat forested terrain

Shaw and Schumann (1992) were the first to perform numerical simulations using a canopy model in an LES mode and were able to resolve structures of turbulence similar to that seen in flat forested terrain. This work included the form drag and dissipation of turbulence within a canopy that was resolved vertically over 10 grid levels. A simple source term was also included to represent heat imparted to the air by the vegetation. This was a pilot study of the canopy model methods but the simulations carried out produced results consistent with the turbulence patterns found within forested sites. In a later study, Shaw and Patton (2003) included terms to represent momentum loss and turbulence dissipation due to skin friction between the air and canopy elements. However, it was found that this effect was minimal compared to the form drag and dissipation of TKE due to the wakes produced in the lee of canopy elements. Watanabe (2004) went on to model the diffusion of scalars throughout a canopy and was able to reproduce realistic concentrations near the canopy top. Partially forested flat terrain was then studied by Clark and Mitchell (2007) but only the form drag within the canopy was included. The focus of this work was to determine how patterns of harvesting for forestry purposes affected the bending moment, and hence the chance of stem failure, for stands of unharvested trees within the site. It was found that decreasing the size and spacing of such compartments of felled and retained trees reduced the bending moment of trees downstream of the edge of the site. Dupont and Brunet (2008a) used the momentum sink and dissipation of turbulent kinetic energy in the canopy to investigate the effects of canopy edges with resolutions of $2\,\mathrm{m}$ in the horizontal. The model was able to reproduce features such as an "enhanced gust zone" (EGZ) which is found near the edge of a canopy, as was found in analytical solutions by Raupach et al. (1987). Increasing canopy density was found to increase the strength of gusts within the EGZ. The same was true of reducing the density of the lower portion of the canopy to represent a sparse trunk space, due to a low level jet strengthening gusts in the clearing upstream of the canopy edge. Attempts have been made to resolve the canopy with a higher level of detail as a series of solid trunks surrounded with a porous leaf space by Yue et al. (2007). This method requires a very high

resolution to resolve individual tree trunks and was not found to improve reproduction of the mean flow or associated shear stresses.

The sensitivity of the model to the canopy density and the distribution of density in the vertical was explored further by Dupont and Brunet (2008b). It was found that increasing density made it more difficult for turbulence to penetrate deep in to the canopy but made downward gusts in to the canopy more likely. The stages of development of the turbulence occurring immediately above the canopy top and their development downstream of a canopy edge (as discussed in Sect. 1.2) were successfully reproduced by Dupont and Brunet (2009). It was also found that increasing the canopy density reduced the distance over which the instabilities at canopy top formed. Ross (2012) investigated the effects of a varying canopy density in the horizontal using analytical, numerical and surface roughness based methods. Each method produced very different results, but there was no comparison to measurements to determine which method was the most successful. Further work was done to assess the importance of representing the variability of canopy morphology by Desmond et al. (2014). The flow over a heterogeneous canopy of model trees with a variety of morphologies and heights was measured in a wind-tunnel experiment. This experimental data was then compared against the results of simulations representing the canopy either as a porous block with constant height, a porous block with variable height matching the height distribution of the artificial canopy or as a series of individual cylinders to represent each model tree. This study showed that the accuracy of the simulations in reproducing the measured flow was not strongly dependent on the morphology, but was increased by a more accurate representation of the heterogeneity of canopy density. The effects of vertical resolution on the dynamics within and immediately above a forest canopy were investigated by Ouwersloot et al. (2017). However, this study focussed on instabilities caused by a sharp transition from a dense canopy to the free air above. These instabilities were reduced by including a more smooth transition of density at the canopy top, but such methods are only possible where enough grid levels are present within the canopy for this to be practical. Further investigation of the sensitivity to vertical resolution and to the number of vertical levels needed to represent the canopy is carried out in Sect. 3 and Sect. 4.

2.3.2 Thermal effects

While Shaw and Schumann (1992) had included a basic heat source to represent transfer of heat from canopy elements to the air, the other studies above used only the form drag and sometimes the dissipation of turbulence to model the canopy. In some cases the thermal effects of the canopy can modify the dynamics of the flow in and around a canopy to produce motions such as drainage flows. Garrett (1983) had previously attempted to model the temperature of canopy elements explicitly with a sensible heat flux between the canopy elements and the air. This method used a rate of transfer based on measurements of the loss of heat from canopy elements to cooler air. Yamada (1982) used a similar method with a constant ratio of sensible and latent heat transfers, but neglected heat

storage within the canopy elements. While reasonable vertical distributions of temperature were found for periods of cooling, daytime temperatures in simulations involving a canopy were up to 8°C higher than those without a canopy present. The rate of cooling in the early evening was also higher within the canopy, which would not be expected if heat stored within the canopy throughout the day had not been considered negligible. These methods were developed further by Sun et al. (2006) to include heat storage within canopy elements. It was assumed that the canopy elements and the air would cool at the same rate, but this led to unrealistically high rates of cooling of the canopy air space. To avoid this high rate of cooling Sun et al. (2006) required a canopy density that was much larger than those seen in real forest canopies.

The imbalance in the rate at which the temperature of the air and the canopy change was recognised by Froelich et al. (2011). A coefficient was implemented to increase the rate at which canopy elements cool in the evening and warm in the morning. The model was compared to flux tower data of air temperatures within a canopy covered site and was shown to perform well. The authors point out that there was insufficient data available regarding heat storage and transfer between the canopy elements and the canopy air space to develop the model further. The process is complex given the range of scales for different canopy elements (leaves, twigs, branches, stems), the difference in rate of transfer for different species with different morphologies and surfaces (such as bark thickness and roughness) and the interplay between the above and below ground portions of the vegetation including uptake of water from the ground and also heat transfer through evaporation and transpiration. Studies have been carried out more recently to investigate the thermal interaction between the stems (Li et al., 2017) or leaves/needles (Musselman and Pomeroy, 2017) with the surrounding air space and to improve modelling of evaporation and transpiration processes Xu et al. (2016). However, due to the uncertainty around heat transfer within the canopy, more recent versions of vertically explicit canopy models often do not include the thermal effects (Ouwersloot et al., 2017; Arthur et al., 2019) or rely on the methods mentioned above (Ma and Liu, 2019). Due to the uncertainties in representing the canopy heat storage and transfer between the canopy and the surrounding air space it was decided not to implement terms relating to these in the canopy model described in Sect. 2.2.4. For such processes to be modelled would require more detailed data regarding the temperature and thermal properties of a forest against which to compare.

2.3.3 Flow over forested hills

While it has still not been possible to fully parameterise heat transfer and storage within the canopy, the modifications to momentum and the dissipation of turbulence within a canopy have been shown to be very effective at reproducing flows over flat terrain. Due to the success of this method the canopy model has also been extended to numerical simulations of flows over idealised complex terrain. Kobayashi et al. (1994) studied various geometries of isolated hills covered with a forest canopy in two dimensions and found that the results compared well with wind-tunnel observations. The wind-

tunnel experiment of Finnigan and Brunet (1995) for flow over a 'hill' with a two-dimensional ridge-like profile was reproduced in three-dimensional numerical simulations performed by Wilson et al. (1998). A field study of flow in a corn canopy and a study in a wind tunnel using an artificial canopy of 'tombstone' shaped bars (both on flat surfaces) were also studied. The use of a simple turbulence closure, with ϵ_c specified as in equation (16), was shown to reproduce the mean flow within and above these canopies successfully. Brown et al. (2001) applied a first order turbulence closure and canopy momentum sink to simulate wind-tunnel experiments over three canopy covered, shallow hills. Even this first order closure was able to re-produce these flows accurately, but the cases considered did not produce strongly separated flows. A canopy model with a one-and-a-half-order closure scheme was applied to simulations of the Finnigan and Brunet (1995) wind-tunnel experiment by Ross and Vosper (2005). In comparison to representing the canopy with an increased surface roughness, it was found that simulations using a canopy model were better able to predict flow separation in the lee of the hill. The canopy model also led to more realistic drag on the flow and displaced the pressure minimum further downstream of the hill-top, as had been seen in field measurements and experimental data.

Ayotte (2008) used similar wind-tunnel experiments over an isolated hill to assess wind turbine productivity and potential for damage. They found that using LES methods to resolve fine scale turbulent motions allowed for better reproduction of the wake formed in the lee of a hill covered in a canopy. It was noted that the effectiveness of such methods would be likely to improve as computing power increased and higher resolutions allowed for finer scales of turbulence to be resolved in numerical simulations, as confirmed later by Patton (2006). To reduce the computational power required to simulate at higher resolutions, Dupont et al. (2008) used a process of domain nesting. The Finnigan and Brunet (1995) experiment was simulated at high resolution in close proximity to the hill, while the flow outside this region was simulated at a lower resolution. This reduces the amount of calculations that are required in locations where turbulence length-scales are large, while still resolving the fine scales of turbulence seen around the canopy covered hill. This method was able to reproduce the Finnigan and Brunet (1995) results to a high degree of accuracy but highlighted discrepancies such as insufficient variance in vertical velocity over flat forested terrain and excessive production of TKE in the wake region downstream of the hill-top. Ross (2008) compared first order LES to one-and-a-half order RANS and found that both were able to reproduce the main features of the flow successfully, including flow separation.

The impact of canopy density on the flow over a canopy covered hill was explored by Patton and Katul (2009), although apparently without inclusion of the modified turbulence dissipation term within the canopy. The experimental findings of Finnigan and Belcher (2004) and Poggi and Katul (2007) that increased canopy density for the same hill geometry can lead to flow reversal within the canopy on the lee slope were confirmed. Ross (2011) investigated scalar transport over a canopy covered hill and found that variations in scalar concentration were more dependent on turbulent transport than advection. However, the impact of advection on scalar concentration was found

to increase with increasing hill steepness or canopy depth, or for decreasing canopy density. All of these studies have explored the flow over hills covered entirely with a homogeneous canopy. In real-world scenarios this will rarely be the case and so Ross and Baker (2013) explored the effects of partially forested hills. Regions of flow separation were found to be limited in the horizontal to terrain covered by a canopy and predominantly limited to the lee slope. Xu et al. (2015) used a two-dimensional model to investigate the flow over a hill in stable conditions and found that an unstable layer develops within the canopy and increased buoyancy close to the ground was found to suppress turbulence significantly within and immediately above the canopy. Each of these studies has shown that resolving the momentum sink and turbulence dissipation of a canopy over several vertical levels provides significant benefits over simply parameterising the canopy at the surface boundary. More recently, researchers have been attempting to apply the canopy model to real-world situations to see if it can provide benefits to larger-scale simulations with more complex terrain features.

2.3.4 Real-world scenarios

The canopy model has been explored using a wide range of canopy properties, canopy distributions and terrain geometries in idealised numerical simulations. It has been necessary to rely on wind-tunnel experiments with idealised terrain due to the lack of data from field experiments regarding flows over forested complex terrain or flat terrain with heterogeneous canopy cover. While the canopy model may still have some deficiencies in reproducing flows over complex terrain, it has been shown to be more effective at reproducing the characteristics of these flows than simply relying on changes in roughness length at the surface. Most of the idealised studies that have been carried out also use resolutions that would become impractical over the large areas that require simulation to properly reproduce flows in real-world situations. However, given the importance of representing the heterogeneities of canopy cover, the resolution can not be decreased significantly if the benefits of the canopy model are to be retained.

A relatively flat site with heterogeneous canopy cover including a large clearing was used as a case study by Schlegel et al. (2015). Ultrasonic anemometer data from four flux towers was compared to numerical simulations using a sub-tree-size grid resolution of $2\,\mathrm{m}$. The representation of the canopy was based on randomly sampled canopy height and density data that was interpolated across the extent of the simulated domain. The results of the field experiment were compared to two simulated cases with either a vertically homogeneous but horizontally varying canopy density or a realistic three-dimensional distribution of density based on measured and predicted vertical profiles. The heterogeneous representation of the canopy density was able to reproduce the flow measured at the flux towers well and also reproduced features of the flow such as enhanced gust zones near the clearing. The fully three-dimensional representation produced similar results to the two-dimensional distribution of density for the stream-wise velocity and TKE. However, profiles of the vertical velocity component collected at towers in the clearing and some distance in to the canopy downstream of

the clearing were closer to those measured when the variation of density in the vertical was included. This study provided evidence that representing the heterogeneity of canopy density in simulations of real-world scenarios is important to reproduce flows within and immediately above a forest canopy. Another study by Liu et al. (2016) was carried out to examine the effectiveness of a canopy model at reproducing the flow measured at a single tower at Taikoyama wind farm near Kyoto, Japan. The importance of using a resolution in the horizontal at least as large as the height of the canopy and of also including a large area of the surrounding terrain in numerical simulations was highlighted. Terrain features nearly 6 km upstream were found to have a significant impact on the simulated flow at the measurement tower. This conflict of requiring high resolution and simultaneously needing to simulate the flow over a large horizontal extent lead to a high computational cost of using the canopy model.

More extensive measurements of flow over the canopy covered ridge Leac Gharbh on the Isle of Arran, Scotland were collected by Grant et al. (2015). Numerical simulations were carried out by Grant et al. (2016) with a 50 m horizontal resolution and a 0.5 m vertical resolution at the surface for a near-neutral flow over the ridge. A RANS model with a one-and-a-half-order, mixing-length based turbulence closure was shown to reproduce many features of the observed flow, such as the promotion of flow separation over the gentle slope of the ridge. Although accurate data for the location of the canopy was available, canopy properties such as height, density and drag coefficient were chosen based on sampling studies at the ridge and applied to all locations where a canopy was present. The distance that was expected for the flow to adjust to the canopy with the properties selected was approximately 24 m and large discrepancies with the observations were found at these locations. While high-resolution data for the canopy properties might have led to greater accuracy, the large discrepancy was more likely due to the horizontal resolution being slightly more than double the canopy edge adjustment length. This highlights the importance of using a high resolution in numerical simulations where the canopy is expected to have a significant effect on the flow that is being considered. The authors also suggest that LES may also be required to better resolve and diagnose the effect of the canopy on the flow and for other cases of atmospheric stability to be considered.

A field campaign has since been carried out where extensive measurements were taken for the flow over the double-ridge Vale Cobrão, Portugal (Fernando et al., 2019). A 49 day period of observations at the site were compared to numerical simulations by Wagner et al. (2019) using a series of nested domains. The outermost domain covered the entire Iberian peninsula, while the innermost domain covered the length of the Vale Cobrão and ran in an LES mode with a horizontal resolution of 200 m and a vertical resolution of 15 m. It was found that the use of a canopy model was necessary to reproduce the observed flow at the site accurately. The largest discrepancy with the observations was an underestimation in the strength of the along-valley flow at the site. Locations where forest land use was recorded in the CORINE land use dataset were represented with a randomly distributed canopy height of 30 m ± 5 m. It was suggested that higher-resolution input data may improve the

discrepancies with observations, providing further motivation for a high-resolution simulation with accurate representation of the properties of the canopy across the site. Numerical simulations of the flow over this site for a 3 hour night-time period in stable conditions are presented in Sect. 4 at a horizontal resolution of $10\,\mathrm{m}$. For the terrain considered a vertical resolution near the surface of $\approx 6\,\mathrm{m}$ was required to avoid numerical instabilities. Considerable advantages were still found over conventional methods of parameterising the canopy at the surface boundary, but high resolution canopy data was not found to significantly improve the accuracy of the simulations.

SECTION 3

Numerical modelling of neutral boundary-layer flow across a forested ridge

3.1 Motivation

Once the WRF model had been modified to include the canopy model implemented in Sect. 2.2.4 it was necessary to test that the flow over forested complex terrain could be re-produced successfully. An idealised case was required for this purpose before the model could be applied to a real-world situation where the terrain and distribution of the canopy are truly complex. Finnigan and Brunet (1995) carried out a wind-tunnel experiment to examine the flow over a shallow ridge with a two-dimensional profile in the span-wise direction. The artificial canopy used to cover this ridge was the same as that used by Finnigan and Mulhearn (1978) to simulate the flow over a flat canopy of wheat. This consisted of cylindrical nylon stalks that were $50\,\mathrm{mm}$ long and $0.25\,\mathrm{mm}$ in diameter and had the aero-elastic properties of wheat when the wind speed in the tunnel was $30\,\mathrm{m\,s^{-1}}$. This artificial canopy was placed on top of the ridge and a wind speed of $12\,\mathrm{m\,s^{-1}}$ was used in the tunnel such that the stalks behaved like the more rigid stems and branches of a forest canopy. This does not provide a true representation of a forest canopy but should affect the flow in a similar way and provides a known frontal density of $10\,\mathrm{m^{-1}}$ and a drag coefficient of $C_d = 1.35$. These canopy properties are somewhat larger than those measured in real canopies due to the small scale of the experiment, but can be used directly in numerical simulations. As described below, the canopy properties were scaled up in line with the work of Dupont et al. (2008) to create a more realistically scaled forest canopy. In the interest of providing novel scientific results the simulations described below were also carried out over a range of horizontal and vertical resolutions, as this had not been explored previously. The following chapter was peer-reviewed and accepted for publication in Boundary-Layer Meteorology on 13 May 2021. The article was authored by John Tolladay and Charles Chemel and published with the title "Numerical modelling of neutral boundary-layer flow across a forested ridge".

3.2 Abstract

Forest canopies have been shown to alter the dynamics of flows over complex terrain. Deficiencies have been found when tall canopies are represented in numerical simulations by an increase in

roughness length at the surface. Methods of explicitly modelling a forest canopy are not commonly available in community numerical weather prediction models. In this work, such a method is applied to the community Weather Research and Forecasting model. Simulations are carried out to replicate a wind-tunnel experiment of neutral boundary-layer flow across a forested ridge. It is shown that features of the flow, such as the separated region on the lee slope of the ridge, are reproduced by the roughness length or canopy model methods. Shear at the top of the ridge generates turbulence that spreads vertically as the flow moves downstream in both cases, but is elevated to canopy top where a canopy model is used. The roughness-length approach is shown to suffer several deficiencies, such as an over-prediction of mean wind-speeds, a lack of turbulence over flat forested ground and an insufficient vertical extent of turbulence at all locations of the domain studied. Sensitivity to the horizontal resolution of the simulation is explored. It is found that higher resolution simulations improve reproduction of the mean flow when modelling the canopy explicitly. However, higher resolutions do not provide improvements for the roughness-length case and lead to a reduction in the horizontal extent of the separated region of flow on the lee slope of the ridge.

3.3 Introduction

Interactions with surface elements such as buildings and forested areas have a significant effect on the flows present in complex (uneven) terrain (Fernando, 2010). It is thereby important to understand the contributing factors to these flows, so as to evaluate their impacts on pooling of cold air and air pollution in valleys or to predict mean wind speed and turbulence statistics for wind farm applications. Bastin et al. (2019a) estimated that 2.8 of the 15 billion hectares (that is 18.7%) of the Earth's land surface are covered in a forest canopy with a tree cover greater than 10%. Given the difficulty of building on ridge or valley sides and in mountainous areas, these areas are often left untouched and so likely to be covered in shrubs and trees at mid-latitudes. Therefore, a significant fraction of complex terrain is likely to be covered in a forest canopy of some sort.

Finnigan (2000) reviewed the bulk of the work done to date to understand flow in homogeneous forest canopies over flat ground. Belcher et al. (2012) built on this review to illustrate how canopy flows respond to complex terrain. More recently, Finnigan et al. (2020) reviewed the subject of boundary layer flows in complex terrain. A section of this review focused on theory, analytical and numerical models of flow over canopy covered hills, and considered the effects of stability and scalar transport. There is a reasonably good mechanistic understanding of the dynamics of canopy flows, the adjustment of flows at canopy edges, the ability to use 'simple' turbulence closures due to the inviscid nature of the dynamics, effects of forested terrain on scalar transport, the generation of reversed flows within canopies downstream of ridge-tops and the significant reduction of turbulence and momentum within a canopy. However, woodland canopies are often not modelled explicitly in numerical weather prediction (NWP) models and relatively little attention has been paid to the evaluation of the effects of forest cover in complex terrain in these models.

Due to the broad range of scales of canopy elements (e.g. leaves, twigs and branches), it is currently computationally impractical to model explicitly the processes involved in the canopy flow dynamics on the scale of canopy elements in NWP models. Recognising the increased friction caused by canopy elements, the most common approach to parametrise the effects of the canopy on the flow is to increase the roughness z_0 of the underlying surface and displace the height of the ground. As is customary in micrometeorology, let us align the x-direction with that of the mean horizontal flow (i.e. the stream-wise direction) of velocity $\langle u \rangle$ such that there is no variation of the mean span-wise component of velocity $\langle v \rangle$ in the y-direction. Parametrising the turbulent kinematic flux of stream-wise momentum in the vertical direction z (referred to as stream-wise momentum flux thereafter), $\langle u'w' \rangle$, using a first-order flux–gradient relationship yields

$$u_\star^2 \equiv -\langle u'w' \rangle = K_m \frac{\partial \langle u \rangle}{\partial z}, \tag{22}$$

where $u_\star \equiv \sqrt{|\langle u'w' \rangle|}$ is the (stream-wise) friction velocity and K_m is the eddy diffusivity of momentum. Using a mixing-length model, K_m is modelled, for neutral stability, as

$$K_m = \ell \, u_\star = \ell^2 \frac{\partial \langle u \rangle}{\partial z}, \tag{23}$$

where the mixing-length $\ell = \kappa \, (z - d)$, $\kappa = 0.4$ is the von Kármán constant and d is the zero-plane displacement height, where $\langle u \rangle = 0$. Assuming that $\langle u'w' \rangle$ is constant in the surface layer (that is $u_\star$ is constant in this 'constant-flux' layer), an integration of Equation (22) with the boundary condition $\langle u \rangle \, (z = d + z_0) = 0$ gives the logarithmic law

$$\langle u \rangle = \frac{u_{\star 0}}{\kappa} \ln \left(\frac{z - d}{z_0} \right), \tag{24}$$

where $u_{\star 0} = u_\star \, (z = 0)$. Since the wind speed is reduced to zero at the displacement height, this formulation cannot represent the flow or turbulence below the displacement height. When canopy elements are small in scale relative to the extent of the atmosphere being modelled above, flows within the canopy have little impact on the dynamics of the flow well above the canopy. A change in roughness length at the surface is, thereby, a reasonable option to be used in NWP models for flows over short canopies. However, when dealing with taller canopy elements on the scales of mature trees, in the range 10–50 m in height, turbulence and drag within the canopy can have a profound effect on the flow above canopy (e.g. Ross, 2012), which is not accounted for over a bare surface with increased roughness. Furthermore, the mixing length ℓ as defined above is not the most appropriate to use as a length scale for turbulent motions within a forest canopy (Wilson et al., 1998).

Several studies using the roughness-length approach to simulate the flow over forested ridges have shown that various features of the flow are not recreated accurately (e.g. Finnigan and Brunet, 1995; Ross and Vosper, 2005). In particular, the region of separated flow, where the wind downstream of a forested ridge reverses close to the ground, is often not as substantial in simulations using a

roughness-length parametrisation when compared to observations. The roughness-length approach also tends to over-predict the turbulence kinetic energy (TKE) within close proximity to ridge-tops. Finnigan and Belcher (2004) and Harman and Finnigan (2007) examined canopy flows with an analytical model and found evidence that canopies do not tend to a constant roughness length while flowing over hills. This suggests that using a constant roughness length across a forested section of a hill is unlikely to properly recreate the flows over forested, complex terrain. A study by Allen (2006), on the effects of roughness lengths on flows over ridges, found that flow separation is encouraged if the roughness length is largest at the top of ridges. If the surface roughness length is largest at the base of ridges then flow separation is reduced.

More success has been found in recreating flow dynamics within and above canopies where the effects of these canopies are modelled explicitly and with a proper vertical extent. Such models consider the canopy as a horizontally homogeneous but vertically resolved volume, wherein the total kinematic drag generated by the canopy, $\mathbf{F}_c$, is expressed as the product of a drag coefficient C_d, a one-sided plant area density a and the square of the resolved velocity $\mathbf{u}$ (see Wilson and Shaw, 1977; Raupach and Thom, 1981; Raupach and Shaw, 1982; Finnigan, 1985; Raupach et al., 1986), namely

$$\mathbf{F}_c = -C_d\, a\, |\mathbf{u}|\, \mathbf{u}. \tag{25}$$

This term represents the momentum per unit mass that is lost per unit time through interaction between the air and the trunks, branches and leaves that make up a forest canopy. Numerous studies added $\mathbf{F}_c$ as an additional sink of momentum to the momentum equation within the canopy in bespoke numerical models to study *(i)* observed properties of the flow within the canopy over flat ground, e.g. sweeps and ejections that govern turbulent transport (e.g. Shaw and Schumann, 1992; Dupont and Brunet, 2008a; Finnigan et al., 2009; Ouwersloot et al., 2017), effects of forest edges (e.g. Cassiani et al., 2008; Dupont et al., 2011), variability in plant-area density in the horizontal (e.g. Bohrer et al., 2009) and in the vertical (e.g. Dupont and Brunet, 2008a), and *(ii)* the associated biosphere–atmosphere exchange of trace-gas and other scalars (e.g. Patton et al., 2001, 2003). In the study by Ouwersloot et al. (2017), some work was done to assess the sensitivity of model results to changes in grid resolution, but this related only to the influence of resolution on the production of unphysical velocity fluctuations caused by the sharp transition in plant area density at canopy top.

Less attention was given to deep canopies over hilly and mountainous terrain. Numerical modelling studies of flow across forested hills and ridges were conducted to challenge the model results with experimental measurements or analytical predictions (Ross and Vosper, 2005; Tamura et al., 2007; Dupont and Brunet, 2008a; Ross, 2008; Grant et al., 2016). Patton and Katul (2009) investigated phase relationships between mean flow variables and turbulence statistics and their sensitivity to a change in leaf area density. The separation region was found to be ambiguous for sparse canopies while being well-defined within the canopy on the lee side of the ridge for dense canopies.

Ross (2011) and Chen et al. (2019) examined how topography-induced changes in the flow translate to scalar transport within the canopy. Scalars emitted near the ground exhibited larger spatial variability than those emitted in the upper canopy (see also Ross and Harman, 2015). Transport out of the canopy was enhanced compared to that over flat terrain, with a preferential route out of the canopy located over the region of separated flow. Ross and Baker (2013) considered the effects of a forest canopy covering partially hilly terrain. Flow separation was essentially limited to the forested region over the lee slope where an adverse pressure gradient is induced by the terrain. The differences in flow separation for different positionings of the forest were found to have a large impact of scalar transport out of the canopy.

In the present work, a simple canopy model is implemented in the Weather Research and Forecasting model. Large-eddy simulations using the standard roughness length approach and using the canopy model are evaluated using the 'Furry Hill' data (Finnigan and Brunet, 1995) for a neutral boundary-layer flow across a forested ridge. Simulations are carried out using a range of horizontal and vertical grid spacings in order to assess the impact that this has on the response of the flow to the canopy covered hill, hereafter referred to as a ridge to clarify the two dimensional profile. The modelling system is presented briefly in Sect. 3.4. The set-up of the modelling system and the design of the numerical experiments are described in Sect. 3.5. Numerical results and sensitivities to the horizontal grid spacing are analysed in Sect. 3.6. Conclusions are given in Sect. 3.7.

3.4 Modelling System

Numerical simulations were performed with the community Weather Research and Forecasting (WRF) modelling system, version $3.9.1$, and using its Advanced Research WRF (ARW) dynamical core. The ARW dynamical core integrates the fully compressible, non-hydrostatic equations of motion in flux form. The equations are discretised using a terrain-following mass-based coordinate system and a staggered grid of type Arakawa-C. Time integration was performed using a third-order Runge-Kutta scheme and a time-splitting technique with semi-implicit sound waves. A fifth-order Weighted Essentially Non-Oscillatory (WENO) scheme with a positive definite filter was selected for advection of momentum and scalar variables. The Coriolis force was excluded as the effects of the Earth's rotation on the flow are negligible at the scales of motion that are considered in the present work (see Sect. 3.5).

Canopy models have been developed and implemented in WRF by, for example, Ma and Liu (2019) and Arthur et al. (2019). However, these were not finalised until considerable work had already been done for this study. The term $\mathbf{F}_c$, defined by Equation (25), as an additional sink of momentum to the momentum equation within the canopy was therefore implemented by the authors. The 1.5-order turbulence closure scheme developed by Deardorff (1980) with a prognostic equation for sub-grid-scale (SGS) TKE, denoted by k_{SGS}, was used to determine the SGS fluxes from the resolved fields and the SGS TKE. In this scheme, the eddy viscosity of momentum K_m is

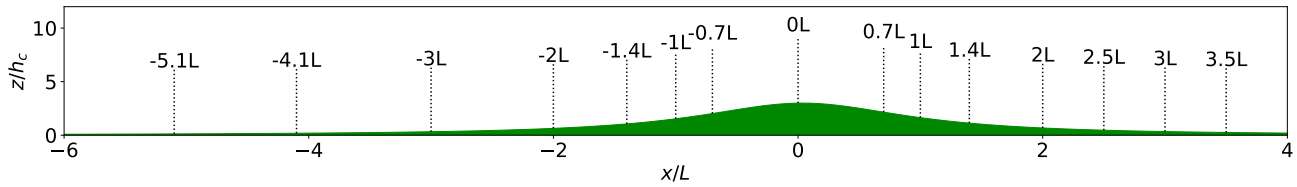

Figure 8: Terrain height z_g, normalised by the height of the canopy h_c, along the stream-wise direction x. The distance along x is normalised by the half-height width L of the ridge. The terrain is symmetric about $x = 0$ and uniform in the span-wise direction y (into the page). The vertical dotted lines indicate the positions where experimental data is available and the wind is moving from left to right

modelled as

$$K_m = C_k \, \lambda \, \sqrt{k_{\mathrm{SGS}}}, \tag{26}$$

where the diffusion coefficient $C_k = 0.10$ and the SGS mixing length scale λ was set equal to the cube root of the grid-cell volume $\Delta s = (\Delta \mathrm{x} \, \Delta \mathrm{y} \, \Delta \mathrm{z})^{1/3}$.

In the turbulence closure scheme proposed by Deardorff (1980) the SGS TKE dissipation is given by

$$\epsilon_v = C_\epsilon \, k_{\mathrm{SGS}}^{3/2} / \lambda, \tag{27}$$

where the dissipation coefficient $C_\epsilon = 0.93$, except in the first grid cell immediately above the surface, where C_ϵ is increased to 3.9 to mimic a 'wall effect' so as to prevent k_{SGS} from becoming unduly large there. Following Shaw and Schumann (1992), the standard viscous dissipation ϵ_v was augmented by an additional dissipation term,

$$\epsilon_c = 2 \, C_d \, a \, |\mathbf{u}| \; k_{\mathrm{SGS}}, \tag{28}$$

to represent the dissipation caused by the interactions between the air and the canopy.

3.5 Design of The Numerical Experiments

The 'Furry Hill' wind-tunnel experiment carried out by Finnigan and Brunet (1995) is used to evaluate the different methods of parametrising the canopy presented in the previous sections. In this experiment, a neutral atmosphere with a uniform background wind $U_b = 12 \, \mathrm{m \, s^{-1}}$ interacts with a forested ridge with a two dimensional profile of a 'witch of Agnesi' centred about $x = 0$ (see Fig. 8). Ground level z_g is defined as $z_g = H_e / [1 + (x/L_e)^2]$, where the height of the ridge $H_e = 0.15 \, \mathrm{m}$ and its half-height width $L_e = 0.42 \, \mathrm{m}$. For the artificial canopy used in the experiment, the height of the canopy was $h_{c,e} = 0.047 \, \mathrm{m}$, the plant area density $a_e = 10 \, \mathrm{m^{-1}}$ and the drag coefficient $C_{d,e} = 0.68$, leading to a canopy-drag length scale $L_{c,e} = (C_{d,e} \, a_e)^{-1} = 0.147 \, \mathrm{m}$. This artificial canopy was then surrounded by a rough surface of gravel with a diameter of $0.014 \, \mathrm{m}$ ($\approx h_{c,e}/3.36$).

The physical properties of the ridge and canopy are scaled up as proposed by Dupont and Brunet (2008a), so that the experiment represents atmospheric scales. This provides a ridge height $H = 30\,\mathrm{m}$, half-height width $L = 84\,\mathrm{m}$, canopy height $h_c = 10\,\mathrm{m}$, plant area density $a = 0.165\,\mathrm{m}^{-1}$ and drag parameter $C_d = 0.2$, leading to a canopy-drag length scale $L_c = (C_d\,a)^{-1} = 30.3\,\mathrm{m}$. Geometric similarity is achieved ($H/L = H_e/L_e = 0.36$), but a was increased slightly in comparison to the value of $0.16\,\mathrm{m}^{-1}$ used by Dupont and Brunet (2008a). This was done to achieve marginally closer values to the 'Furry Hill' experiment for the conditions $L_{c,e}/L_e = 0.35$ and $h_{c,e}/L_{c,e} = 0.32$, where these are $L_c/L = 0.36$ and $h_c/L_c = 0.33$ for the values used here. The canopy extends from $x/L = -9.35$ to 3.39 to match the location of the artificial canopy used in the experiment. For all simulations, the surrounding gravel surface is simulated using a roughness length of $z_0 = 0.0025\,h_c = 0.025\,\mathrm{m}$, approximately one tenth of the diameter of the scaled up gravel.

Simulations are performed with two nested domains and feedback was enabled, such that the lateral boundaries of the inner domain are set by the outer domain solution and the solution at the boundaries of the inner domain are fed back to the outer domain. The outer domain extends horizontally between $x/L = \pm 36$ and $y/L = \pm 10.6$. The inner domain, centred on $(x, y) = (0, 0)$, covers one third of this extent, between $x/L = \pm 12$ and $y/L = \pm 3.53$. It should be noted that the ridge and canopy are present in the inner and outer domains and both domains are run in large-eddy simulation (LES) mode. In the vertical, a terrain-following coordinate is used with 85 points from the surface to the top of the two domains at approximately $z/h_c = 20$ above the sections of flat ground. A hyperbolic tangent function is applied to the vertical grid spacings to compact the grid close to the ground, with grid spacings barely increasing above. The grid is stretched such that the lowest level has a height of approximately $h/h_c = 0.1$, providing 10 levels within the canopy. A lowest grid level height of $h/h_c = 0.2$ was also considered but the results are not shown because the difference between the two cases was negligible. The top of the two domains is frictionless and includes a $50\,\mathrm{m}$ deep Rayleigh damping layer to reduce numerical instabilities in the simulation (Klemp et al., 2008). Periodic boundary conditions are used at the lateral boundaries of the outer domain, which is given a sufficient extent in the stream-wise direction for the forested ridge to have no noticeable effect on the incoming flow at the inner domain. Horizontal grid spacings $\Delta x = \Delta y$ of 0.024, 0.048 and $0.071\,L$ (2, 4 and $6\,\mathrm{m}$) are considered for the inner domain and 0.071, 0.143 and $0.214\,L$ (6, 12 and $18\,\mathrm{m}$) for the outer domain, respectively. At the surface, no-slip conditions are imposed, the heat flux is set to zero and the momentum flux is calculated from wind velocity at the first grid point above the surface, using the logarithmic profile of Eq. (24) with a prescribed surface roughness length z_0.

The simulations are initialised with a wind speed of $17\,\mathrm{m\,s}^{-1}$ in the positive x-direction at all positions. The initial wind speed is larger than that of the upstream flow in the wind-tunnel experiment ($12\,\mathrm{m\,s}^{-1}$) so that the flow speed achieved after the spin-up period corresponds to that approaching the canopy in the experiment. After approximately 30 to 40 minutes of simulation time, the solution reaches a quasi-steady state, as shown in Fig. 9 by the relatively constant wind speed

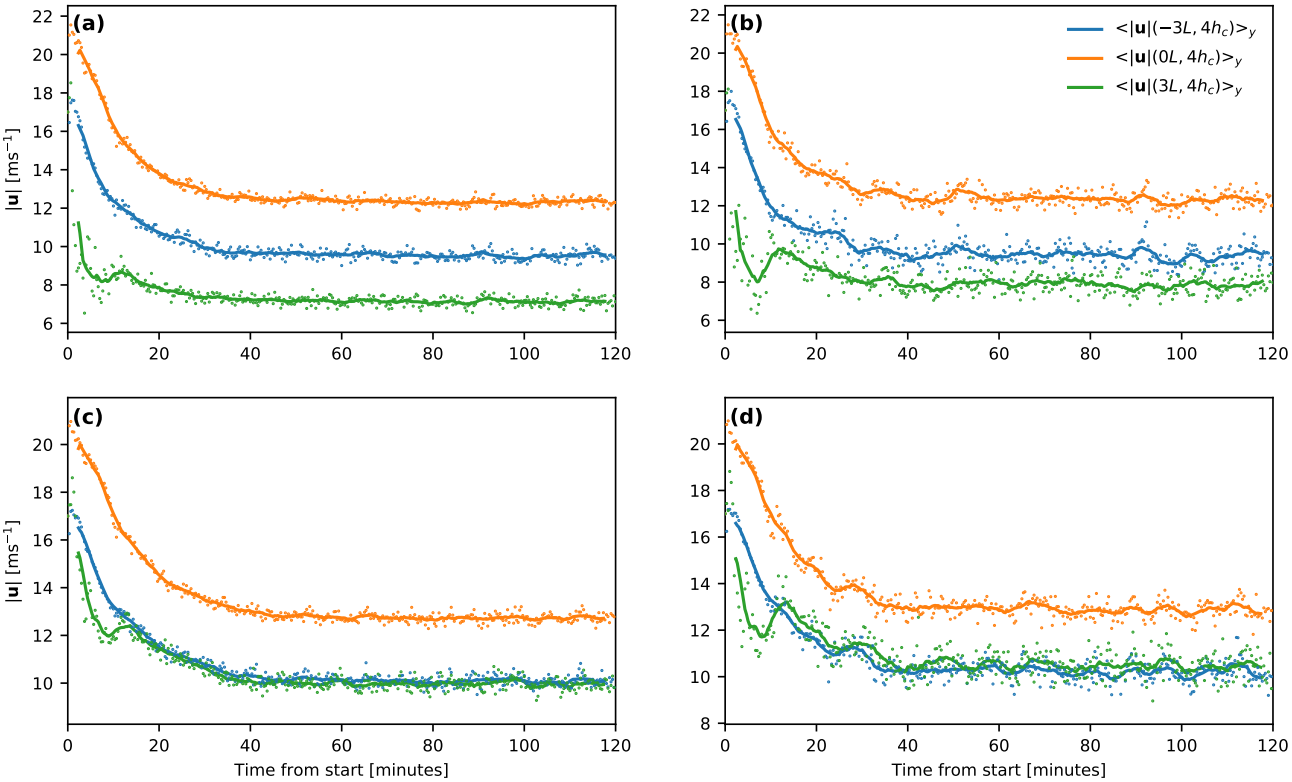

Figure 9: Wind speed $|\mathbf{u}|$ averaged in the y-direction for WRF-C6 **(a)** outer and **(b)** inner domains and for WRF-R6 **(c)** outer and **(d)** inner domains for positions around the ridge at $4\,h_c$ above ground level. The points show instantaneous wind speeds, while the solid lines show a 5 min moving average

after this time. While no forcing is applied to drive the flow, the 5 minute moving average of wind speed at the locations shown vary by no more than 3% in the outer domain and 6% in the inner domain for the time period after the first 45 minutes for all the simulations that were performed. To obtain numerically stable results, the vertical grid resolution and maximum flow speed demanded a model time-step $\Delta t = 0.025\,\mathrm{s}$, with data being exported at $20\,\mathrm{s}$ intervals. The 90 data points between minute 45 and minute 75 of the simulation are then used to calculate the mean velocity components $\langle u \rangle_{yt}$, $\langle v \rangle_{yt}$, $\langle w \rangle_{yt}$ and their variances $\langle u'^2 \rangle_{yt}$, $\langle v'^2 \rangle_{yt}$, $\langle w'^2 \rangle_{yt}$ in the x-, y-, z-directions, respectively, the momentum flux per unit mass $\langle u'w' \rangle_{yt}$ and TKE per unit mass $\langle k \rangle_{yt}$, where $\langle \rangle_{yt}$ denotes an average in both time and the span-wise direction y and $'$ represents a fluctuation from this averaged value. The velocity components and turbulence statistics collected by Finnigan and Brunet (1995) were normalised with the friction velocity $u_\star$ at canopy top at $x/L = -3$. In this work the results are presented in SI units and the normalisation of the measurements was reversed using $u_\star = 0.911\,\mathrm{ms}^{-1}$ calculated from their results.

In the following, the WRF simulations that use the canopy model introduced in Sect. 3.4 are given the reference WRF-C. The surface roughness length at the location of the canopy is set to $z_0 = 0.001\,h_c = 0.01\,\mathrm{m}$ (as in Shaw and Schumann, 1992) for these simulations. Another set of WRF simulations with reference WRF-R use only a change in surface roughness length to represent the artificial canopy, rather than modelling it explicitly. For WRF-R the roughness length used at the

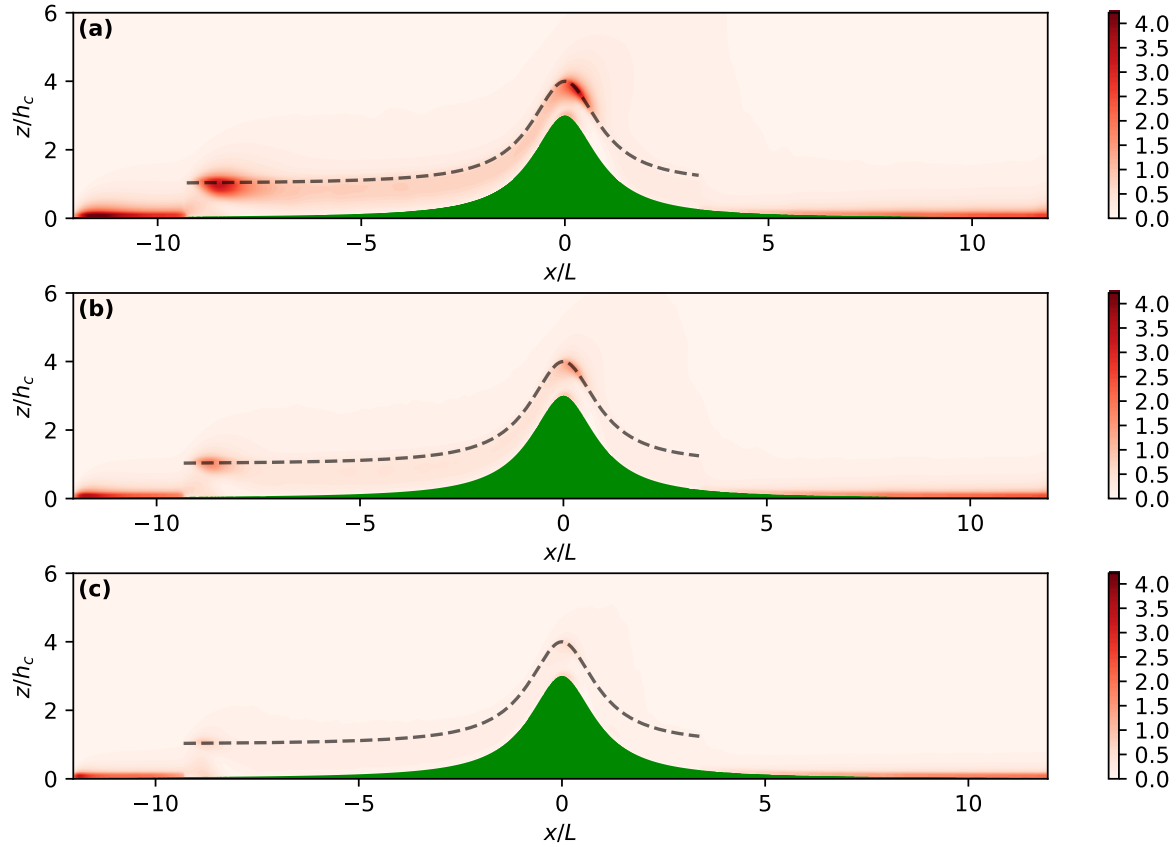

Figure 10: Ratio of sub-grid scale to resolved turbulence kinetic energy per unit mass, $\langle k_{\mathrm{SGS}} \rangle_{yt} / \langle k \rangle_{yt}$ for **(a)** WRF-C6, **(b)** WRF-C4 and **(c)** WRF-C2. The top of the simulated artificial canopy is indicated by a black dashed line

location of the canopy is $z_0 = 0.085\, h_c = 0.85\,\mathrm{m}$, determined to provide the closest agreement with the profile above the flat section of canopy in WRF-C when used in Equation (24). When discussing a specific simulation, the references WRF-C and WRF-R are followed by a number representing the horizontal grid spacing of the inner domain. For example, with horizontal grid spacing of $2\,\mathrm{m}$ $(0.024\, L)$ for a simulation using the explicit canopy model, the reference would be WRF-C2. The height of the lowest grid level is below the displacement height of the canopy and WRF is designed to only apply the effects of a roughness length in the bottom grid level. The results for WRF-R were elevated upwards by $z/h_c = 0.6$ such that the displacement height $d = 0.7\, h_c$ is within the lowest grid level. To keep notation simple in the following, height above ground level $h = z - z_g$ for WRF-R refers to that for WRF-C. Note that the ground is elevated at all positions, as this change in displacement height can not be properly applied at the leading and trailing edge of the canopy-covered region.

To ascertain that the model does resolve the most energetic scales of motion, the ratio of SGS to resolved TKE is shown in Fig. 10 for WRF-C. The SGS component of $\langle k \rangle_{yt}$ is negligible at all positions away from the canopy regardless of the horizontal grid spacing considered. In all cases, SGS TKE is up to 4 times greater in magnitude than resolved TKE at the lowest levels of the domain,

outside of the canopy. While it is not shown here, the same is true for all cases of WRF-R at the lowest grid levels but with a more significant contribution where the surface roughness increases to represent the canopy, especially around the peak of the ridge between $x/L = -1$ to 1. For WRF-C6 [see Fig. 10(a)], above the lowest grid levels, SGS TKE is most substantial (up to 3 times resolved TKE) at the top of the leading edge of the canopy ($x/L = -9$ to -8) and at canopy top near the peak of the ridge ($x/L = 0$ to 1). As the horizontal grid spacing is reduced, more of the turbulence generated in these locations within the canopy is resolved. Almost all TKE is resolved for WRF-C2 [see Fig. 10(c)]. It is therefore expected that the results for WRF-C2 will be closer to the measurements made in the 'Furry Hill' experiment than the other cases of WRF-C.

3.6 Results and Analysis

3.6.1 Model Evaluation

Pressure perturbations $\langle \Delta p \rangle_{yt}$ as a difference from the values at corresponding altitude z further upstream, taken here at $x/L = -3$, result from interaction with the forested ridge. The pressure perturbations induced by the canopy, Δp_c, and by the ridge, Δp_h, scale as $\Delta p_c \approx \rho\, U_b^2\, h_c/L_c$ and $\Delta p_h \approx \rho\, U_b^2\, H/L$, respectively, where ρ is density and U_b is the stream-wise velocity at corresponding altitude upstream of the ridge, taken here at $x/L = -5$ (Belcher et al., 2003). Simulated near-surface pressure perturbations for WRF-C and WRF-R are compared with measurements from the wind-tunnel experiment in Fig. 11(a) and (b), respectively. Recall that the simulated fields for WRF-R are valid from height $z = d$ and so pressure is compared at this height. The simulations capture reasonably well the measured decrease in pressure across the top of the ridge, although both over-predict the drop in pressure over the windward slope of the ridge. Immediately after the ridge-top the near-surface pressure for WRF-R follows the measurements closely, with the exception of WRF-R2 where the near-surface pressure increases over a shorter distance than for the other WRF-R simulations. For WRF-C, the distribution of near-surface pressure is similar to that measured but of a larger magnitude at all positions where measurements are available. This shows, as pointed out for instance by Ross and Vosper (2005), that the effective width of the ridge is increased for WRF-C when compared to WRF-R.

Simulated vertical profiles of the time and y-direction averaged stream-wise velocity and turbulence statistics to the counterpart measured profiles are presented in Fig. 12 and Fig. 13 for a selected subset of positions across the ridge. A quantitative evaluation in terms of root-mean-square error (RMSE), denoted by γ herein, for all measurement positions (x, h), illustrated in Fig. 8, is presented in Table 1. Vertical profiles of the time and y-direction averaged stream-wise velocity $\langle u \rangle_{yt}$ for WRF-C and WRF-R are shown respectively in Fig. 12(a) and Fig. 13(a). For WRF-C, these profiles are relatively close to those of the measurements, with similar $\gamma(\langle u \rangle_{yt})$ of 0.9 to $1.3\,\mathrm{m\,s^{-1}}$ over the range of horizontal grid spacings. For WRF-R the profiles of $\langle u \rangle_{yt}$ are similar to the measurements upstream of the ridge but, as a result of the weaker separation on the lee side of the ridge, there is

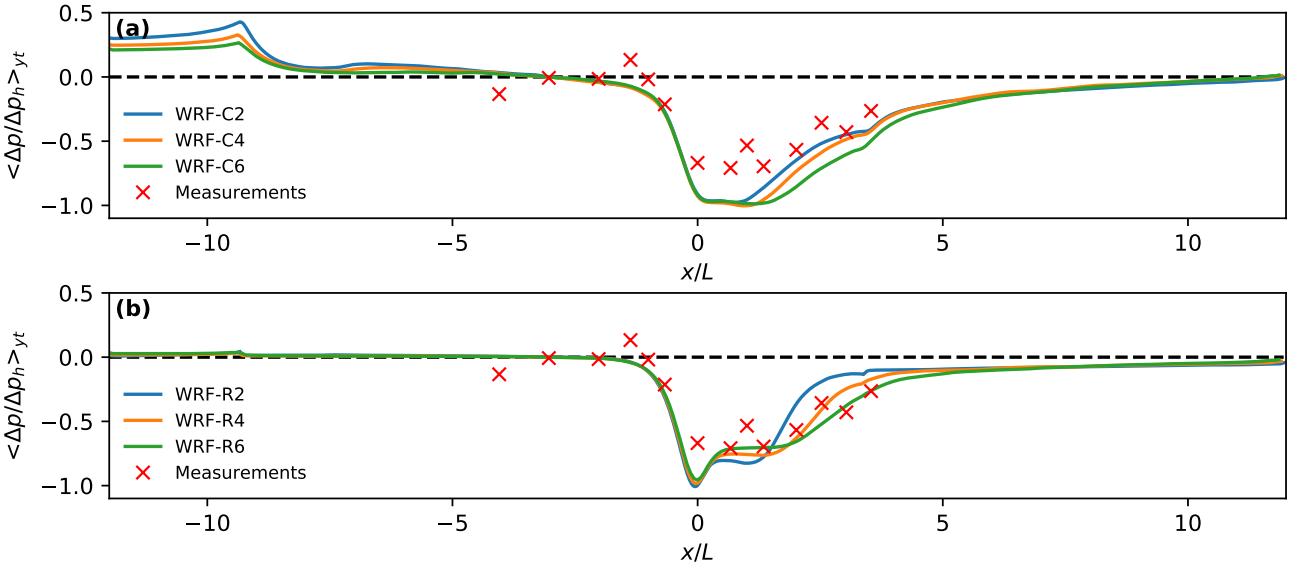

Figure 11: Simulated mean near-surface normalised pressure $\langle \Delta p / \Delta p_h \rangle_{yt}$ for **(a)** WRF-C and **(b)** WRF-R compared with the wind-tunnel measurements over the 'Furry Hill' from Finnigan and Brunet (1995) (see text for details). The pressure perturbation Δp is calculated relative to the value at $x/L = -3$

Table 1: Domain-wide root-mean-squared-error γ for the time and y-direction averaged stream-wise velocity $\langle u \rangle_{yt}$ (in $\mathrm{m\,s^{-1}}$), vertical momentum flux per unit mass $\langle u'w' \rangle_{yt}$ (in $\mathrm{m^2\,s^{-2}}$), stream-wise velocity variance $\langle u'^2 \rangle_{yt}$ (in $\mathrm{m^2\,s^{-2}}$), vertical velocity variance $\langle w'^2 \rangle_{yt}$ (in $\mathrm{m^2\,s^{-2}}$) and turbulence kinetic energy per unit mass $\langle k \rangle_{yt}$ (in $\mathrm{m^2\,s^{-2}}$), for all cases considered for WRF-C and WRF-R

Simulation	$\gamma(\langle u \rangle_{yt})$	$\gamma(\langle u'w' \rangle_{yt})$	$\gamma(\langle u'^2 \rangle_{yt})$	$\gamma(\langle w'^2 \rangle_{yt})$	$\gamma(\langle k \rangle_{yt})$
WRF-C2	0.90	0.70	1.03	0.58	1.20
WRF-C4	0.96	0.67	1.19	0.64	1.24
WRF-C6	1.03	0.56	1.26	0.75	1.13
WRF-R2	2.50	0.68	1.88	1.05	2.08
WRF-R4	1.92	0.62	1.67	0.98	1.69
WRF-R6	1.53	0.57	1.62	1.08	1.45

an excess of $\langle u \rangle_{yt}$ from approximately $z/h_c = 2$ to 6. This indicates that using a passive roughness is appropriate to represent the mean boundary-layer flow over flat ground for the case considered, but performance degrades significantly when the boundary-layer flow crosses over the ridge. When evaluated across all measurement positions (x, h), $\gamma(\langle u \rangle_{yt})$ is 49 to 178% larger for WRF-R than for WRF-C (see Table 1). The canopy model therefore performs better overall at reproducing the mean flow over a ridge covered in a forest canopy. Although the canopy model in WRF-C was implemented with the *sharp transition* of Ouwersloot et al. (2017), erroneous fluctuations in stream-wise velocity above the canopy were not seen.

The simulated $\langle u \rangle_{yt}$ on the lee side of the ridge is negative within the canopy for WRF-C and WRF-R, which is not the case for the measurements. However, the measurements of velocity must be interpreted with caution in the region of separated flow, since the crossed hot-wire probes that

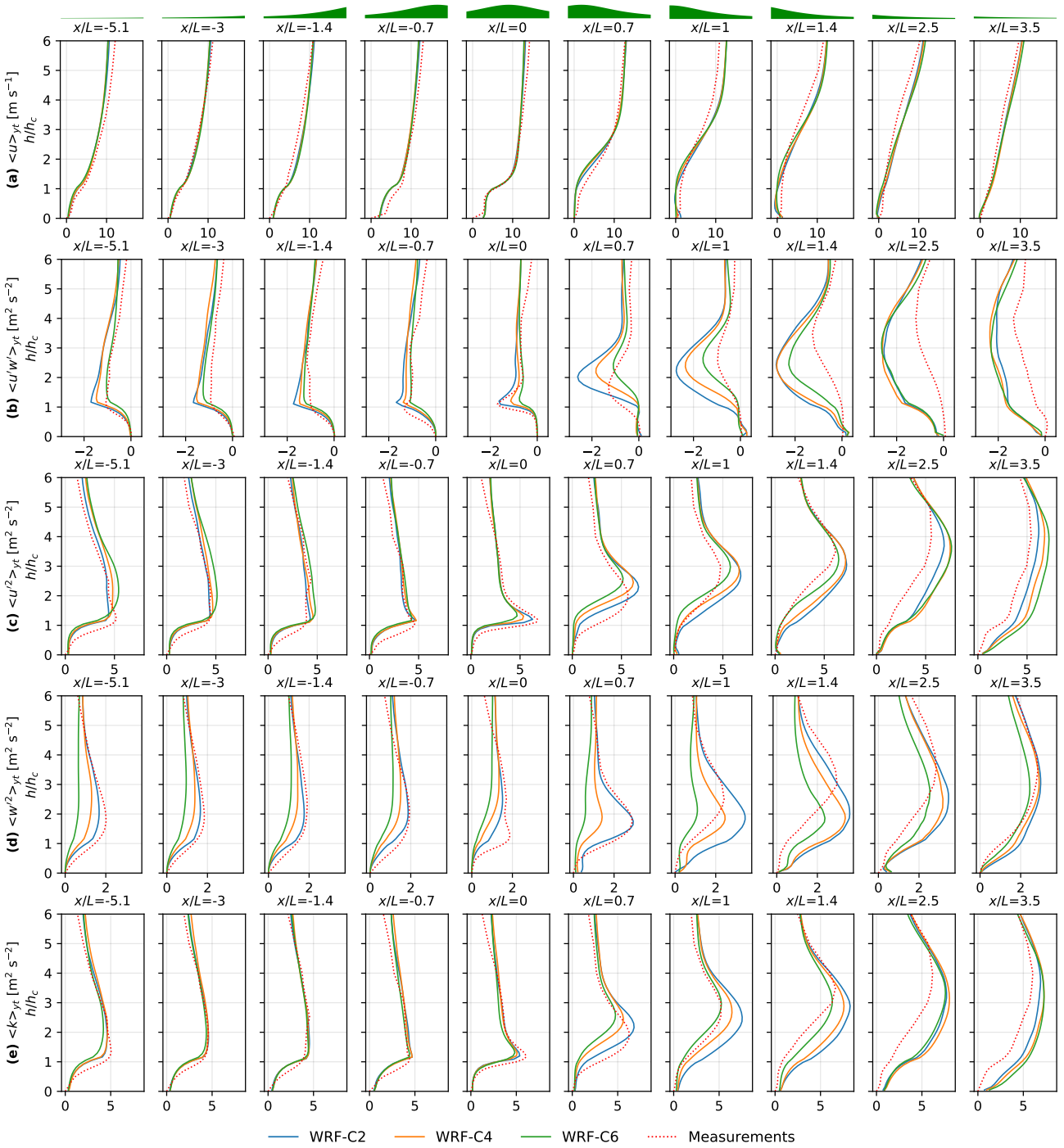

Figure 12: Vertical profiles of time and y-direction averaged (from the top to bottom panels) stream-wise velocity $\langle u \rangle_{yt}$, vertical momentum flux per unit mass $\langle u'w' \rangle_{yt}$, stream-wise velocity variance $\langle u'^2 \rangle_{yt}$, vertical velocity variance $\langle w'^2 \rangle_{yt}$ and turbulence kinetic energy per unit mass $\langle k \rangle_{yt}$ for WRF-C, compared with the wind-tunnel measurements over the 'Furry Hill' from Finnigan and Brunet (1995) (see text for details). A graphical representation of the slope in the terrain present around each profile is displayed at the top of the figure

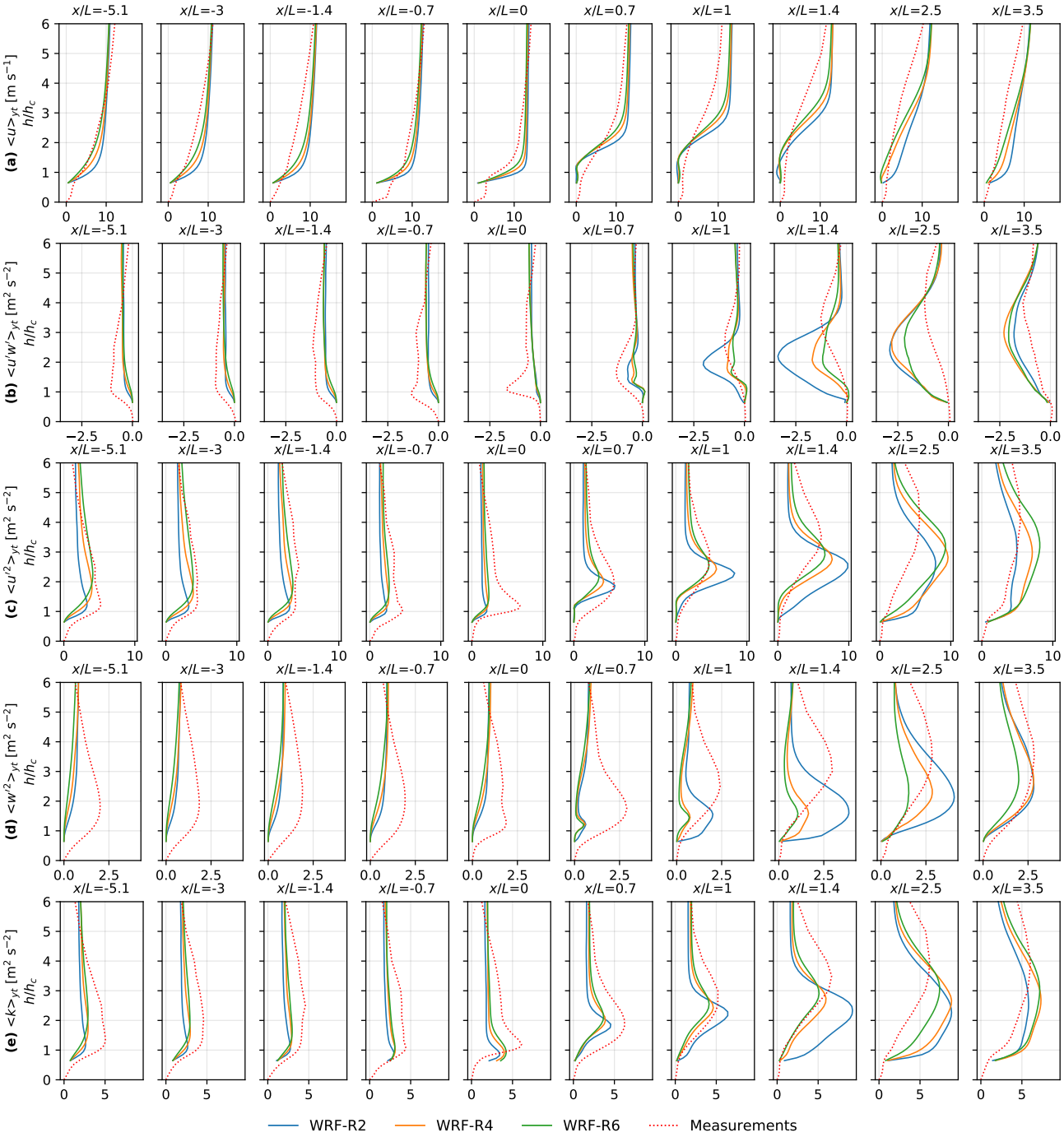

Figure 13: Vertical profiles of time and y-direction averaged (from the top to bottom panels) stream-wise velocity $\langle u \rangle_{yt}$, vertical momentum flux per unit mass $\langle u'w' \rangle_{yt}$, stream-wise velocity variance $\langle u'^2 \rangle_{yt}$, vertical velocity variance $\langle w'^2 \rangle_{yt}$ and turbulence kinetic energy per unit mass $\langle k \rangle_{yt}$ for WRF-R, compared with the wind-tunnel measurements over the 'Furry Hill' from Finnigan and Brunet (1995) (see text for details). A graphical representation of the slope in the terrain present around each profile is displayed at the top of the figure

were used are not appropriate for measuring a reversed flow. Using flow visualisation techniques, Finnigan and Brunet (1995) were able to identify a separation region $5.2\,L$ in length. This will be explored in Sect. 3.6.2 using cross-sections that show the full extent of the simulated separation region more clearly. WRF-C performs better than WRF-R not only for the mean flow but also for the majority of the turbulence statistics (see rows (b) to (e) in Fig. 12 and Fig. 13 and the second to fifth columns of Table 1). The RMSE γ for WRF-R are 29 to 83%, 44 to 81% and 28 to 73% larger than that for WRF-C for the stream-wise velocity variance $\langle u'^2\rangle_{yt}$, vertical velocity variance $\langle w'^2\rangle_{yt}$ and TKE per unit mass $\langle k\rangle_{yt}$, respectively.

In the region upstream of the ridge, the stream-wise velocity variance $\langle u'^2\rangle_{yt}$ takes a similar form to the measured profiles for both WRF-C and WRF-R, with WRF-C closer to the measured values than WRF-R and WRF-R2 performing particularly poorly above the canopy. The vertical velocity variance $\langle w'^2\rangle_{yt}$ and vertical momentum flux per unit mass $\langle u'w'\rangle_{yt}$ below $z/h_c = 5$ in the upstream region are minimal for all cases for WRF-R in comparison to the corresponding measurements. This is a clear indication that the roughness-length approach to modelling the effects of a canopy does not generate the level of turbulence seen in the wind-tunnel measurements, at least over flat ground. Conversely, WRF-C is able to reproduce most turbulence statistics accurately, with $\langle u'^2\rangle_{yt}$ and $\langle k\rangle_{yt}$ agreeing well with the measured profiles. The magnitude of the peak in $\langle w'^2\rangle_{yt}$ is reproduced well by WRF-C2; it is between 4 and 16% of the measured peak value in the upstream region. However, the simulations with larger horizontal grid spacings under-predict $\langle w'^2\rangle_{yt}$, with peak values in this region 22 to 37% smaller for WRF-C4 and 40 to 69% smaller for WRF-C6. The WRF-C simulations tend to over-predict the magnitude of $\langle u'w'\rangle_{yt}$ above the canopy, with WRF-C6 performing slightly better than WRF-C4 and WRF-C2 in the upstream region.

As the flow reaches the top of the ridge, at $x/L = 0$, a peak forms in the measured vertical momentum flux per unit mass $\langle u'w'\rangle_{yt}$ within close proximity of the top of the canopy. This is reproduced well by WRF-C2, but WRF-C4 and WRF-C6 under-predict this peak value respectively by 36 and 56%. For WRF-R this peak is not present for any of the horizontal grid spacings used. A similar peak in TKE per unit mass $\langle k\rangle_{yt}$ is also seen in the measurements at this location. In carrying out simulations similar to those discussed here, Dupont and Brunet (2008a) and Ross and Vosper (2005) reported large peaks in $\langle k\rangle_{yt}$ near the displacement height of the canopy at ridge-top when using a change in roughness length at the surface to represent the canopy. While this was not seen in the results shown here, such an excess was present in the results of preliminary simulations carried out by the authors when considering non-neutral conditions. The peaks in $\langle k\rangle_{yt}$ for WRF-R at this location are approximately 50% smaller than the measured values, with WRF-R6 and WRF-R4 11 to 12% closer to the measured peak value than WRF-R2. The peak values of $\langle k\rangle_{yt}$ for WRF-C are within 12 and 23% of the measured peak values, with smaller horizontal grid spacings providing the closest agreement. The differences between the ridge-top profiles for the different grid-spacings are minimal at most locations, but while WRF-C2 provides the best result for the canopy model simulations, WRF-R6 provides the best result for the simulations using only a change in roughness

length at the surface.

As the flow proceeds downstream, all turbulence statistics begin to respond more strongly to the presence of the forested ridge. For the simulations and measurements, the momentum flux $\langle u'w' \rangle_{yt}$ displays a single peak, the location of which increases in height above ground level between $x/L = 0$ and 2.5 (see Fig. 12(b) and Fig. 13(b)). It should be noted that these figures show height above ground level. Thus, while a peak in a profile appears to be displaced upwards, it actually remains at a fairly constant altitude, as will be shown in the cross-sections of Sect. 3.6.2.

For WRF-C, the peak in $\langle u'^2 \rangle_{yt}$ increases in height downstream over a similar range of x/L to that seen in the measurements. However, for $\langle w'^2 \rangle_{yt}$ the peak rises initially but then remains between $h/h_c = 1.5$ to 2.5 over $x/L = 0.7$ to 2.5. $\langle u'w' \rangle_{yt}$ and $\langle k \rangle_{yt}$ correspondingly increase more rapidly at low levels than higher above the ground. This leads to the peak value occurring lower than that measured in the wind tunnel and to closer agreement with the measurements above the peak than below. For WRF-R the peak value of $\langle w'^2 \rangle_{yt}$ occurs slightly closer to the ground, between $h/h_c = 1$ to 2. The magnitude of this peak is not reproduced well by any of the WRF-R simulations at $x/L = 0.7$. For $x/L = 1$ to 1.4, WRF-R6 and WRF-R4 remain close to the measured profiles of $\langle w'^2 \rangle_{yt}$ until $h/h_c = 1.5$ but under-predict above this height until $h/h_c = 6$. This is also true for the peak in $\langle w'^2 \rangle_{yt}$ for WRF-R2, except by $x/L = 1.4$ the peak value is over-predicted by 32% while still $1.5\,h_c$ lower than the height of the peak in the measurements. The peaks in the downstream profiles of $\langle u'^2 \rangle_{yt}$ for WRF-R rise over a range of x/L more in line with the measurements and WRF-C than those for $\langle w'^2 \rangle_{yt}$. However, by $x/L = 1.4$ these peaks are 0.5 to $1\,h_c$ lower than those in the measurements, with this discrepancy most acute in the case of WRF-R2. This leads to the peak in $\langle u'w' \rangle_{yt}$ for WRF-R occurring up to $1.5\,h_c$ lower than the peak in the measurements, compared to $1\,h_c$ lower for WRF-C. As WRF-R reproduces $\langle u'w' \rangle_{yt}$ more accurately downstream of the ridge and less accurately before the ridge and *vice versa* for WRF-C, the corresponding γ for this quantity are within 2 to 8% when comparing the two methods of parametrising the canopy.

The results produced by WRF-C are very similar to those that were produced in the simulations carried out by Dupont and Brunet (2008a). The peak in $\langle u'w' \rangle_{yt}$ immediately downstream of the ridge also occurs at a position in the vertical that is different from that of the measurements and is over-predicted by a similar amount, but by $x/L = 3.5$ the profile is more similar to the measurements than WRF-C. The simulations from both works follow the profiles of $\langle u'^2 \rangle_{yt}$ and $\langle k \rangle_{yt}$ closely. Similar but small over-predictions in these quantities below $z/h_c = 3$ are present in both cases, but larger for WRF-C. While WRF-C2 performs considerably better in reproducing $\langle w'^2 \rangle_{yt}$ upstream of the ridge, the results by Dupont and Brunet (2008a) are closer to the measurements downstream of the ridge. The vertical position of the peak in $\langle w'^2 \rangle_{yt}$ is also lower than in the measurements at $x/L = 2$ but follows the measurements better than any of the WRF-C simulations. It is worth noting that Dupont and Brunet (2008a) do not provide the value for $u_\star$ used for normalisation and this could lead to differences in the magnitudes of the various statistics between those results and the results of WRF-C. The similarity between the height of the wake seen in the WRF-C simulations

and those of Dupont and Brunet (2008a) would suggest that the difference to the measurements is a result of the experiment being scaled up. It is therefore possible that further similarity conditions are required when scaling up experiments studying flows over ridges covered with a canopy. The 'Furry Hill' experiment was studied by Ross and Vosper (2005) using numerical simulations of the same scale as that of the wind tunnel with a canopy model and using only a change in roughness length at the surface to parametrise the artificial canopy. However, it is difficult to compare WRF-C and WRF-R to those results due to the reduced vertical extent of the plotted data and the small size of the plots themselves.

There are some considerable differences between the profiles of turbulence statistics for the equivalent simulations with different horizontal grid spacings. Upstream of the ridge, WRF-C2 provides the closest agreement with the measurements but, as the flow proceeds past the ridge, WRF-C6 tends to produce better results. The finest grid appears to be reproducing the fine scales of turbulence above the flat section of canopy upstream of the ridge well, but is not performing so well in the wake, where turbulence is generated by the combination of the canopy and the ridge. The profiles of turbulence statistics for WRF-R6 and WRF-R4 are very similar across most positions, although with considerable differences to the measured values. However, there are large differences between the profiles for WRF-R2 and those with a more coarse grid spacing. The TKE $\langle k \rangle_{yt}$ and vertical momentum flux $\langle u'w' \rangle_{yt}$ are over-predicted to varying degrees in all of the simulations below $h/h_c = 5$ to 6 in the downstream region. While this is still true at $x/L = 3.5$, the differences between equivalent simulations of different horizontal grid spacings are greatly reduced, with profiles of $\langle k \rangle_{yt}$ much closer to the measured profiles. The horizontal grid resolution of the simulations has a strong influence on the properties of the flow in close proximity to the forested ridge, but does not make a large difference to the properties of the flow further downstream.

While the magnitude of the turbulence statistics generated from WRF-R and WRF-C both differ from the measurements in some positions, the forms of the vertical profiles are more closely reproduced by WRF-C. The response to the forested ridge for WRF-R generally lies between what would be expected for a ridge with negligible roughness and that for WRF-C. The roughness-length approach to modelling the effects of a canopy does modify the dynamics correctly but not sufficiently for the extensive, tall canopy considered in the present work. In sum, the comparison of model results with the 'Furry Hill' data shows that the implementation of the canopy model in WRF is a significant improvement over the roughness-length approach for both the mean flow and the turbulence statistics when considering a ridge covered by a tall canopy for the range of horizontal grid spacings considered herein. While WRF-C provides better results than WRF-R immediately downstream of the ridge, there are still clearly deficiencies in the model's ability to reproduce the magnitude and height of the wake.

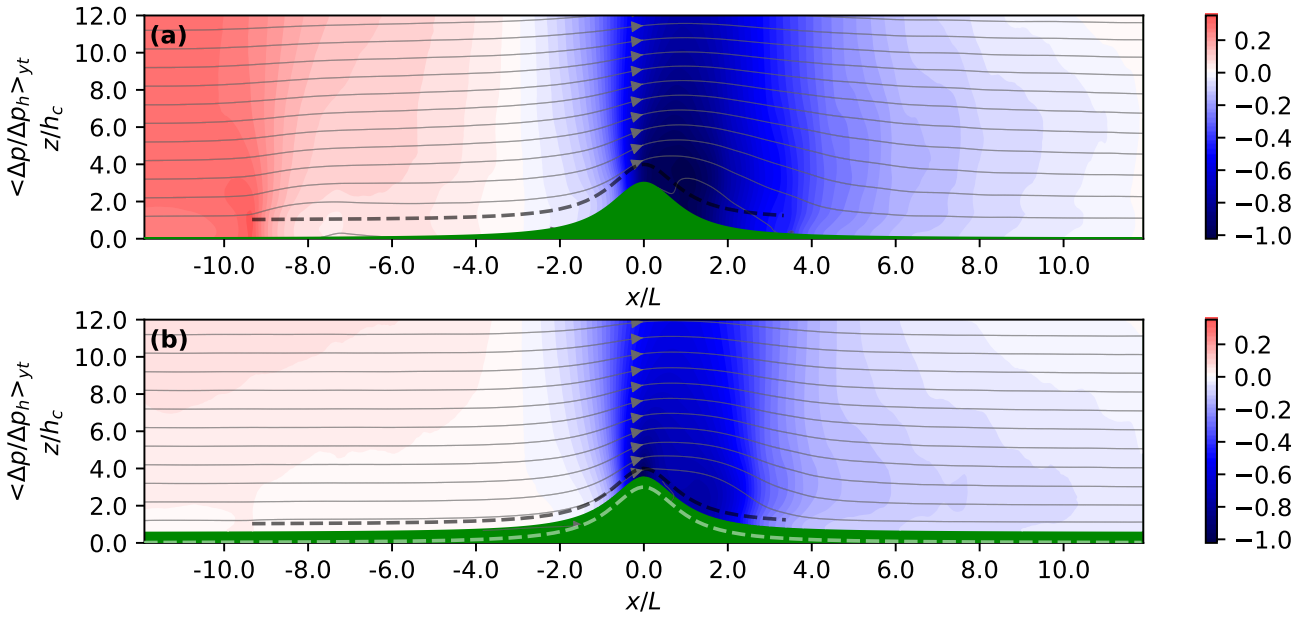

Figure 14: Simulated mean normalised pressure perturbation $\langle \Delta p \rangle_{yt}$ for **(a)** WRF-C4 and **(b)** WRF-R4. The pressure perturbation is calculated relative to the value at the corresponding height at $x/L = -3$. The top of the simulated artificial canopy is indicated by a black dashed line. The light grey lines show mean flow streamlines originating at regular height intervals above the flat ground at $x/L = -12$. The dashed white line in **(b)** represents the effective ground level of the vertically displaced WRF-R4 simulation (see Sect. 3.5 for details)

3.6.2 Flow Features

Using the scaling arguments presented at the beginning of Sect. 3.6.1, since $h_c/L_c \sim H/L$ in the present work, there ought to be an interplay between the canopy and the ridge on the generation of drag on the ridge surface. The mean pressure perturbation field $\langle \Delta p \rangle_{yt}(x, z)$ across the finer-resolved domain is shown in Fig. 14 for WRF-C4 and WRF-R4. Significant differences can be noticed between the two simulations, most notably the presence of a local maximum and minimum in pressure respectively before and after the leading edge of the canopy at $x/L = -9.35$ for WRF-C (see Fig. 14a). The local minimum at $x/L = -7.5$ induces an adverse pressure gradient, thereby decelerating the flow (see Belcher et al., 2003, for a detailed description of the adjustment of a turbulent boundary layer to a canopy of roughness elements). In contrast, pressure is essentially horizontally uniform upstream of the ridge for WRF-R with only a slight decrease caused by the change in roughness length at $x/L = -9.35$. The flow is assumed to adjust to the canopy at the location where $\langle w \rangle_{yt}/u_{\text{ref}} = 0.01$, with u_{ref} taken as $\langle u \rangle_{yt}$ at height $h/h_c = 2$ over the flat section of terrain with no canopy present at $x/L = -10.5$. For all cases of WRF-C this adjustment length $L_a \approx 3.8\, L_c$, which is smaller than the range 4.5–$6\, L_c$ predicted by Belcher et al. (2012). However, it is in line with the values of $3\, L_c$ and $4\, L_c$ found in the analytical and numerical studies of Belcher et al. (2008) and Dupont and Brunet (2009), respectively. It should be noted that the analytical methods use the location where the vertical velocity has dropped to the friction velocity $u_\star$; however

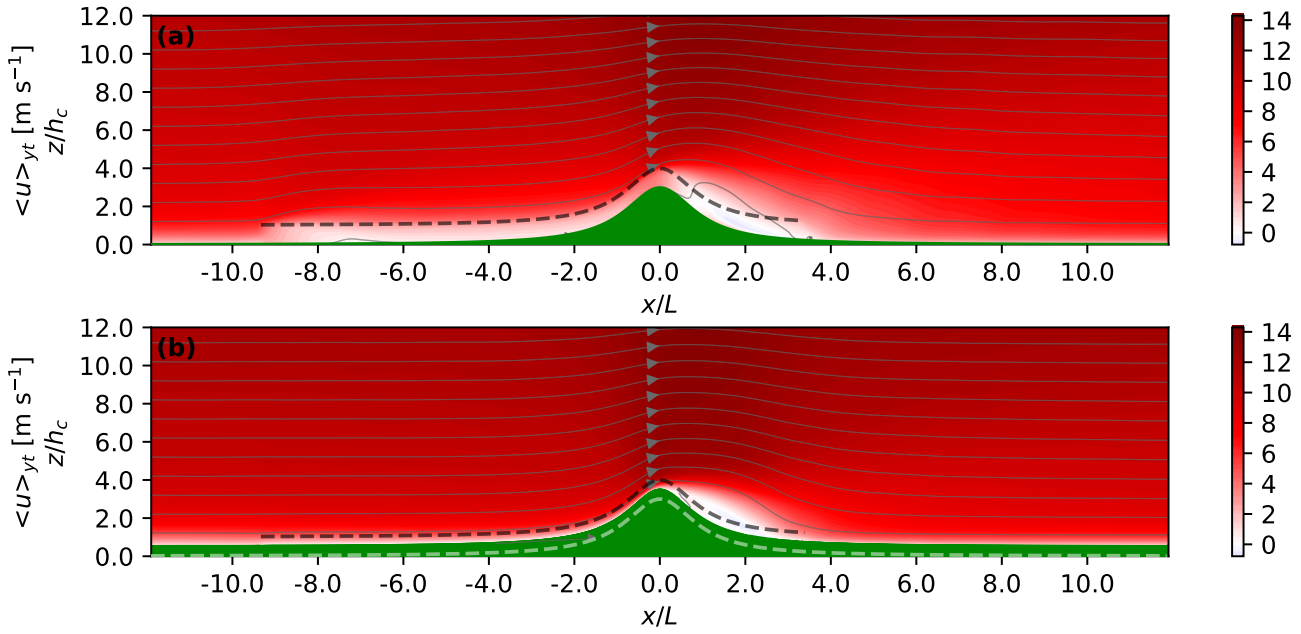

Figure 15: Simulated mean stream-wise velocity $\langle u \rangle_{yt}$ for **(a)** WRF-C4 and **(b)** WRF-R4. The top of the simulated artificial canopy is indicated by a black dashed line. The light grey lines show mean flow streamlines originating at regular height intervals above the flat ground at $x/L = -12$. The dashed white line in **(b)** represents the effective ground level of the vertically displaced WRF-R4 simulation (see Sect. 3.5 for details)

for WRF-C the vertical velocity is always less than the friction velocity at canopy top.

Pressure decreases and hence the wind speed increases as the flow approaches the top of the ridge. In the case of a ridge with no canopy and negligible surface roughness, the pressure minimum is located directly above the ridge. When a canopy is present on the ridge this pressure minimum is displaced to a position downstream from the ridge-top (see Fig. 14). For WRF-C the area of lowest pressure extends over the majority of the slope on the lee side of the ridge for all horizontal grid spacings. A pressure minimum occurs immediately downstream of the ridge-top just above the canopy at $x/L = 0.95$, $h/h_c = 1.7$ for WRF-C4. Changing the horizontal grid spacing does not modify the height of this minimum by more than $0.1\,h_c$. However larger grid spacings result in a more significant displacement of this minimum in the stream-wise direction, $x/L = 0.67$ for WRF-C2 and $x/L = 1.14$ for WRF-C6 (not shown). While there is an area of reduced pressure over a similar extent for WRF-R, the location of minimum pressure is at the top of the ridge at the lowest modelled level at $x/L = 0$, $h/h_c = 0.6$ for all horizontal grid spacings considered.

On the lee side of the ridge the adverse pressure gradient leads to flow separation which, in turn, causes the adverse pressure gradient to extend further downstream as if the ridge has been extended in the downstream direction. This effect is more significant for WRF-C than for WRF-R, although the pressure field for WRF-R is much closer to that for WRF-C than to that which would be expected for a ridge with negligible roughness. The pressure close to the ground readjusts downstream of the ridge over a shorter distance for WRF-R than for WRF-C (cf. Fig. 11). Coupling between the

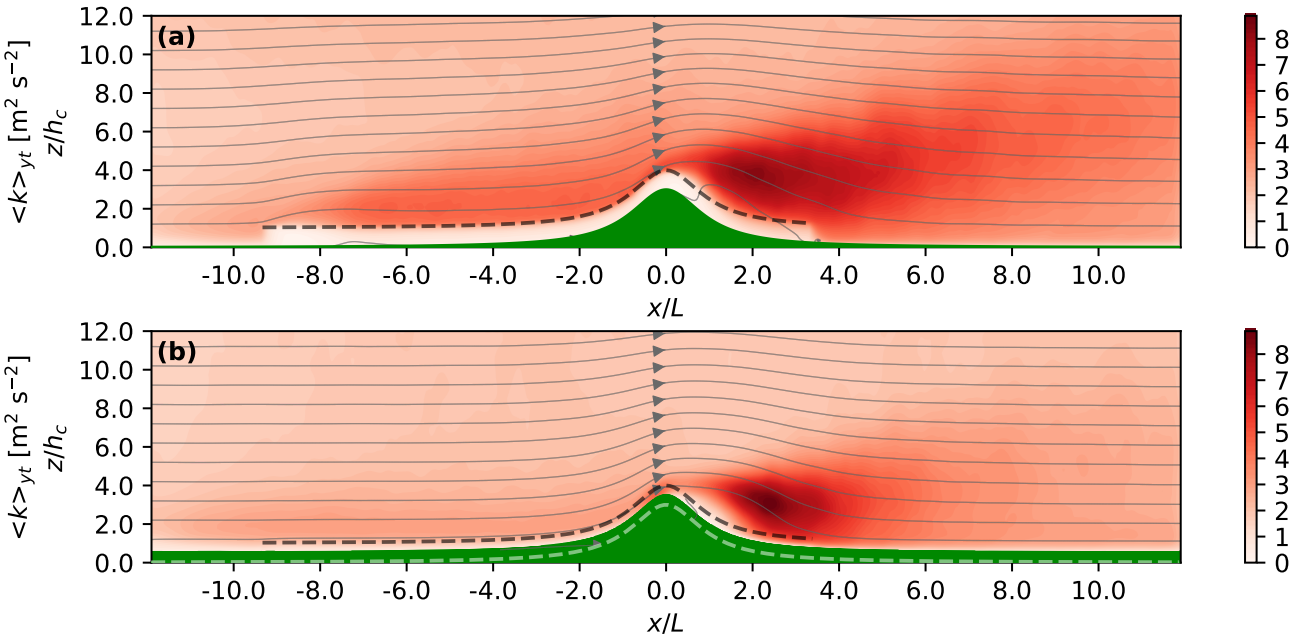

Figure 16: Simulated turbulence kinetic energy per unit mass $\langle k \rangle_{yt}$ for **(a)** WRF-C4 and **(b)** WRF-R4. The top of the simulated artificial canopy is indicated by a black dashed line. The light grey lines show mean flow streamlines originating at regular height intervals above the flat ground at $x/L = -12$. The dashed white line in **(b)** represents the effective ground level of the vertically displaced WRF-R4 simulation (see Sect. 3.5 for details)

out-of-phase flows within and above the canopy results in a reduced pressure gradient (reduced over-speeding) over the ridge for WRF-C compared with that for WRF-R. The separation region extends over $4\,L$ in length over the ground surface for all cases for WRF-C, in line with the experimental data of Finnigan and Brunet (1995) and numerical data of Ross and Vosper (2005) and Dupont and Brunet (2008a), compared with $3\,L$ for WRF-R4 (see Fig. 15). However, the horizontal extent of the separation region at the surface for WRF-R would be of comparable extent if the flow could be visualised below the displacement height d. The horizontal grid spacing does not modify the length of the separation region significantly for WRF-C. For WRF-R the horizontal extent of the separation region increases with horizontal grid spacing, from $2.2\,L$ in length for WRF-R2 to $3.5\,L$ for WRF-R6.

A wake is created on the lee side of the ridge, centred vertically on the region of maximum wind shear above the separation region as shown in Fig. 16 for $\langle k \rangle_{yt}$ (although a similar structure is visible in all other turbulence statistics). The vertical differential in wind speed at the top of the ridge is smaller for WRF-R than that at canopy height at the top of the ridge for WRF-C. Therefore, the wake angle and the intensity of turbulence within the wake are larger for WRF-C than for WRF-R. There is evidence of Kelvin-Helmholtz billows forming in the wake for both simulations. Turbulence is suppressed in the canopy for WRF-C while fluctuations are clearly visible near the surface for WRF-R. The vertical spread or depth D of the turbulent wake region follows a power law of the form $D = A\ (x - x_0)^{\alpha}$, as presented by Kaimal and Finnigan (1994) in reference to Taylor (1988).

In this formulation x_0 is a virtual origin situated before the ridge and A is a constant. Kaimal and Finnigan (1994) pointed out that theory, wind-tunnel and field experiments have not decided whether α should be equal to 0.5 or 1. The power α that best fit the wakes in the simulations presented here is in the range $0.6 - 0.7$ with x_0 taken as $x/L = -3$.

3.7 Conclusions and Discussion

Results from numerical model simulations of neutral boundary-layer flow across a forested ridge using a canopy model (WRF-C) or a bare surface with an increased roughness z_0 at the location of the canopy (WRF-R) using a range of resolutions were analysed and compared. The main conclusions, along with some discussion, are given below.

- The speed of the flow in the stream-wise direction is closer to the counterpart wind-tunnel measurements for WRF-C than for WRF-R. As is expected, the reduced canopy drag for WRF-R leads to an over-estimation of the wind speed above the canopy, which becomes larger as the flow proceeds downstream.

- WRF-C captures the measured turbulence statistics significantly better than WRF-R. The boundary layer has very little turbulence upstream of the ridge for WRF-R with a particular deficiency in the vertical velocity variance $\langle w'^2 \rangle_{yt}$.

- While the forested ridge in WRF-R generates turbulence close to the ground, the vertical extent of these turbulent structures does not reach as far above the ground as those seen in the measurements or in WRF-C.

- For WRF-R the horizontal extent of the separation region increases as the horizontal grid spacing is increased. This is not seen in WRF-C, where the separation region was of comparable extent for each horizontal grid spacing considered.

- The discrepancies between the experimental measurements and simulated values of stream-wise velocity and the various turbulence statistics are reduced by reducing the horizontal grid spacing for WRF-C.

- While it might be expected for a finer horizontal resolution to improve the results of WRF-R, the discrepancy with the measurements is actually increased, as is discussed below.

The RMSE γ between the measured and modelled profiles at the positions shown in Fig. 8 varies between the different turbulence statistics and mean stream-wise velocity for different horizontal grid spacings for WRF-C and WRF-R. In general, WRF-C provides closer results to the measurements when a smaller horizontal grid spacing is used, while the WRF-R simulations provide closer results at larger grid spacings for the case considered here. The RMSE for vertical momentum flux $\gamma(\langle u'w' \rangle_{yt})$

and TKE $\gamma(\langle k \rangle_{yt})$ do not follow this trend for WRF-C, with the largest grid spacing providing the best result in the reproduction of both statistics. However, this discrepancy is predominantly due to the turbulence occurring directly after the peak of the ridge at the profiles between $x/L = 0.7$ and 1.4. In this region there is a large over-prediction in $\langle w'^2 \rangle_{yt}$ at low levels and the closest simulated profiles to the measurements shift from WRF-C2 to WRF-C6 as the flow moves downstream. The stronger response to the ridge at low levels when smaller horizontal grid spacings are used leads to an even greater over-prediction in $\langle u'w' \rangle_{yt}$ and, as the difference to the measurements is large here, $\gamma(\langle u'w' \rangle_{yt})$ is heavily influenced by these profiles. The smaller grid spacings also lead to an over-prediction of $\langle k \rangle_{yt}$ in this region, but the difference this makes to $\gamma(\langle k \rangle_{yt})$ is reduced by the smaller difference in magnitude to the measured profiles. The fact that WRF-C2 is closer to the measurements before and after the ridge leads to $\gamma(\langle k \rangle_{yt})$ for WRF-C2 being only 6% larger than for WRF-C6, while for $\gamma(\langle u'w' \rangle_{yt})$ WRF-C2 is 25% larger. For WRF-R, $\gamma(\langle u'w' \rangle_{yt})$ and $\gamma(\langle k \rangle_{yt})$ reduce with increasing horizontal grid spacing in line with the other statistics. However, $\langle w'^2 \rangle_{yt}$ is reproduced poorly for all grid spacings, with $\gamma(\langle w'^2 \rangle_{yt})$ remaining at approximately $1\,\mathrm{m^2\,s^{-2}}$.

The larger discrepancies between the measurements and the counterpart numerical results, when smaller horizontal grid spacings are used, is also likely due to a compounding of errors. The dynamics of the flow in and around the canopy is not properly modelled when the canopy is represented only by a change in roughness length at the surface, as for WRF-R. When the horizontal grid spacing is reduced there are a larger number of grid cells over which errors can accumulate. For WRF-C the flow is more accurately reproduced over the flat terrain for which the canopy model used was devised. However, immediately downstream of the ridge, the smallest grid spacing is not providing a significant improvement to the reproduction of turbulence in the wake region. This may indicate that the canopy model used for WRF-C requires improvement to properly reproduce canopy dynamics in complex terrain. However, this canopy model is representing an evenly spaced array of cylindrical stalks as a homogeneous, porous block and so inconsistencies are always likely to be present.

For each of the simulations performed here, with a vertical resolution at the surface of $0.1\,h_c$, a corresponding simulation was carried out with a vertical resolution of $0.2\,h_c$. These have not been shown here as the differences between these two sets of simulations were negligible at all positions, other than a shift of approximately $z/h_c = 0.1$ in the height of peak values at canopy top due to the larger vertical extent of the grid cells. When a forest canopy is represented using an increase in roughness length at the surface and vertical resolution smaller than that of canopy elements, it is necessary to elevate the ground to the displacement height of the canopy. As this is not practical in numerical simulations, it is difficult to accurately reproduce the modification to the flow by the leading or trailing edge of the canopy using such a method. An additional simulation was performed with a bottom grid cell height of $h/h_c = 1.2$, using the roughness length approach but without displacing the ground. Results were found to have the same deficiencies as the other WRF-R simulations, with little to no response to the canopy visible in the turbulence statistics (not shown). Hence, a change in roughness length cannot replicate the effects of a relatively tall canopy

in the modulation of the flow speed over a ridge. An explicit treatment of the canopy represents a significant improvement over the roughness-length approach. However, it does require a fine spatial resolution in the vertical and the horizontal to include model layers within the canopy and to model turbulence in a large-eddy simulation mode. The high spatial resolution of the simulation leads to steeper slopes in the orography, which set constraints on the time-step (Connolly et al., 2020). Further research will be required to determine the effectiveness of this canopy model if coarser spatial resolutions are required.

While the results presented herein are for a fairly idealised terrain geometry and set of initial and boundary conditions, the results have important practical implications for the assessment and management of wind and pollution in the atmosphere within complex terrain. In the interest of comparing to the measurements of Finnigan and Brunet (1995), the current study was limited to geometry of the hill and canopy in their experiment with $L_c/L = 0.36$ and $h_c/H = 0.33$. For this case it appears that a horizontal resolution of $0.024\,L$ ($0.066\,L_c$) and a vertical resolution of 0.1 to $0.2\,h_c$ was appropriate to reproduce the flow over a forested ridge using a canopy model with vertical extent. Further work is required to explore a wider range of hill geometries and canopy properties and extents at different resolutions, as well as real-case studies that are likely to demand coarser grid resolutions. However, this will require considerably more experimental data on canopy flows in complex terrain to be collected.

3.8 Acknowledgements

The authors thank Dr. Sylvain Dupont for the provision of data from the paper by Dupont and Brunet (2008a). Numerical model simulations were performed using the University of Hertfordshire high-performance computing facility.

3.9 References

T. Allen. Flow over hills with variable roughness. *Boundary Layer Meteorology*, 121:475–490, 2006. doi:10.1007/s10546-006-9086-0.

R. S. Arthur, J. D. Mirocha, K. A. Lundquist, and R. L. Street. Using a canopy model framework to improve large-eddy simulations of the neutral atmospheric boundary layer in the weather research and forecasting model. *Monthly Weather Review*, 147(1):31–52, 2019. doi:10.1175/MWR-D-18-0204.1.

J. Bastin, Y. Finegold, C. Garcia, D. Mollicone, M. Rezende, D. Routh, C. M. Zohner, and T. W. Crowther. The global tree restoration potential. *Science*, 365:76–79, 2019. doi:10.1126/science.aax0848.

S. Belcher, I. Harman, and J. Finnigan. The wind in the willows: Flows in forest canopies in

complex terrain. *Annual Review of Fluid Mechanics*, 44(1):479–504, 2012. doi:10.1146/annurev-fluid-120710-101036.

S. E. Belcher, N. Jerram, and J. C. R. Hunt. Adjustment of a turbulent boundary layer to a canopy of roughness elements. *Journal of Fluid Mechanics*, 488:369–398, 2003. doi:10.1017/S0022112003005019.

S. E. Belcher, J. J. Finnigan, and I. N. Harman. Flows through forest canopies in complex terrain. *Ecological Applications*, 18:1436–1453, 2008. doi:10.1890/06-1894.1.

G. Bohrer, G. G. Katul, R. L. Walko, and R. Avissar. Exploring the effects of microscale structural heterogeneity of forest canopies using large-eddy simulations. *Boundary-Layer Meteorology*, 132: 351–382, 2009. doi:10.1007/s10546-009-9404-4.

M. Cassiani, G. G. Katul, and J. D. Albertson. The effects of canopy leaf area index on airflow across forest edges: Large-eddy simulation and analytical results. *Boundary-Layer Meteorology*, 126:433–460, 2008. doi:10.1007/s10546-007-9242-1.

B. Chen, M. Chamecki, and G. G. Katul. Effects of topography on in-canopy transport of gases emitted within dense forests. *Quarterly Journal of the Royal Meteorological Society*, 145(722): 2101–2114, 2019. doi:10.1002/qj.3546.

A. Connolly, F. K. Chow, and S. W. Hoch. Nested large-eddy simulations of the displacement of cold air pool by lee vortices. *Boundary-Layer Meteorology (In press)*, 2020.

J. W. Deardorff. Stratocumulus-capped mixed layers derived from a three-dimensional model. *Boundary-Layer Meteorology*, 18:495–527, 1980. doi:10.1007/BF00119502.

S. Dupont and Y. Brunet. Influence of foliar density profile on canopy flow: A large-eddy simulation study. *Agricultural and Forest Meteorology*, 148(6):976–990, 2008a. doi:10.1016/j.agrformet.2008.01.014.

S. Dupont and Y. Brunet. Edge flow and canopy structure: A large-eddy simulation study. *Boundary Layer Meteorology*, 126:51–71, 2008b. doi:10.1007/s10546-007-9216-3.

S. Dupont and Y. Brunet. Coherent structure in canopy edge flow: a large-eddy simulation study. *Journal of Fluid Mechanics*, 630:93–128, 2009. doi:10.1017/S0022112009006739.

S. Dupont, J. M. Bonnefond, M. R. Irvine, E. Lamaud, and Y. Brunet. Long-distance edge effects in a pine forest with a deep and sparse trunk space: In situ and numerical experiments. *Agricultural and Forest Meteorology*, 151(3):328–344, 2011. doi:10.1016/j.agrformet.2010.11.007.

H. Fernando. Fluid dynamics of urban atmospheres in complex terrain. *Annual Review of Fluid Mechanics*, 42(1):365–389, 2010. doi:10.1146/annurev-fluid-121108-145459.

J. Finnigan. Turbulence in plant canopies. *Annual Reviews of Fluid Mechanics*, 32:519–571, 2000. doi:10.1146/annurev.fluid.32.1.519.

J. Finnigan and S. Belcher. Flow over a hill covered with a plant canopy. *Quarterly Journal of the Royal Meteorological Society*, 130(596):1–29, 2004. doi:10.1256/qj.02.177.

J. Finnigan and Y. Brunet. *Wind and Trees: Turbulent airflow in forests on flat and hilly terrain*. Cambridge University Press, Cambridge, UK, 1995.

J. Finnigan, K. Ayotte, I. Harman, G. Katul, H. Oldroyd, E. Patton, D. Poggi, A. Ross, and P. Taylor. Boundary-layer flow over complex topography. *Boundary-Layer Meteorology*, 177:247–313, 2020. doi:10.1007/s10546-020-00564-3.

J. J. Finnigan. *Turbulent Transport in Flexible Plant Canopies. In: B. A. Hutchison, B. B. Hicks (eds) The Forest-Atmosphere Interaction*. Springer, Dordrecht, 1985. doi:10.1007/978-94-009-5305-5_28.

J. J. Finnigan, R. H. Shaw, and E. G. Patton. Turbulence structure above a vegetation canopy. *Journal of Fluid Mechanics*, 637:387–424, 2009. doi:10.1017/S0022112009990589.

E. Grant, A. Ross, and B. Gardiner. Modelling canopy flows over complex terrain. *Boundary-Layer Meteorology*, 161(3):417–437, 2016. doi:10.1007/s10546-016-0176-3.

I. N. Harman and J. J. Finnigan. A simple unified theory for flow in the canopy and roughness sublayer. *Boundary Layer Meteorology*, 123(2):339–363, 2007. doi:10.1007/s10546-006-9145-6.

J. Kaimal and J. Finnigan. *Atmospheric boundary layer flows. Their structure and measurements.* Oxford University Press, New York, USA, 1994.

J. B. Klemp, J. Dudhia, and A. D. Hassiotis. An upper gravity-wave absorbing layer for nwp applications. *Monthly Weather Review*, 136(10):3987–4004, 2008. doi:10.1175/2008MWR2596.1.

Y. Ma and H. Liu. An advanced multiple-layer canopy model in the wrf model with large-eddy simulations to simulate canopy flows and scalar transport under different stability conditions. *Journal of Advances in Modeling Earth Systems*, 11(7):2330–2351, 2019. doi:10.1029/2018MS001347.

H. G. Ouwersloot, A. F. Moene, and J. J. Attema. Large-eddy simulation comparison of neutral flow over a canopy: sensitivities to physical and numerical conditions, and similarity to other representations. *Boundary-Layer Meteorology*, 162:71–89, 2017. doi:10.1007/s10546-016-0182-5.

E. G. Patton and G. G. Katul. Turbulent pressure and velocity perturbations induced by gentle hills covered with sparse and dense canopies. *Boundary-Layer Meteorology*, 133:189–217, 2009. doi:10.1007/s10546-009-9427-x.

E. G. Patton, K. J. Davis, M. C. Barth, and P. P. Sullivan. Decaying scalars emitted by a forest canopy: A numerical study. *Boundary-Layer Meteorology*, 100:91–129, 2001. doi:10.1023/A:1019223515444.

E. G. Patton, P. P. Sullivan, and K. J. Davis. The influence of a forest canopy on top-down and bottom-up diffusion in the planetary boundary layer. *Quarterly Journal of the Royal Meteorological Society*, 129(590):1415–1434, 2003. doi:10.1256/qj.01.175.

M. R. Raupach and R. H. Shaw. Averaging procedures for flow within vegetation canopies. *Boundary-Layer Meteorology*, 22:79–90, 1982. doi:10.1007/BF00128057.

M. R. Raupach and A. S. Thom. Turbulence in and above plant canopies. *Annual Review of Fluid Mechanics*, 13(1):97–129, 1981. doi:10.1146/annurev.fl.13.010181.000525.

M. R. Raupach, P. A. Coppin, and B. J. Legg. Experiments on scalar dispersion within a model plant canopy part i: The turbulence structure. *Boundary-Layer Meteorology*, 35:21–52, 1986. doi:10.1007/BF00117300.

A. Ross and T. Baker. Flow over partially forested ridges. *Boundary-Layer Meteorology*, 146: 375–392, 2013. doi:10.1007/s10546-012-9766-x.

A. Ross and S. Vosper. Neutral turbulent flow over forested hills. *Quarterly Journal of the Royal Meteorological Society*, 131(609):1841–1862, 2005. doi:10.1256/qj.04.129.

A. N. Ross. Large-eddy simulations of flow over forested ridges. *Boundary-Layer Meteorology*, 128: 59–76, 2008. doi:10.1007/s10546-008-9278-x.

A. N. Ross. Scalar transport over forested hills. *Boundary-Layer Meteorology*, 141:179–199, 2011. doi:10.1007/s10546-011-9628-y.

A. N. Ross. Boundary-layer flow within and above a forest canopy of variable density. *Quarterly Journal of the Royal Meteorological Society*, 138(666):1259–1272, 2012. doi:10.1002/qj.989.

A. N. Ross and I. N. Harman. The impact of source distribution on scalar transport over forested hills. *Boundary-Layer Meteorology*, 156:211–230, 2015. doi:10.1007/s10546-015-0029-5.

R. H. Shaw and U. Schumann. Large-eddy simulation of turbulent flow above and within a forest. *Boundary-Layer Meteorology*, 61:47–64, 1992. doi:10.1007/BF02033994.

T. Tamura, A. Okuno, and Y. Sugio. Les analysis of turbulent boundary layer over 3d steep hill covered with vegetation. *Journal of Wind Engineering and Industrial Aerodynamics*, 95(9):1463–1475, 2007. doi:10.1016/j.jweia.2007.02.014.

P. A. Taylor. *Turbulent wakes in the atmospheric boundary layer. In: W. L. Steffen, O. T. Denmead (eds) Flow and Transport in the Natural Environment: Advances and Applications*. Springer-Verlag, Berlin, Germany, 1988. ISBN 978-3-642-73845-6.

J. Wilson, J. Finnigan, and M. Raupach. A first-order closure for diturbed plant-canopy flows, and its application to winds in a canopy on a ridge. *Quarterly Journal of the Royal Meteorological Society*, 124(547):705–732, 1998. doi:10.1002/qj.49712454704.

N. Wilson and R. Shaw. A higher order closure model for canopy flow. *Journal of Applied Meteorology and Climatology*, 16(11):1197–1205, 1977. doi:10.1175/1520-0450(1977)016<1197:AHOCMF>2.0.CO;2.

SECTION 4

Sensitivity of simulated flow recirculation zones to the representation of the forest canopy over the double-ridge of Serra do Perdigão

4.1 Motivation

The study described in Sect. 3 confirmed that the implemented canopy model was able to reproduce the main features of the mean flow over an idealised forested ridge. The results were found to have the same deficiency in vertical velocity variance over flat forested terrain and over-prediction of the TKE in the wake downstream of the top of the ridge, as were seen by Dupont et al. (2008). However, in general the model was able to provide significantly better results than representing the canopy with an increased roughness length at the surface. Little work has been done to determine whether these benefits over the surface roughness method would still apply when simulating more complex, forested terrain. For this reason it was decided to apply the WRF implementation of the canopy model to a more complex, real-world scenario. The Perdigão experiment (described in more detail below) was carried out in 2017 to study the flow over valley system formed by two parallel ridges in the Serra do Perdigão, Portugal. The terrain here is semi-idealised and the measurements collected were extensive. A large number of tower based instruments and several lidars provided a large, publicly available dataset. High-resolution aerial measurements of the canopy properties across the site were also collected and show a large fraction of the surface is forested. The study below uses a roughly 3 hour long period during the night time where the wind was blowing perpendicular to the ridges, in order to further equate the measurements and results of numerical simulations to the idealised cases that have previously been studied involving flow over forested hills/ridges. The horizontal resolution of the innermost domain and the overall extent of the outermost domain were configured in line with the recommendations of Liu et al. (2016). The canopy across this site was on average $10\,\mathrm{m}$ tall and so this was used as the horizontal resolution for the innermost domain. The outermost domain covered a $36 \times 36\,\mathrm{km}$ area to ensure the inclusion of the mountains to the north-west that were suggested during the field campaign to effect the flow around the valley. The finest resolution

that did not lead to numerical instabilities was used in the vertical dimension near the surface and was approximately $6\,\mathrm{m}$. Following suggestions from Grant et al. (2016) and Wagner et al. (2019), simulations were run in an LES mode and comparisons are made between high-resolution input data for the canopy properties and canopy properties that were assigned manually depending on land use category. The following was submitted to the peer-reviewed journal Boundary-Layer Meteorology on 26 May 2021 by the authors John Tolladay, Charles Chemel and Robert Menke.

4.2 Abstract

The dynamics of atmospheric boundary layer flows in complex terrain have been shown to be modified by the presence of tall canopies such as those of a forest. Numerical simulations that represent the canopy with a vertical extent and a specified density provide a more accurate reproduction of flows in idealised cases. Less work has been done to determine whether such methods of modelling the canopy can provide benefits in less idealised situations. The Perdigão experiment, carried out in Portugal in 2017, provides lidar and flux-tower data for flows over a semi-idealised double-ridge valley system. Different methods of representing the extensive canopy that covers this site are used in numerical simulations for a specific period of this case study, where the wind direction remains perpendicular to the ridges. Three different methods are used, namely the default approach of land use category assigned roughness-lengths at the surface, the use of a canopy model with arbitrary heights and densities applied based on land use category and an accurate representation of the canopy from high-resolution aerial surface scans. The large-scale flow over the double-ridge system was similar in each case and was not found to be strongly modified by the choice of method for representing the canopy. However, for simulations using only an increased roughness length to represent the canopy, recirculation was rarely seen to occur. It is found that simulations using a canopy model provide more accurate reproduction of the near-surface flow and recirculating flow within the valley. The results were found to be equivalent whether the canopy properties were set by land use category or using the high resolution data, but more variable canopies were found to reduce the level of turbulence occurring above.

4.3 Introduction

The predictability of near-surface wind and turbulence is key to a range of applications, including air pollution, aviation meteorology, and wind energy harvesting. Forested complex terrain poses particular challenges in this respect since the variability of the underlying surface strongly affects the flow in the atmospheric boundary layer (Finnigan et al., 2020). The uneven (rough and hilly) surfaces interact primarily with the atmospheric boundary layer through the pressure field, thereby exerting drag on the flow (e.g., Kaimal and Finnigan, 1994). The variations of pressure distort the mean flow and generate turbulence. The effects such of pressure perturbations induced by the rough orography include velocity speed-up, separation, attachment and recirculation.

The presence of recirculation zones downstream of orographic features can change the flow significantly and hence can profoundly affect the ventilation potential. The extent of the recirculation zones depends to a large extent on steepness of the terrain and canopy density. Recirculation zones are ubiquitous for flows over steep hills. For gentle hills, the theoretical work of Finnigan and Belcher (2004) predicts there is a critical canopy density that induces recirculation downstream of an idealised hill covered with a plant canopy. Results from flume experiments (Poggi and Katul, 2007) and high-resolution numerical simulations (Patton and Katul, 2009) are consistent with this prediction. For a relatively small canopy density, the flow does not reverse on the lee side of the hill while for a dense canopy a recirculation zone is created. Ross and Baker (2013) investigated the effects of partially forested idealised hills. Flow separation and resulting recirculation were found confined to the forested region over the lee slope where an adverse pressure gradient is induced by the terrain. As expected, the deeper canopies/lower hills were found to result in a larger pressure drag for partially forested hills, relative to the drag over a fully forested hill.

Real flows over forested complex terrain are generally over truly complex terrain with heterogeneous forest cover. Several field campaigns have studied orographic features of relatively moderate complexity, more amenable to analytical analysis, namely a single hill (e.g., Askervein in Scotland; Taylor and Teunissen, 1987) or an isolated escarpment (Bolund in Denmark; Berg et al., 2011). However, only a few studies have considered real forested complex terrain. Liu et al. (2016) simulated the flow over forested complex terrain around Taikoyama hill, Japan, where mast measurements were available at hilltop. The authors showed that a relatively large numerical domain had to be considered for observed wind and turbulence intensity to be simulated realistically. Grant et al. (2015) reported measurements made during the Arran canopy experiment over a partially forested hill on the north-east coast of the isle of Arran, UK. The data collected during this experimental campaign were modelled by Grant et al. (2016). Satisfactory model performance was obtained if the horizontal variability in canopy structure was explicitly represented. The sensitivity of the model results to the surface parameterisation was investigated with a focus on the separation region. This sensitivity study showed that using a roughness length parameterisation led to significant discrepancies between simulated and observed separation. The authors stressed the need to explicitly model the forest canopy if detailed predictions of near-surface flow around forests are required.

The recent Perdigão experiment (Fernando et al., 2019) provided extensive measurements over a mostly forested double-ridge straddling the Cobrão valley (Vale Cobrão) in Portugal. The scale of the orographic features is comparable to that of Askervein, but with land cover consisting mostly of trees of mean height ~ 10 m. Menke et al. (2019) used data from a network of scanning Doppler lidars to quantify occurrences of flow recirculation during the Perdigão experimental campaign. Flow recirculation was found to occur over 50% of the time when the wind direction is perpendicular to the direction of the ridges and to occur most frequently during periods with wind speeds ~ 6 m s^{-1}. Palma et al. (2019) presented results from a numerical model simulation of a case study for 14 to 15 May 2017, where flow separation occurred downstream of the ridge. The results were found to

be in good agreement with measurements. However, no detail was provided as to how the forested canopy was represented in the modelling system. Numerical simulations using a canopy model were carried out by Wagner et al. (2019) for a 49-day period at the Perdigão site. The use of a canopy model that gives the canopy a vertical extent was found to be necessary to reproduce the observed flow accurately. Some discrepancies were found with the observations and it was suggested that a more detailed description of the canopy may be required to improve the results.

The present work aims to investigate the sensitivity of simulated flow recirculation to the representation of the forest canopy at the site of the Perdigão case study during the night between 28 and 29 May 2017, when the wind was perpendicular to the direction of the ridges. A brief description of the site and the approach used for modelling the forest canopy are presented in Sect. 4.4. The methodology is given in Sect. 4.5 and the results are analysed in Sect. 4.6. Conclusions and some discussion are given in Sect. 4.7.

4.4 Setting and data collection

In the early summer of 2017, researchers from North America and Europe collaborated on a field campaign in Vale Cobrão, Portugal (Fernando et al., 2019). The campaign has taken on the name of a small village located close to the valley, Perdigão (partridge in Portuguese), and this is how it will be referred to hereafter. Two parallel ridges separated by 1.5 km and rising up to 300 m above the surrounding terrain form a valley system for which the cross-sectional profile remains similar over a north-west to south-east direction for approximately 4 km. Maps showing the site of the measurement campaign are provided in Fig. 17 and show an area 4x4 km in size. This was the area chosen to be covered by the innermost domain of the simulations described in Sect. 4.5.2. The satellite map in Fig. 17(a) shows a significant fraction of green space, with trees across much of the terrain. The mean flow in this location tends to be across the valley in a direction almost perpendicular to the ridges or aligned parallel to the ridges. This semi-idealised terrain and the tendency for flow across the ridges provide a relatively simple system in comparison to more complex real-world scenarios, making this campaign ideal for investigation of the sensitivity of simulated recirculation zones to the representation of the forest canopy.

Data was intensively collected at this site over a period of a month and a half, from 1 May 2017 to 15 June 2017. The measurements covered an area of 4×4 km and extended up to 10 km altitude with resolutions of tens of metres and seconds. The field campaign was carried out as part of the New European Wind Atlas (NEWA) project and all data collected is publicly available. An extensive array of instruments were used to collect measurements over the duration of the campaign including various lidar, radar and sodar systems, radiosondes, tethered launch systems and 49 meteorological towers with various instruments at several different vertical levels. These intensive measurements over a large area and the easy availability of the data make this a great data set to use as a comparison for the testing of numerical systems. While the lidar observations can provide wind speeds up to

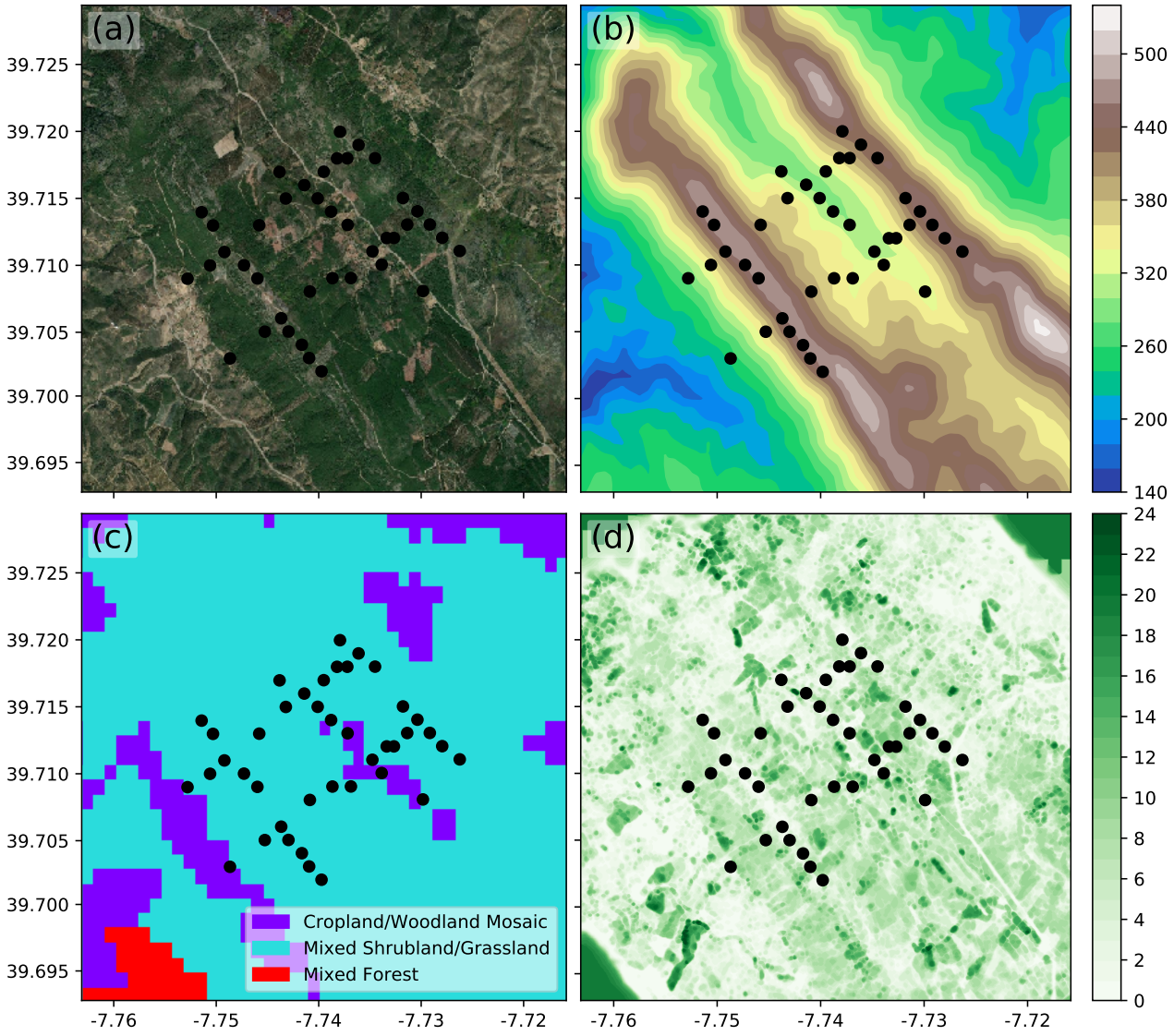

Figure 17: Co-located maps showing (a) a satellite image of the site, (b) the terrain height above sea level [m], (c) the United States Geological Survey land use categories as converted from the Coordination of Information on the Environment land use dataset and (d) the canopy height h_c [m] as measured by Palma and Batista (2019b). The black circles mark locations of flux towers at the site. Satellite image sources: Esri, DigitalGlobe, GeoEye, Earthstar Geographics, CNES/Airbus DS, USDA, USGS, AeroGRID, IGN, and the GIS User Community

many times the canopy height, the flux towers provide measurements from within and just above the canopy. Data from UCAR/NCAR-Earth Observing Laboratory (2019) for a selection of the flux towers at the site (see Sect. 4.6.1 for more detail) averaged at 5-minute intervals are used in the following sections. Observations from the six scanning lidars shown in Fig. 18(b) are presented in Sect.4.5.3. The lidar systems performed cross-sectional scans of the radial wind velocities normal to the valley axis across the northern and southern transect. The individual scans took 24 s and range gates were placed every 15 m at distances of 100 to 3000 m from the lidars. The measurements were filtered using an advanced filtering method as described in Menke et al. (2020). The raw data from Menke et al. (2018) was combined for the lidars at each transect using the methods explained in Menke et al. (2019). Here we show 30-minute averages of the data at the southern transect and averages of 10-minute periods along the northern transect.

4.5 Methodology

4.5.1 Modelling of the forest canopy

Forest canopies are often modelled in numerical simulations using an increased roughness length at the surface. Such methods have been shown to be effective in modelling the flow over rough ground, waves on open water (Cheng et al., 2014) and shallow canopies such as crops and grasslands (Tan and Ling, 1960; Tani, 1963; Uchijima and Wright, 1963). However, studies have shown that this parameterisation is unable to properly model the flow over deeper canopies such as woodland (Ross and Vosper, 2005; Dupont et al., 2008; Belcher et al., 2012). Using an analytical model, Finnigan and Belcher (2004) found that roughness lengths are unlikely to be suitable in accelerating or decelerating turbulent boundary layers, such as those around vegetative canopies. Shaw and Schumann (1992) developed a simple parameterisation that gives a vertical extent to the canopy and modifies the momentum and turbulence within the canopy for all grid cells where it is present. Such a model has been applied to idealised simulations for flat forested terrain (Shaw and Schumann, 1992; Shaw and Patton, 2003; Watanabe, 2004; Clark and Mitchell, 2007; Dupont and Brunet, 2008a,b, 2009; Patton and Katul, 2009; Froelich et al., 2011; Ross, 2012; Ouwersloot et al., 2017), forested hills and ridges (Kobayashi et al., 1994; Wilson et al., 1998; Brown et al., 2001; Ross and Vosper, 2005; Ayotte, 2008; Dupont et al., 2008; Ross, 2008, 2011; Ross and Baker, 2013; Xu et al., 2015; Tolladay and Chemel, 2021) and some modelling of real world scenarios (Liu et al., 2016; Grant et al., 2016).

Following Shaw and Schumann (1992) and Wilson et al. (1998) a model designed to account for the reduction in momentum, and the dissipation of turbulence caused by a tall vegetative canopy was implemented by the authors in the Weather Research and Forecasting (WRF) modelling system, version 4.1.1 (Skamarock et al., 2019). The reduction of the momentum of the flow, caused by interaction with canopy elements, is modelled using a sink term in the momentum equation as

$$\mathbf{F}_c = -C_d\, a\, |\mathbf{u}|\, \mathbf{u}, \tag{29}$$

where the drag coefficient $C_d = 0.25$ (see Ross and Baker, 2013; Finnigan and Belcher, 2004), a is a position dependent one-sided plant area density and $|\mathbf{u}|\ \mathbf{u}$ is the square of the resolved velocity $\mathbf{u}$. WRF was configured to run in a large-eddy-simulation (LES) mode. The 1.5-order turbulence closure scheme developed by Deardorff (1980) with a prognostic equation for k_{SGS}, was used to determine the sub-grid-scale (SGS) fluxes from the resolved fields and the SGS turbulence kinetic energy (TKE). In this scheme, the eddy viscosity of momentum K_m is modelled as

$$K_m = C_k\, \lambda\, \sqrt{k_{\mathrm{SGS}}}, \tag{30}$$

where the diffusion coefficient $C_k = 0.10$ and the SGS mixing length scale λ is defined algebraically. Where grid cells are within or in close proximity to the canopy, the scale of the most energetic unresolved eddies are dependent on the shear layer at canopy top

$$\lambda_s = \frac{|\mathbf{u}|\,(h_c)}{(\partial|\mathbf{u}|/\partial z)_{h_c}}, \tag{31}$$

where h_c is the height of the canopy. Wilson et al. (1998) uses λ_s in combination with the distance to the ground to determine an 'inner' length scale λ_i and with the distance above the displacement height of the canopy to determine an 'outer' length scale, namely

$$\frac{1}{\lambda_i} = \frac{1}{\kappa\, h} + \frac{1}{\lambda_s} \quad \text{and} \quad \frac{1}{\lambda_o} = \frac{1}{\kappa\ (z-d)}, \tag{32}$$

where h is height above the ground, $d = 0.7h_c$ is the displacement height of the canopy and κ is the von Kármán constant. The maximum of these is then taken as the canopy length scale $\lambda_c = \max(\lambda_i, \lambda_o)$. The most energetic unresolved turbulence away from the canopy is assumed to consist of the largest SGS eddies, of the same scale as the grid cell they are contained within. This is calculated as the cube root of the volume of the grid cell being processed $\Delta s = (\Delta \mathrm{x}\, \Delta \mathrm{y}\, \Delta \mathrm{z})^{1/3}$ and the length scale $\lambda = \max(\lambda_c, \Delta s)$. As proposed by Deardorff (1980), the SGS TKE dissipation in free space is modelled as

$$\epsilon_v = C_\epsilon\, k_{\mathrm{SGS}}^{3/2}/\lambda, \tag{33}$$

where the dissipation coefficient $C_\epsilon = 0.93$, except in the first grid cell immediately above the surface, where C_ϵ is increased to 3.9 to mimic a 'wall effect' so as to prevent k_{SGS} from becoming unduly large there. Following Shaw and Schumann (1992), the standard viscous dissipation ϵ_v was augmented by an additional dissipation term, ϵ_c, to represent the dissipation caused by the interactions between the air and the canopy, viz.

$$\epsilon_c = 2\, C_d\, a\, |\mathbf{u}|\ k_{\mathrm{SGS}}. \tag{34}$$

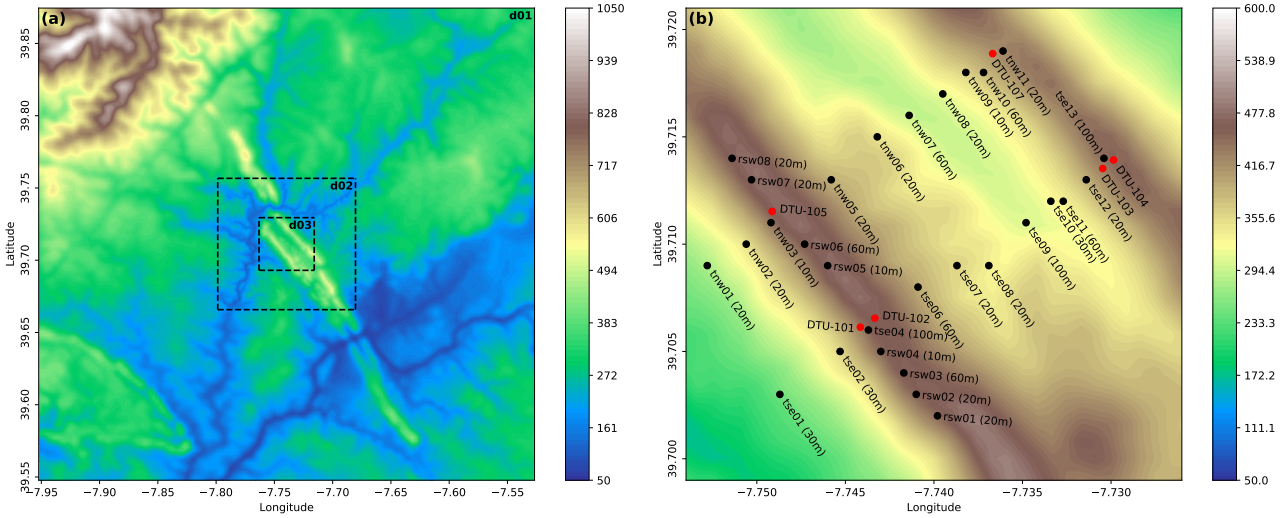

Figure 18: Map of (a) the terrain surrounding the site of observations and showing the extent of the three domains used in all simulations carried out for this work and (b) a zoomed in map of the terrain around the flux towers used for comparison with model data, labelled with their name and height in brackets. The shading shows the height above sea level [m] and the position of the lidars used in Sect.4.6 are also marked with red circles

4.5.2 Model configuration

Simulations were carried out with three nested domains, as shown in Fig. 18(a), using one-way nesting. The dimensions and spatial and temporal resolution of the three domains are described in Table 2. Each domain uses terrain-following co-ordinates in the vertical dimension with 81 levels extending up to approximately 12 km altitude. The vertical grid is compacted close to the ground using a hyperbolic tangent function that provides a spacing between the ground and the first level of just over 5 m depending on the height of the terrain. A higher resolution in the vertical at ground level would be preferable to provide more levels within the shortest canopies but reducing the height of the lowest grid cell requires ever smaller time steps to avoid numerical instability. This leads to longer simulation times that can become impractical and in some cases the time step could not be reduced sufficiently to avoid these issues.

A 3 km Rayleigh damping layer is implemented at the frictionless lid at the top of the domain to dampen vertically propagating internal gravity waves. The lateral boundaries of the outermost domain are set every 6 hours by meteorological input data provided by the National Centers for Environmental Protection (National Centers for Environmental Prediction, National Weather Service, NOAA, U.S. Department of Commerce, 2000) and the Unified Noah Land Surface Model (Tewari et al., 2004) and Eta similarity scheme (Monin and Obukhov, 1954) are used at the lower boundary. The planetary boundary layer (PBL) is resolved explicitly, as opposed to being parameterised with a PBL scheme. The 1.5 order TKE closure of Deardorff (1980) is used with diffusion and mixing handled in stress form. The Thompson micro-physics scheme (Thompson et al., 2008) and Rapid Radiative Transfer Model for Global (RRTMG) (Iacono et al., 2008) are used in all domains.

Table 2: Details about the various domains used in the simulations carried out for this work

Domain	Latitudes	Longitudes	Horizontal span	Grid size (x, y, z)	dx and dy	dt
d01	$39.55 - 39.87$	-7.95 – -7.53	36 km	(144, 144, 80)	250 m	$1/8$ s
d02	$39.67 - 39.76$	-7.80 – -7.68	10 km	(200, 200, 80)	50 m	$1/40$ s
d03	$39.69 - 39.73$	-7.76 – -7.72	4 km	(400, 400, 80)	10 m	$1/40$ s

Simulations are started at 1800 UTC on 28 May 2017 such that the model is able to adjust to the initial conditions before the start of the selected time period at 2317 UTC on 28 May 2017 (see Sect. 4.5.3 for further details). Data is exported from the model at 20 s intervals, providing nearly 500 time steps from which to calculate 34 5 min averages of wind speeds and fluxes for comparison with the measurements. The topography used in WRF simulations is interpolated by the WRF Pre-processing System (WPS) from various sources of terrain data with different resolutions. The highest resolution available as default in WPS is 30 arc-seconds, which equates to approximately 900 m between data points. While this may be suitable for the outer domain, it is a resolution about 90 times more coarse than the resolution of the inner domain. Topographical data from the 3 arc-second Shuttle Radar Topographic Mission (SRTM) carried out by the National Aeronautics and Space Administration (NASA) was therefore converted in to the binary format used as an input to WPS (Jarvis et al., 2008). This provides data at a resolution of approximately 90 m from which WPS can interpolate a terrain field to be used in WRF. Higher resolution data was made available from the aerial lidar scans of Palma and Batista, however this data was not used due to time constraints and requirements to keep the terrain consistent with simulations that had already been completed.

Three different simulations were carried out for comparison with the measurements and each characterises surface vegetation in a different way. As with the terrain, the default land use options available in WRF are not of a high enough resolution to provide detail within the innermost domain. The authors therefore followed the work of Pineda et al. (2004) to convert the 44 Coordination of Information on the Environment (CORINE) land use categories to the 24 categories used by USGS at a resolution of 100 m. A simulation that will be referred to as WRF-R uses the standard methods available in WRF to represent vegetation at the surface. USGS land use categories are assigned with their default surface roughness lengths z_0 as well as a range of other relevant quantities such as albedo and moisture availability. Values of z_0 for the categories "Cropland/Woodland Mosaic", "Mixed Shrubland/Grassland" and "Mixed Forest" found in the innermost domain are 0.2 m, 0.06 m and 0.5 m, respectively. The relationship between roughness length and canopy height is dependent on many factors (see for example Verhoef et al., 1997), but if the estimate of $h_c = 10z_0$ is used then these categories have effective canopy heights of 2 m, 0.6 m and 5 m for WRF-R. However, it should be noted that these z_0 values are selected to replicate areas that have a range of canopy types, densities and heights present.

The simulation referred to here as WRF-C uses the canopy model described in Sect. 4.5.1 and

also uses the USGS land use categories to assign canopy properties. Where land use categories involving woodland or shrubland are present, WRF-C uses a canopy height based on averages of the canopy data collected by Palma and Batista (2019b) and shown in Fig.17(d). For woodland land use, the height of the canopy is set as $h_c = 20\,\mathrm{m}$ and this value is halved to $h_c = 10\,\mathrm{m}$ for areas of shrubland. The momentum and turbulence modifications are then applied respectively over the bottom 4 or 2 grid levels. Whether shrubland or woodland is present, the canopy density $a = 0.35\,\mathrm{m}^{-1}$ and where woodland/shrubland is mixed with other land use types, such as grassland or cropland, the canopy density is halved to $a = 0.175\,\mathrm{m}^{-1}$. These values for canopy density were again set based on averages of the high-resolution canopy data provided by Palma and Batista (2019a). One further simulation is carried out that uses the high-resolution canopy data to assign accurate values of canopy height and density to each grid cell where the data was present and is assigned the reference WRF-T. For all locations where this data was not present, mostly outside of the innermost domain, canopy properties were assigned as for WRF-C using the land use categories. For all locations where h_c is greater than zero but less than the height of the first grid level, the canopy is effectively given the extent of the height of the first grid level at that location. Both WRF-C and WRF-T use a surface roughness of $0.01\,\mathrm{m}$ for locations where a canopy is present. These two methods were used to assign canopy properties to the domain to determine whether high-resolution canopy data can provide significantly better reproduction of the flow than a more simple representation. High-resolution input data for the canopy properties is not generally available to modellers so it would be beneficial if the more simple description can still provide benefits over standard surface parameterisations.

4.5.3 Flow conditions

In order to have results that it is possible to relate to previous experiments, a period where the predominant flow was in a direction perpendicular to the valley axis is selected. Using the measurements from the highest instruments on the towers situated on the ridge-tops, the longest period of across-valley flow was determined. This selected time period (STP), over which data will be extracted from the flux measurements and from the simulations described below, extends from 2317 UTC on 28 May 2017 to 0202 UTC on 29 May 2017. During this period the conditions were thermodynamically stable and the wind direction measured at towers tse04 and tse13 (see Fig. 19(a)) at $100\,\mathrm{m}$ above ground level was within 10° of being perpendicular to the ridges and from the south-west (220 to 240°). The quantities u and v that are used in Sec. 4.6 refer to the across- and along-valley wind velocity, with positive values representing components of the wind from 230° and 140°, respectively.

A comparison between the measured and simulated wind speed and direction over the STP for a selection of the flux tower instruments are shown in Fig. 19. Wind speed and direction for the top instrument, at a height of $100\,\mathrm{m}$, on towers tse04 and tse13, used to determine the STP, are shown in Fig. 19(a)-(d). For tower tse04 on the upstream ridge (to the south-west), the simulated

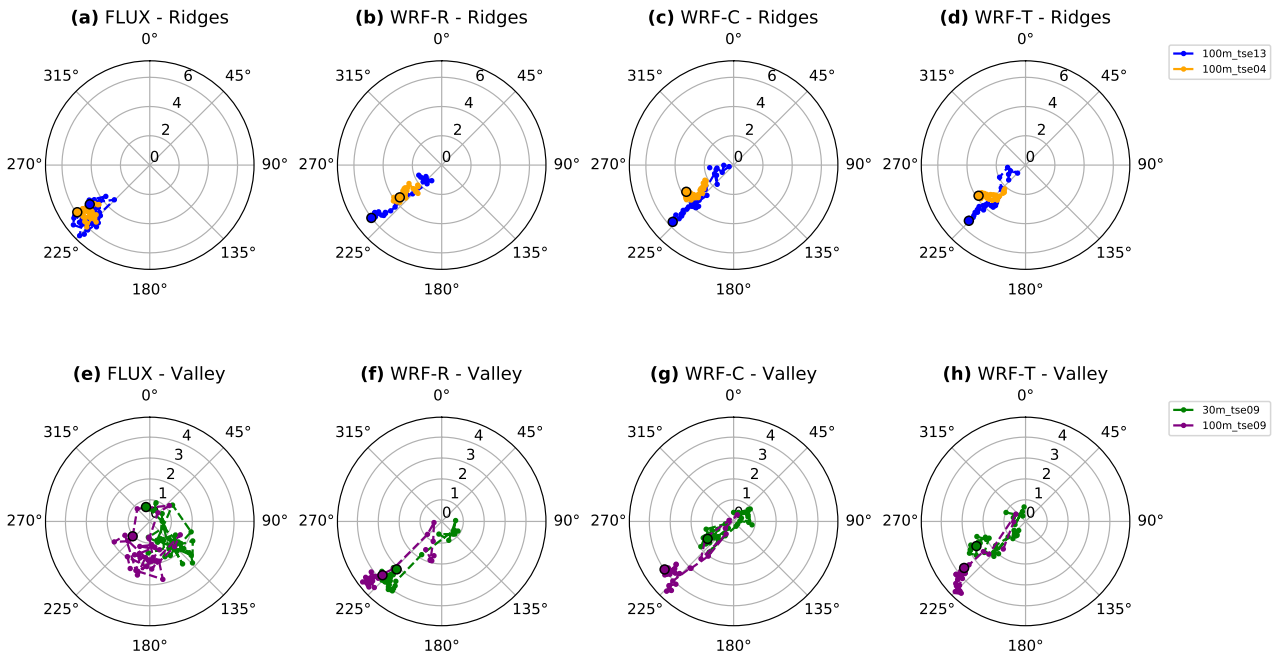

Figure 19: Polar plots showing 5-minute averaged wind speed [ms^{-1}] and direction time series' over the STP for instruments on the ridge-top towers tse04 and tse13 (top) and for valley floor tower tse09 (bottom). From the left to the right column, data is presented for the flux measurements, WRF-C, WRF-R and WRF-T, respectively. The first reading of the observation period for each measurement position is marked with a larger circle outlined in black, with subsequent time periods linked with a dashed line for each instrument

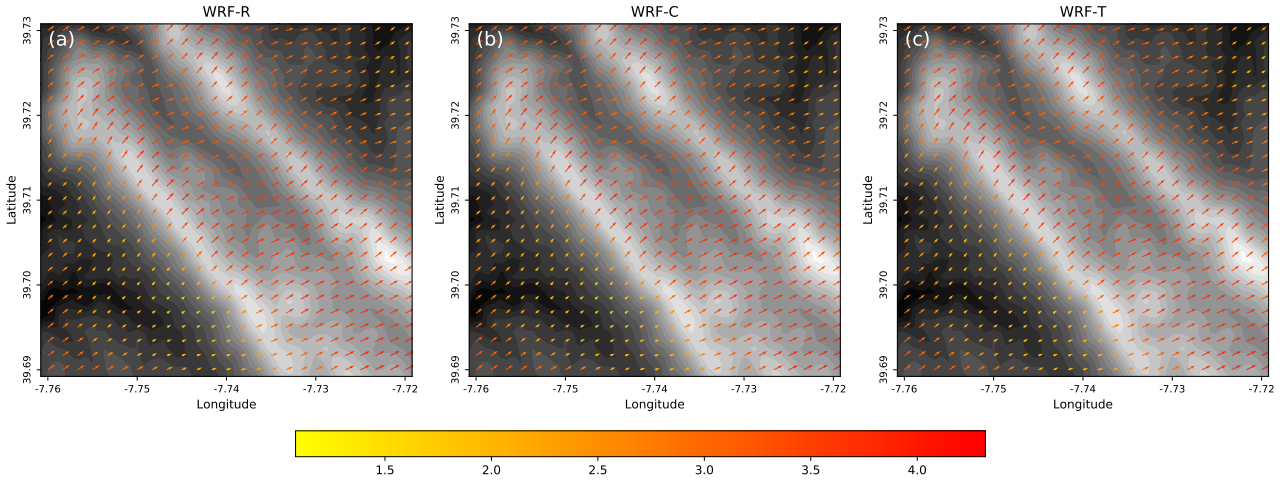

Figure 20: Time averaged wind speed [ms^{-1}] and direction for the selected time period at $z = 600$ m above sea level, approximately 100 m above ridge height, for (a) WRF-C, (b) WRF-R and (c) WRF-T. The topography is represented by the grey-scale shading to show the location of the ridges

wind speeds tend to be roughly 30% less than the speed seen in the flux measurements and are more variable. However, the three simulations provide a very similar distribution of the wind at these locations and the across valley direction is maintained for each case. The wind speed and direction within the valley is much more variable for the flux measurements but the variability in the along valley direction is not reproduced in the simulations (see Fig. 19(e)-(h)). The flow at $h = 100$ m for tower tse09 tend to remain similar to the mean across valley flow, but with significantly slower wind speeds towards the end of the STP. While there is little difference between the flow at $h = 30$ m and $h = 100$ m for WRF-R and WRF-T, the distribution of wind speeds at the lower instrument heights are reproduced more accurately by WRF-C.

For further inspection of the wind field at altitude, Fig. 20 shows the horizontal distribution of wind speed and direction at $z = 600$ m above sea level, approximately 100 m above the ridge height, or roughly equivalent to the top of the towers shown in the top row of Fig. 19. The three simulations show very similar distributions of wind speed and direction, indicating that the different methods of handling the vegetation at the surface does not have a large impact on the wind well above the ground. Some slight differences are present in the results of WRF-R, with slightly faster wind speeds upstream and downstream of the ridges that make up the valley system. This is likely to do with the fact that representing the surface vegetation with a roughness length provides less drag than is required for a tall canopy and results in faster wind speeds than those measured or simulated using a canopy model at most positions. For all cases, the flow tends to be diverted towards the east as it proceeds over the upstream ridge and is then diverted back towards the north-east as it moves past the downstream ridge (to the north-east).

Although the flow is fairly constant at elevations above the ridge-tops, it is more variable within the valley. Both transects show a similar flow towards the beginning of the STP, as presented in Fig. 21. The across-valley component of the wind u is estimated by the radial velocity of the two

lidars positioned at the ridge-tops of each transect marked in red in Fig. 18(b). The first scan taken during the STP is presented in Fig. 21(a) for the northern transect and Fig. 21(e) for the southern transect. As with the measurements taken by the flux towers, u is over-predicted by the simulations at all positions within the valley, shown beneath each of the lidar results in Fig. 21(b) to (d) and (f) to (h) respectively for the northern and southern transects.

The lidar measurements show a larger recirculation zone downwind of the upstream ridge at both transects than is seen in the simulations. The recirculation region extends 380 m downwind of the upstream ridge-top at the northern transect for both canopy model cases (WRF-C and WRF-T) and reaches elevations of approximately 50 m above the surface, not reaching higher than the ridge-top. The measured recirculation region at this location has a similar horizontal extent, bounded by the bulge in the lee slope and extending up to the height of the ridge-top. Reversed flows are measured over a larger vertical extent further downstream of the ridge than those simulated, occurring up to 100 m above ground level until 390 m downwind of the ridge-top. At the southern transect the reversed flows measured in the lee of the upstream ridge are weaker, but are present up to 800 m downstream, to the lowest point of the valley. The simulations show much less variation in the extent of the recirculation region between the two transects and WRF-R shows no recirculation occurring at the upstream ridge at either transect. Gentle reversed flows are also seen within the canopy on the windward slope of the upstream ridge at both transects for the two canopy model cases.

The lidar measurements do not provide data for the recirculation zone in the lee of the downstream ridge at the northern transect and only extend down to approximately 50 m above the surface at the southern transect. The zero contour in Fig. 21(e) can be seen to extend from the downstream ridge-top, indicating that at least some recirculation is occurring here close to the ground. The simulated recirculation is stronger at the downstream ridge, where the lee slope is steeper and descends to a point below the valley floor. Reversed flows are occurring up to the height of the ridge-top at the northern transect and in some cases are still present close to the surface more than 1 km downstream, until a point outside of the innermost domain. Recirculation over such a large extent was also present in the lidar data where available, an example from the southern transect is presented in Fig. 21(i). For WRF-C the recirculation in this region is limited to within 50 m of ground level with no reversed flows more than 600 m downwind of the ridge-top at the northern transect. At the southern transect the recirculation is much more similar to that seen for the other cases. No reversed flows are present at the southern transect for WRF-R and those at the northern transect are over a similar horizontal extent but lesser vertical extent than for WRF-T. Over the STP reversed flows were rarely present in the WRF-R results on the lee slope of the downstream ridge.

Insufficient data was available within the valley from the lidar scans that occurred later in the STP to make a comparison with the simulations. However, for each case simulated the flow developed in a similar way. Approximately one and a half hours in to the STP, the flow begins to become

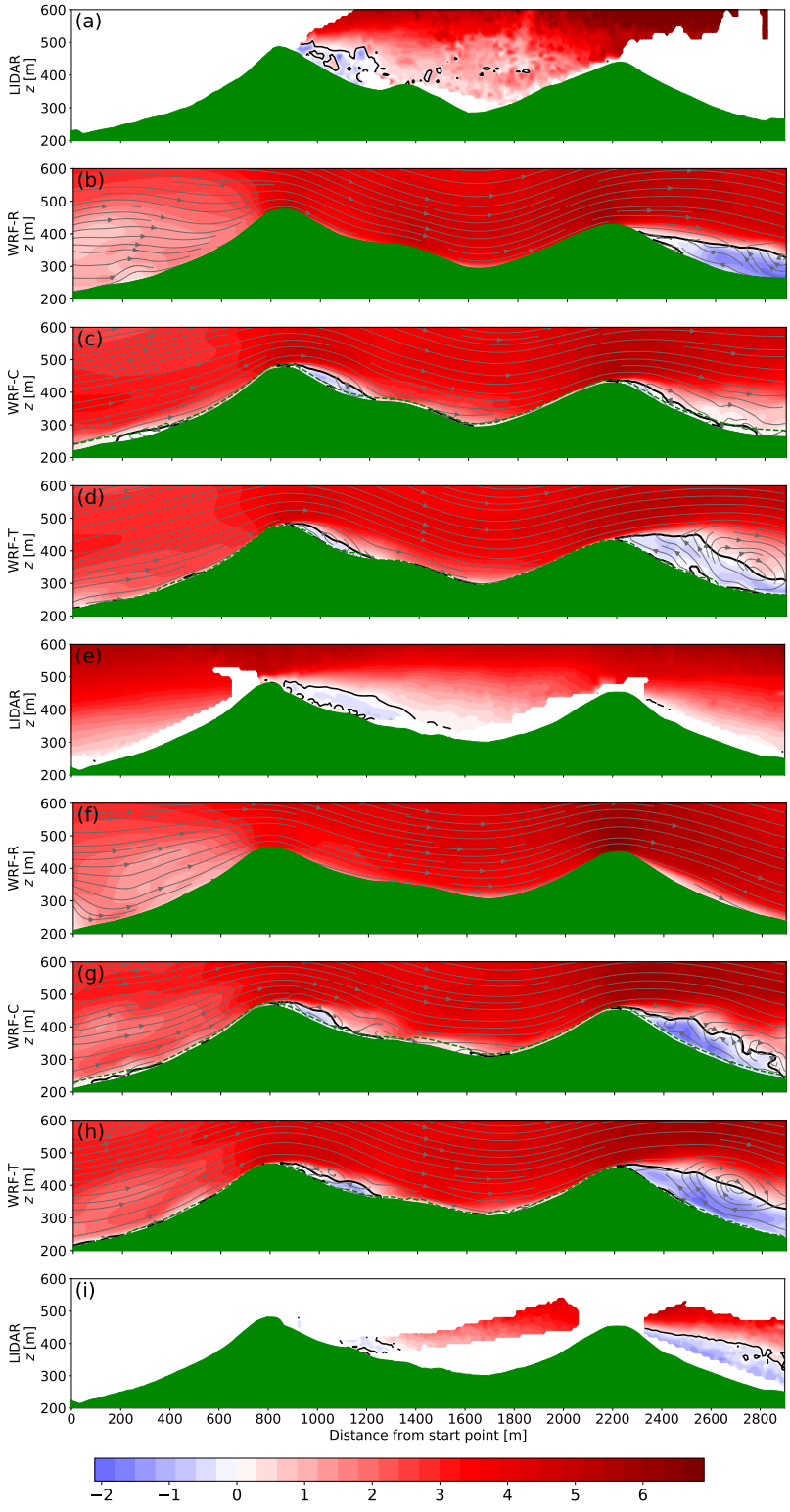

Figure 21: Cross-sections shaded with the across-valley flow u [ms^{-1}] with the zero contour marked with a thick black line for (a) lidar scans from the northern transect for 2300 to 2310 UTC on 28/05/2017, simulated results at the northern transect for (b) WRF-C, (c) WRF-R and (d) WRF-T, (e) lidar scans from the southern transect for 2300 to 2330 UTC on 28/05/2017, simulated results at the southern transect for (f) WRF-C, (g) WRF-R and (h) WRF-T and (i) lidar scans from the southern transect for 0100 to 0130 UTC 29/05/2017. Simulated results are shown for a 5 minute averaged period at the beginning of the STP with streamlines marked in grey and the canopy height marked by a dashed green line for the canopy model cases

attached to the valley floor and the extent of the recirculation zone is restricted in the lee of both ridges. While still extending up to $200\,\mathrm{m}$ downwind of the upstream ridge, the reversed flows are only occurring very close to the canopy, no higher than $h = 20\,\mathrm{m}$. At this point the recirculation also begins to reduce in the lee of the downstream ridge until no recirculation is occurring on this slope for any of the simulations. Over the final hour of the STP, as the recirculation in the lee of the downstream ridge reduces, strong turbulence begins to build up around the downstream ridge. This then leads to the flow becoming attached to the lee slope of the downstream ridge and the flow begins to recirculate within the valley above the lowest point. Very little recirculation is seen immediately downwind of the upstream ridge over this final hour at the southern transect, but reduced levels of recirculation continue to occur at the northern transect until the end of the STP. The recirculation region above the lowest point of the valley becomes much more extensive than those seen downstream of the ridges for all simulated cases, covering up to $600\,\mathrm{m}$ in the horizontal and reaching more than $200\,\mathrm{m}$ above the surface, in some cases above the height of the ridges. While there was some evidence of reversed flows occurring in this location in the lidar measurements towards the end of the STP, there was insufficient data available to infer the magnitude and extent of this region of recirculation.

4.6 Results and Analysis

4.6.1 Flux towers

Although there are measurements from a large number of flux towers and weather stations across the site, many were not used due to a lack of data during the STP or because they were unsuitable for the current study. The towers for which there was suitable data available are shown in Fig. 18(b) and labelled with the name assigned to them by the National Center for Atmospheric Research (NCAR) and the height of the highest instrument. A detailed view of the canopy distribution and slope around each tower can be seen in Fig. 22 and details about each tower are listed in Table 3. The measurements from these towers will be used to compare to values extracted from the results of simulations at the corresponding locations. Many of the towers on the upstream ridge have been excluded for simplicity but most show very similar results to those on the ridge-top of the northern and southern across-valley transects of towers, as can be seen in Fig. 23 discussed below.

The simulated wind speeds are approximately 1 to $2\,\mathrm{ms}^{-1}$ slower than those of the measurements at the top of the upstream ridge. This discrepancy is most significant in the case of WRF-R at the lowest instrument heights. With increasing height the difference between the measured and simulated wind speeds increases for all cases, with a discrepancy of 2 to $3\,\mathrm{ms}^{-1}$ at $h = 100\,\mathrm{m}$ (see Fig. 23(m) to (p)). For WRF-T, the most southerly of the ridge-top towers show the mean wind being directed to a more easterly direction that is not seen in the measurements or the other cases simulated. At the position of the two towers immediately downwind of the upstream ridge the two canopy simulations (WRF-C and WRF-T) are consistent with the measurements, showing very little

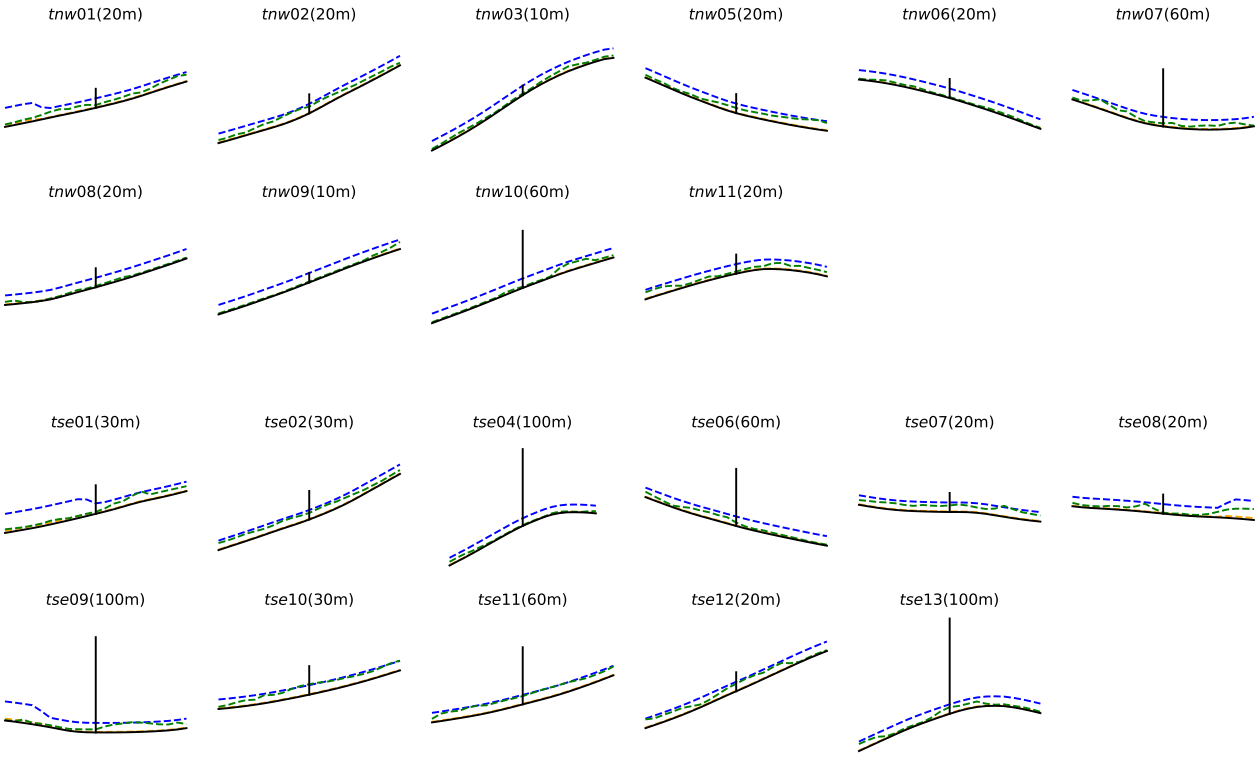

Figure 22: Cross-sections of the terrain and effective canopy heights from WRF-C (blue) and WRF-T (green) around the towers of the north (top) and south (bottom) transects of towers. Plots are presented with an equal aspect ratio to show actual terrain gradient and tower height (to highest instrument) and extend horizontally for 100 m either side of the towers

Table 3: Details about the flux towers selected for comparison with simulation data

			WRF-C		WRF-T		WRF-R
Tower	Altitude [m]	Height [m]	h_c [m]	a [m^{-1}]	h_c [m]	a [m^{-1}]	z_0 [m]
tse01	243.7	30	20.0	0.17	3.0	0.24	0.2
tse02	354.7	30	10.0	0.17	7.0	0.24	0.06
tse04	447.3	100	10.0	0.17	1.0	0.27	0.06
tse06	398.0	60	10.0	0.17	7.0	0.4	0.06
tse07	359.5	20	10.0	0.17	7.0	0.42	0.06
tse08	336.9	20	10.0	0.17	1.0	0.1	0.06
tse09	308.5	100	10.0	0.17	3.0	0.12	0.06
tse10	322.6	30	10.0	0.17	11.0	0.18	0.06
tse11	332.9	60	10.0	0.17	9.0	0.24	0.06
tse12	385.2	20	10.0	0.17	7.0	0.18	0.06
tse13	442.6	100	10.0	0.17	8.0	0.28	0.06
tnw01	279.7	20	10.0	0.17	4.0	0.63	0.06
tnw02	347.6	20	10.0	0.17	7.0	0.29	0.06
tnw03	434.3	10	10.0	0.17	1.0	0.28	0.06
tnw05	392.6	20	10.0	0.17	6.0	0.35	0.06
tnw06	350.7	20	10.0	0.17	1.0	0.51	0.06
tnw07	298.3	60	10.0	0.17	3.0	0.53	0.06
tnw08	312.1	20	10.0	0.17	1.0	0.23	0.06
tnw09	359.7	10	10.0	0.17	1.0	0.37	0.06
tnw10	378.0	60	10.0	0.17	2.0	0.45	0.06
tnw11	423.4	20	10.0	0.17	1.0	0.09	0.06

response in the time averaged wind speed below $h = 40\,\text{m}$. The reduction in the mean wind speeds at these locations are the result of turbulence and reversed flows generated by the ridge and any canopy present, as will be explored further in Sect. 4.6.4.

Measured time averaged wind speeds within the valley are greatly reduced in comparison to the flow at the upstream ridge-top and the direction no longer follows the mean south-westerly flow at $h = 20\,\text{m}$. The reduction of mean wind speed within the valley is much weaker for the simulations, with the wind direction tending to remain aligned to the mean flow. The two towers within the valley that are immediately downstream of the area where canopy height exceeds $20\,\text{m}$ (marked in green) for WRF-C show a significant reduction in wind speed and match more closely with the measurements than the other towers within the valley. For WRF-R, where this area has an increased surface roughness z_0, the wind speed is also reduced but to a much lesser extent. The same two towers show negligible wind speeds at $h = 20\,\text{m}$ for WRF-T but again do not match the rotation of the mean wind direction to the more south-easterly direction seen in the measurements. As height increases to $h = 100\,\text{m}$, the simulated wind speeds for the towers within the valley become more similar between the three simulations and all are over-predicted by 2 to 3ms^{-1}.

At the windward slope of the downstream ridge the mean wind speed is reproduced well in all of the simulations at $h = 20$ to $60\,\text{m}$. However, at the top of this ridge the simulated mean wind speed is approximately half that of the measurements, with WRF-T showing almost one third of the measured wind speed at $h = 20\,\text{m}$. No towers are present on the lee slope of this ridge to compare the simulated flow with measurements for the region downstream of the ridge and valley system.

4.6.2 Across-valley flow

For closer inspection of the flow at the northern and southern transects of flux towers, the mean across-valley component of the flow $\bar{u}$ and TKE per unit mass k averaged over the STP are shown for each instrument height of each tower in Fig. 24. In the region upwind and below the top of the upstream ridge, $\bar{u}$ is reduced as the flow interacts with the windward slope, as is seen more clearly in the cross-sections of each transect, presented in Fig. 25. For the northern transect, $\bar{u}$ remains negative up to $h = 60\,\text{m}$ and TKE remains below $k = 0.4\,\text{m}^2\text{s}^{-2}$. While the smoother slope down in to the valley at the southern transect leads to slightly greater $\bar{u}$ at and above $h = 60\,\text{m}$, the magnitude of TKE seen at tse09 is almost twice that seen for tnw07 at all measured levels. Immediately after the valley bottom, at the leading edge of the downstream ridge, $\bar{u}$ is reduced to almost zero at all heights measured. As the flow proceeds up this slope, $\bar{u}$ increases gradually until the top of the downstream ridge, where it reaches 3 to $4\,\text{ms}^{-1}$ at $h = 20\,\text{m}$ for both tnw11 and tse13. At the southern transect, the flow is accelerated at the peak of the upstream ridge and $u = 5 \pm 1\,\text{ms}^{-1}$ from $h = 10$ to $100\,\text{m}$. Up to this point k is negligible, remaining below $0.2\,\text{m}^2\text{s}^{-2}$ at all measured heights. The towers on the lee slope all measure reversed mean flows of up to $u = -1\,\text{ms}^{-1}$ and the magnitude of TKE increases from $k = 0.3$ to $0.5\,\text{m}^2\text{s}^{-2}$. At the lowest point

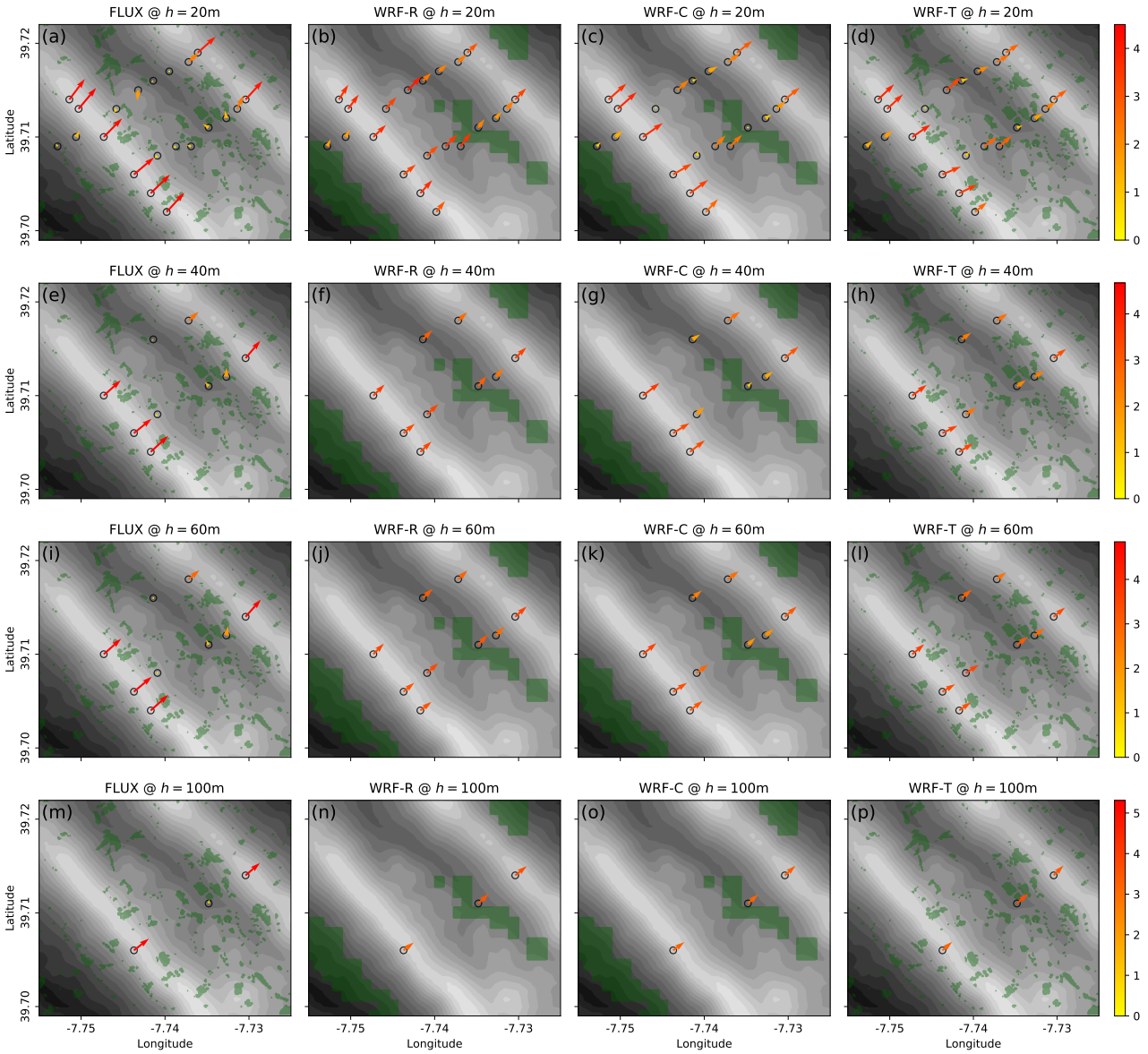

Figure 23: Mean wind speed [ms^{-1}] and direction over the selected time period measured by the flux towers (first column) and extracted from WRF-C, WRF-R and WRF-T respectively in the remaining columns. Each row shows data from a specific instrument height for towers where this instrument is present. The areas shaded in green represent locations where canopy height $h_c > 10\,\mathrm{m}$ or locations where surface roughness is increased for WRF-R

of the valley the measurements still show some reversal of the mean flow but wind velocity here remains at $u = \pm 1\,\mathrm{ms}^{-1}$.

The simulations each show different responses to the ridge and valley system. For WRF-R the across-valley mean wind velocity $\bar{u}$ is consistently over-predicted, by as much as $6\,\mathrm{ms}^{-1}$ at $h = 20\,\mathrm{m}$ for tnw06, with k being under-predicted and remaining close to $0\,\mathrm{m}^2\mathrm{s}^{-2}$. It is only when the flow reaches the upwind slope of the downstream ridge that $\bar{u}$ for WRF-R begins to become consistent with the measured wind speeds. Across-valley wind velocity at tnw10 is almost identical to that measured at all instrument heights and remains closer to the measurements at tnw11 than for the simulations using a canopy model. At the southern transect, WRF-R performs less well, with over-prediction on the windward slope and then under-prediction at the top of the downstream ridge of approximately $\pm 1\,\mathrm{ms}^{-1}$. The magnitude of TKE is seen to increase as the flow proceeds along this slope for WRF-R, but k is still under-predicted by 75% or more.

The results of WRF-C and WRF-T show a similar distribution of $\bar{u}$ and k across the valley system. Upwind of the upstream ridge the canopy model cases both match well with the measured $\bar{u}$ and the low levels of k seen in the measurements. At the top of the upstream ridge, $\bar{u}$ is under-predicted and a slight rise in k that is seen in the measurements is not seen for WRF-C or WRF-T. As the flow proceeds down the slope in to the valley, both cases show very low or negative $\bar{u}$ at low levels. The reversal of the mean flow is not as strong or occurring as high above the ground as is seen in the measurements. Results for WRF-C and WRF-T are more consistent with the measurements than are the results of WRF-R, especially within close proximity of the ground. Proceeding further downstream, the wind speed for the canopy model cases tends to remain between the measured values and the over-predicted values seen in WRF-R, while the TKE tends to be under-predicted less by the canopy model cases than by WRF-R. For the highest towers on the downstream ridge, the results of all of the simulations have become very similar, but not entirely consistent with the measurements. For example, at tower tnw10 $\bar{u}$ is reproduced very accurately by each simulation, but k is under-predicted by more than 80%, while at tower tse13 both $\bar{u}$ and k are under-predicted. The results for WRF-C and WRF-T generally reproduce the mean flow within the valley more accurately than WRF-R, but the resulting impact on the flow after crossing the two ridges is very similar regardless of the method used to represent the canopy.

The deficiency in k when the canopy model is not used can be seen clearly in Fig. 26(a) and (d), where the results for WRF-R show k reaching no more than 0.25 and $0.52\,\mathrm{m}^2\mathrm{s}^{-2}$ across the north and south transect of towers, respectively. The magnitude of k near the surface is on average 195% larger for WRF-C than for WRF-R across the northern transect and 115% larger at the southern transect. The distribution and magnitude of k is much more similar for the two canopy model cases, especially for the northern transect of towers. The magnitude of k near the surface is on average 39% larger for WRF-C than for WRF-T across the northern transect. However, near the surface of the southern transect k is on average 10% larger for WRF-C when compared to that for WRF-T. A shear layer above the canopy causes increased turbulence within close proximity to the top of

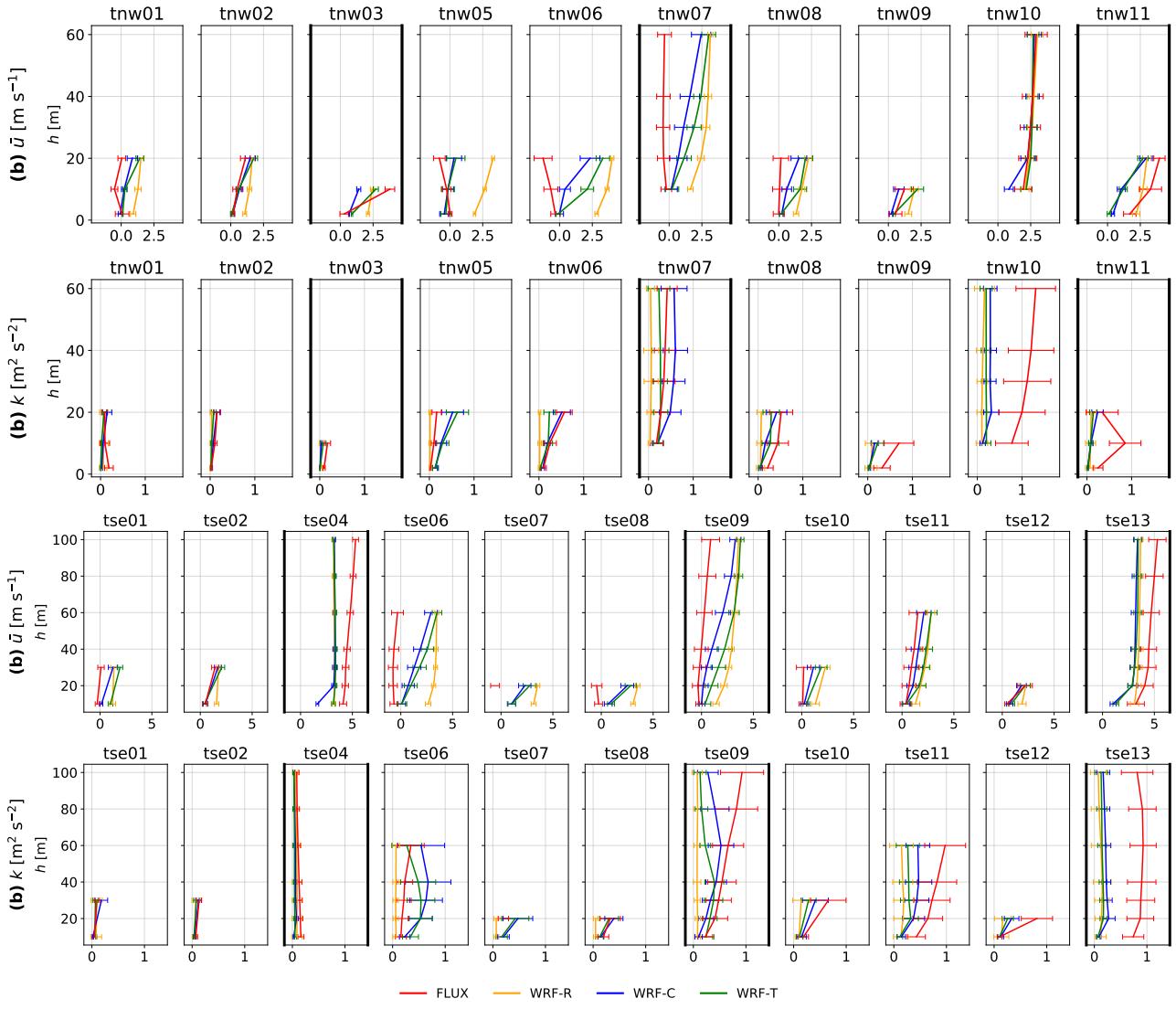

Figure 24: Mean across-valley wind velocity $\bar{u}$ [ms^{-1}] and TKE per unit mass k [m^{2}s^{-1}] over the selected time period for towers in the north, (a) to (b), and south, (c) to (d), transects. Error bars show the standard deviation over the STP for each instrument. The towers at the ridge-tops and at the lowest point within the valley are marked with thick black lines

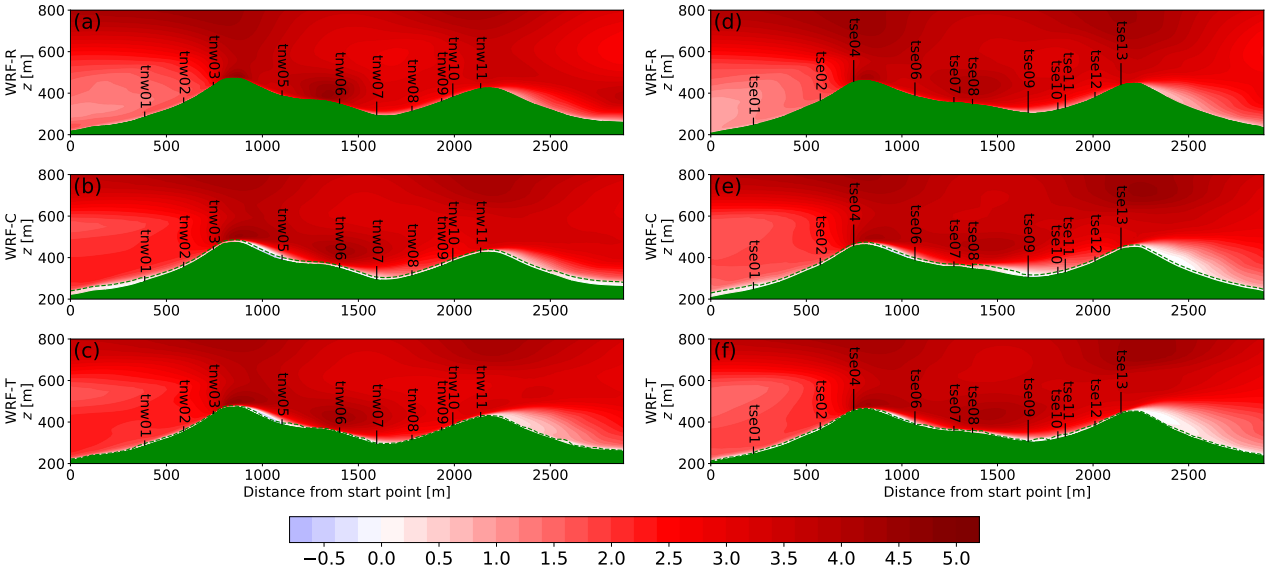

Figure 25: Cross-sections showing the mean across-valley wind velocity $\bar{u}$ [ms^{-1}] over the selected time period at the location of the north (left) and south (right) transects of towers for WRF-C, WRF-R and WRF-T. Canopy height is marked by a dashed green line for simulations using a canopy model and towers are marked with their reference name and the height of the maximum instrument in brackets

the canopy. While the canopy for WRF-C is fairly constant in height, with only occasional steps to a taller canopy, the height of the canopy used for WRF-T is much more variable. This variability in canopy height is leading to a reduction in k above the canopy because this shear layer is being shifted in height and broken up where interacting with a taller section of canopy. This reduction in k caused by a change in canopy height can also be seen in the results of WRF-C by comparing the regions downstream of tnw06 and tse08 in Fig. 26(b) and (e), respectively.

The wake in the lee of the upstream ridge in the canopy model cases is different to that which is formed by an isolated ridge. It tends to follow the terrain downwards in to the valley, rather than spreading horizontally from the top of the ridge in the downstream direction. The wake formed after the downstream ridge is much more similar to that which would be expected for a single ridge or hill. The two ridges are of equivalent height at the southern transect but, at the northern transect, the downstream ridge is around 45 m shorter than the upstream ridge. The wake formed by the downstream ridge at the southern transect spreads horizontally from the top of the ridge, elevated by 10 to 20 m in height for WRF-C and WRF-T. At the downstream ridge of the northern transect the wake is again tending to follow the terrain downwards, more so for WRF-C than for WRF-T, where an elevated section of canopy around tnw11 is diverting the flow higher over the ridge-top.

4.6.3 Along-valley flow

While the across-valley flow tends to be reproduced more accurately by the simulations using a canopy model to represent the vegetation at the surface, the same is not true for the along-valley

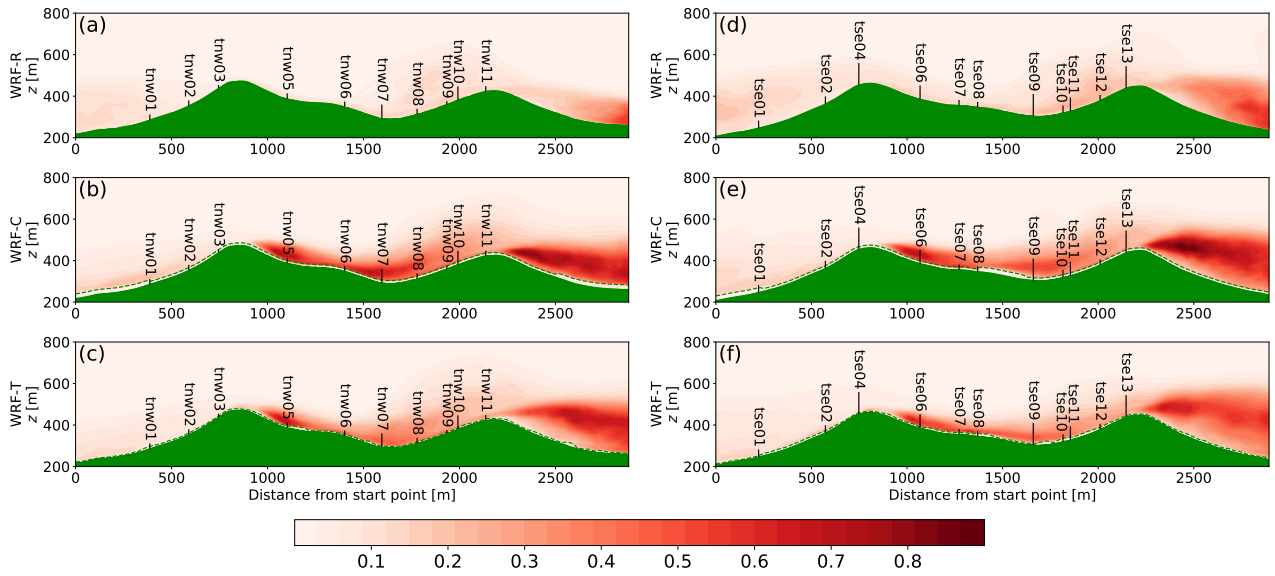

Figure 26: Cross-sections showing the TKE per unit mass k [m^2s^{-2}] over the selected time period at the location of the north (left) and south (right) transects of towers for WRF-C, WRF-R and WRF-T. Canopy height is marked by a dashed green line for simulations using a canopy model and towers are marked with their reference name and the height of the highest instrument in brackets

wind velocity. Figure 27 shows the along-valley component of the wind averaged over the STP $\bar{v}$ for the north and south transects of flux towers. At most positions $\bar{v}$ is negligible for both the measurements and the simulations. On the windward slope of the upstream ridge, the wind is being diverted towards the north-west, giving $\bar{v}$ a positive value. While this is reproduced well by WRF-R, the canopy simulations show the wind being diverted in the opposite direction. As can be seen in Fig. 28, there is a region between $z = 350$ and 650 m at the northern transect and between $z = 450$ and 650 m at the southern transect where $\bar{v}$ is positive for both canopy model cases. However, this region of positive $\bar{v}$ does not extend down to the ground level as it does for WRF-R or the flux tower measurements, except for a very small region around tower tnw01.

As the flow proceeds past towers tnw03, tnw05 and tnw06, the measured $\bar{v}$ gradually becomes negative within close proximity of the ground. This is not reproduced in any of the simulations, with the simulations using a canopy model measuring negligible along-valley winds, WRF-R still showing $\bar{v}$ to be positive for each tower and all of the simulations incorrectly producing positive $\bar{v}$ at the location of tnw05. Wagner et al. (2019) was able to reproduce the along-valley wind in a numerical simulation using a canopy model for a 49 day period of the Perdigão experiment but reported that these were considerably under-estimated. It was suggested that a more detailed representation of the canopy may solve this discrepancy with the observations but that does not seem to be the case for WRF-T. The remaining towers of the northern transect then show negligible $\bar{v}$ at all available instrument heights, though more variation is visible from the larger standard deviations close to the downstream ridge. At tnw07, tnw10 and tnw11 the along valley wind is still reproduced better by WRF-R than WRF-C or WRF-T. Similarly to the region of positive $\bar{v}$ upwind of the upstream

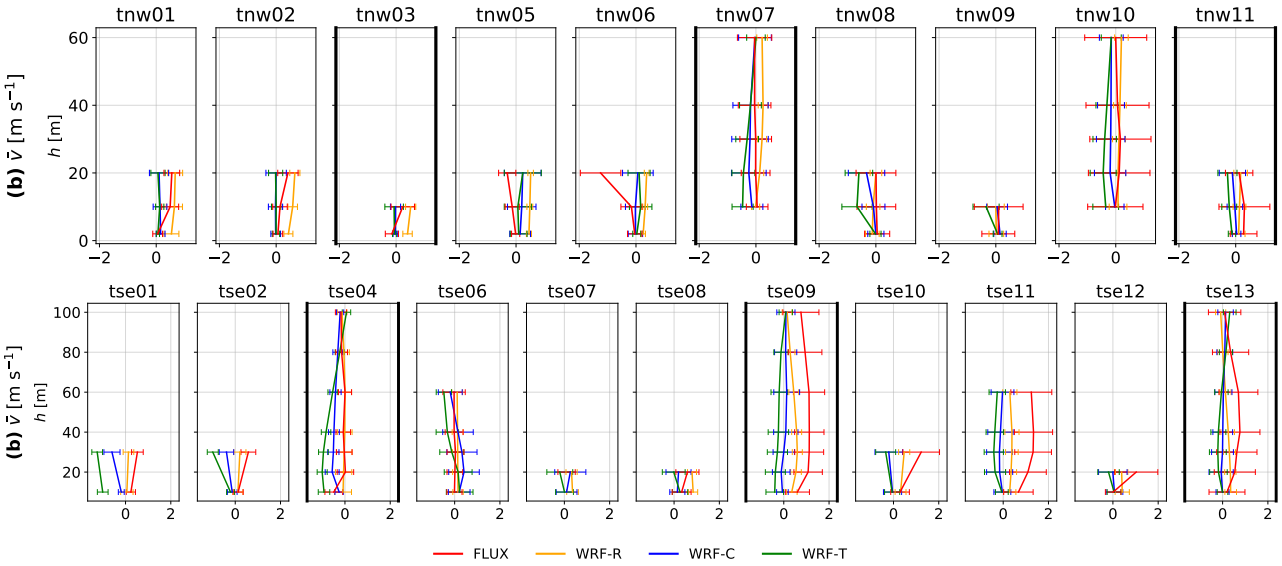

Figure 27: Mean along-valley wind velocity $\bar{v}$ [ms^{-1}] over the selected time period for towers in the (a) north and (b) south transects. Error bars show the standard deviation over the selected time period for each instrument. The towers at the ridge-tops and at the lowest point within the valley are marked with thick black lines

ridge, the canopy simulations are producing a region of positive $\bar{v}$ at these locations but it has been elevated to a height that is above the ground level and the top level of the flux towers.

The strongest along-valley flows are measured at the southern transect, between tower tse09 at the lowest level of the valley system and tse13, the tower at the top of the downstream ridge. At this location there is a positive $\bar{v}$ measured at every instrument height on each of the towers, though becoming negligible at the top of tower tse13. For WRF-R, $\bar{v}$ remains below half of the measured value but is also positive and follows the distribution of $\bar{v}$ with height in a manner similar to the measured values. The simulations using a canopy model do not reproduce the along-valley component of the wind well in this location. The region of positive $\bar{v}$ has been elevated to approximately $100\,$m above the ground level (see Fig. 28(e) and (f)). It appears that the increased turbulence seen close to the ground in the canopy simulations is leading to a vertical displacement of the region of positive $\bar{v}$.

It should also be noted that while WRF-R reproduces $\bar{v}$ correctly, the overall wind speed and direction are not the same as that seen in the measurements. It can be seen in Fig. 23 that, while WRF-R is the only simulation carried out here that shows a diversion of the wind towards the north-west within the valley, the mean wind direction is predominantly in the across-valley direction. Conversely, the measurements at towers within the valley show greatly reduced mean wind speeds below $h = 60\,$m and a mean flow almost directly along the valley.

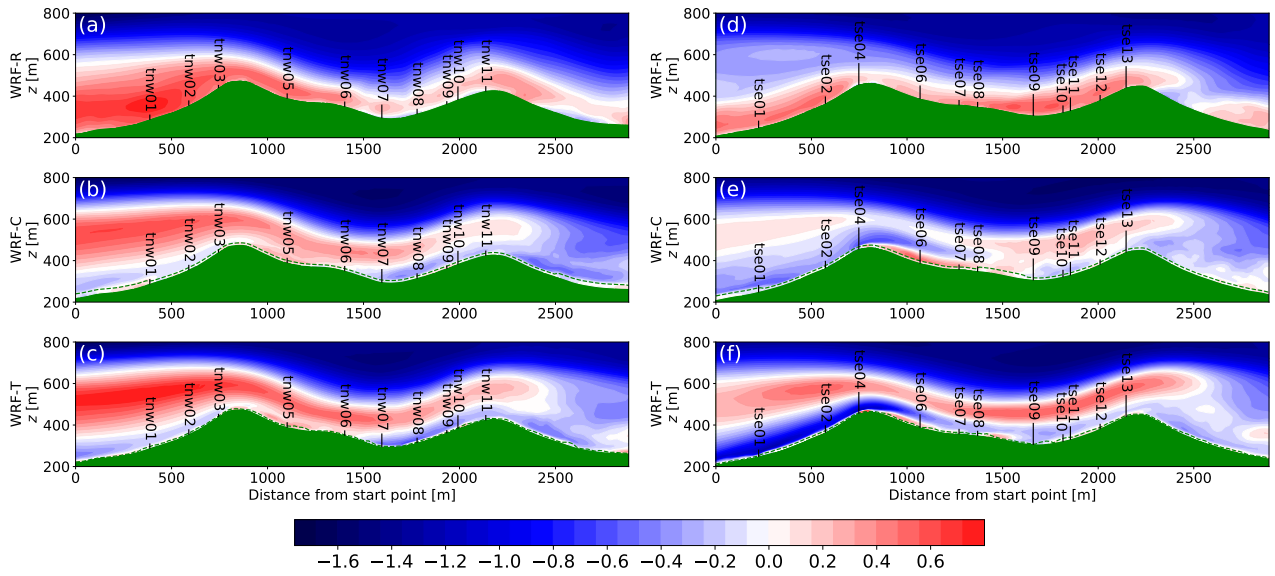

Figure 28: Cross-sections showing the mean along-valley wind velocity $\bar{v}$ [ms^{-1}] over the selected time period at the location of the north (left) and south (right) transects of towers for WRF-C, WRF-R and WRF-T. Canopy height is marked by a dashed green line for simulations using a canopy model and towers are marked with their reference name and the height of the highest instrument in brackets

4.6.4 Flow Recirculation

The reversal of the flow caused by the forested ridges is difficult to discern from time averaged wind speeds and directions as flow reversal is not always constant over time. It is therefore more advantageous to inspect the fraction of time for which reversed flows are occurring at different positions, as shown in Fig. 29 for all towers where reversed flows were measured. The first column shows the two towers situated upstream of the valley system, where reversed flows close to the ground are not generally reproduced in the results of the simulations. Reversed flows at tower tnw01 are only seen for WRF-C and only at $h = 10\,\mathrm{m}$. This occurs for 60% of the STP, approximately 40% more often than that seen in the measurements. This tower is positioned immediately downstream of a change in canopy height h_c from 20 to $10\,\mathrm{m}$. The wind speed from the mean south-westerly direction is reduced at low levels, while eddies generated by the forest edge are causing re-circulation above the shorter canopy around the tower. Tower tse01 is situated within the elevated section of canopy, where $h_c = 20\,\mathrm{m}$, and reversed flows are not occurring at this location. For WRF-T there is very little vegetation immediately upstream of tse01 and the canopy around tnw01 is of equivalent height to that for WRF-C but without the elevated section of canopy immediately upstream. The flow is therefore proceeding over the canopy without interruption, similar to WRF-R but with lower stream-wise velocity due to the increased friction caused by the explicit modelling of the reduction in momentum within the vertical extent of the canopy.

The flow direction is reversed much more often for the two towers immediately downwind of the upstream ridge-top, as is expected. At the southern transect, the wind direction at tower tse06 is

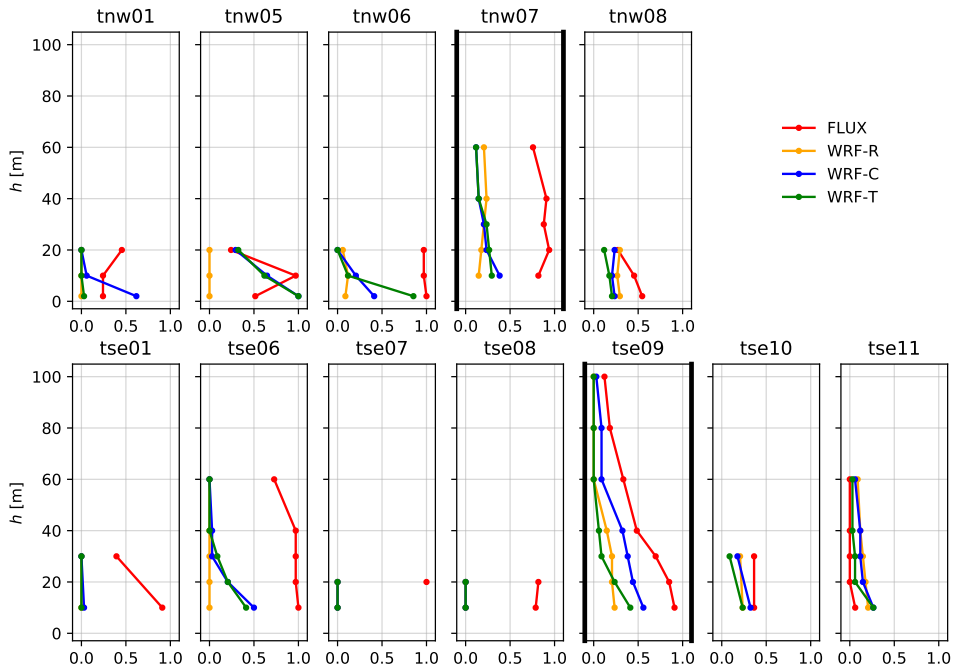

Figure 29: Fraction of time during the selected time period that the across-valley component of the wind u was measured to be negative at any instrument height for the measurements, WRF-C, WRF-R and WRF-T

reversed for almost 100% of the STP where $h \leq 40\,\text{m}$ and 70% of the time at $h = 60\,\text{m}$. The reduction in the flow reversal fraction between $h = 40$ and $60\,\text{m}$ is being caused by the uninterrupted flow passing over the ridge-top approximately $50\,\text{m}$ above the base of the tower. For the canopy model cases the flow over the ridge-top appears to be reaching further down the slope, as the flow reversal falls off at a lower height of $h = 30\,\text{m}$. The fraction of time for which the flow is reversed in the results of the simulations is much less substantial than is seen in the measurements. For the simulations using a canopy model the reversal fraction at tse06 is half of that measured at ground level and reduces above, while WRF-R fails to produce reversed flows at any height at any time. Measured flow reversal occurs between 25 and 100% of the STP for tower tnw05, more often at $h = 10\,\text{m}$ than above or below. This is captured well by the canopy model simulations at $h = 20\,\text{m}$, but is under-predicted by 40% at $h = 10\,\text{m}$ and over-predicted by 100% at $h = 2\,\text{m}$. The representation of the canopy at towers tnw05 and tse06 are similar for WRF-C and WRF-T. However, the canopy is gradually increasing in height as the flow approaches and passes tnw05 and of minimal height downstream of tse06 for WRF-T. For WRF-C the canopy height and density remain constant immediately upstream and downstream of these towers. This difference in canopy properties is not leading to a significant difference in the simulated flow reversal fraction between the two canopy model cases. The difference in the terrain between the two transects appears to be having a larger effect. A bulge in the terrain of the lee slope at the northern transect appears to be the pre-dominant factor leading to increased flow reversal at tnw05 compared to tse06 for the canopy model cases, but does not cause recirculation to occur for WRF-R.

The third to last columns of Fig. 29 all show towers that are within the valley, with the most south-westerly towers to the left and those further to the north-east towards the right. Towers tnw06, tnw07, tse07 and tse08 are all situated on the lee slope of the upstream ridge where it descends towards the low point at the middle of the valley. The flow reversal fraction of the measured across-valley wind velocity reduces from 100% for the available instrument heights on tnw06 and tse07, to between 75 and 90% once the flow has reached tnw07 and tse08. The two southern towers are on a relatively flat section of terrain, whilst the northern towers are situated slightly further downstream and on a section of terrain which descends more steeply towards the lowest point of the valley. The towers of the southern transect are also located at a position where the faster flow moving over the ridge has descended to the ground level for both canopy model cases (see Fig. 25), leading to a complete lack of reversed flows. This again indicates that the faster flow over the upstream ridge is descending down in to the valley more rapidly in the simulations than was measured. Tower tnw06 is located close to the top of the slope created by the bulge in the terrain and tnw07 is at the bottom of this slope at the lowest level of the valley cross-section. As is expected, reversed flow is occurring more often and over a greater vertical extent for tnw07, due to being positioned in the area of reduced flow present at this dip in the terrain. At these towers, flow reversal is beginning to occur for WRF-R, although significantly less than the canopy simulations at low levels, never more than 25% of the time and only for the north-western towers. For WRF-T the canopy around tnw06 is only modelled at the lowest grid level and this is leading to more than twice as much flow reversal at $h = 2\,\text{m}$ than for WRF-C, where the canopy is $10\,\text{m}$ tall and represented across two vertical grid levels.

Moving further downstream, towers tnw08 and tse09 are located around the lowest levels of the valley floor near the beginning of the windward slope of the downstream ridge. Flow reversal is still seen to be occurring here and all of the simulations are showing some amount of recirculation. This is not occurring as often as, but is reducing with height at a similar rate to the fraction of reversal seen in the measured u. At tse09 the flow reversal fraction for WRF-C exceeds that of WRF-T and this is again related to the fact that there is an elevated patch of canopy generating turbulence upstream of this tower for WRF-C. The canopy immediately upstream of this tower for WRF-T on the other hand, is less than $10\,\text{m}$ tall with little variation. The canopy upstream of tower tnw08 are much more similar between the two simulations with a canopy model, leading to much less variation in the fraction of reversed flows seen at this location. The modelled reversed flows occurring at these towers are limited to the end of the STP when recirculation is restricted to the lowest point of the valley.

Towers tse10 and tse11 are located within $60\,\text{m}$ of each other at the start of the windward slope of the downstream ridge, but show some difference in the fraction of reversed flows. Reversed flows are measured 35% of the time at tse10 and this is reproduced well by each of the simulations at $h = 10\,\text{m}$. The fraction of time for which u is negative falls to around half that measured at $h = 30\,\text{m}$ for all simulated results. At tse11 reversed flows are not measured for most instrument

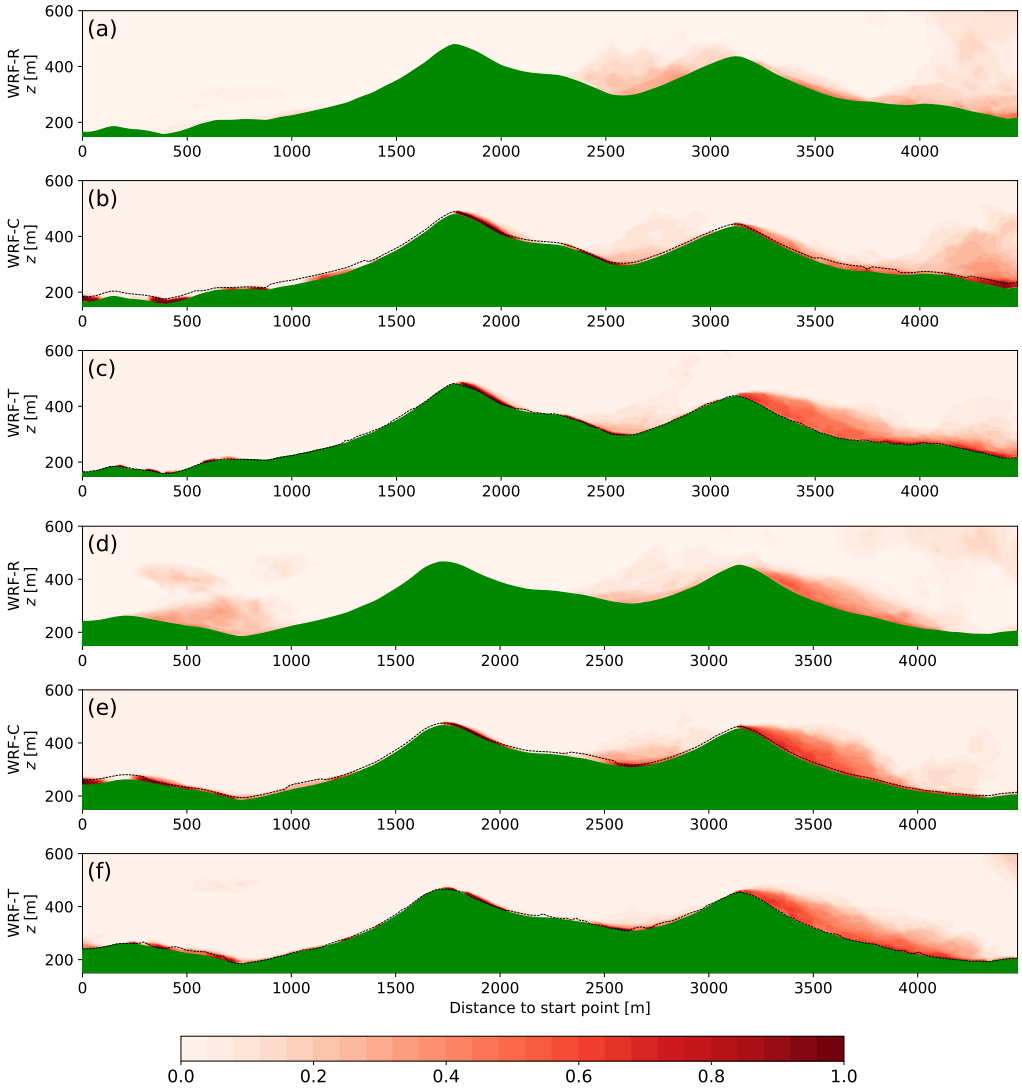

Figure 30: Cross-sections of the fraction of the selected time period for which the across-valley component of the wind u was negative for the north, (a) to (c), and south, (d) to (f), transects of towers across the range of the innermost domain for WRF-C, WRF-R and WRF-T. Canopy height is marked by a dashed black line for simulations using a canopy model

heights, occurring only at $h = 10$ m but for less than 10% of the STP. The results for each simulation show reversed flows for 25% of the STP at $h = 10$ m, with reversed flows at all instrument heights above this for WRF-C and WRF-R for 10 to 20% of the STP. The distribution of reversed flows with height for WRF-T matches more closely with the measurements, falling to almost zero at $h = 20$ m. The most noticeable difference between these two towers is in the canopy cover situated immediately upstream. Both towers are located within an area of canopy of measured height $h_c \approx 8$ m, that extends around 100 m upstream and then reduces to small patchy sections of canopy with $h_c \leq 5$ m. For tse11, the section of reduced canopy height continues until 375 m upstream of the tower, where an elevated section of canopy with $h_c \approx 15$ m is present. This elevated section of canopy is closer to tse10, starting 300 m upstream of the tower and quickly rising to a sharp peak of $h_c = 18$ m, 30 m further upstream. For WRF-C the canopy height doubles to $h_c = 20$ m approximately 360 m upstream of both towers and then returns to $h_c = 10$ m, 200 m upstream, remaining at this height up to the base of the tower. This elevated section of canopy is modelled using a change in surface roughness length from $z_0 = 0.06$ m to 0.2 m for WRF-R at the same location. The more detailed representation of the canopy used in WRF-T appears to be providing a more accurate distribution of the flow reversal fraction at tse11 but not at tse10. While WRF-R shows less flow reversal at $h = 10$ m at tse10, the results are not very different from those for WRF-C.

An overview of the recirculation fraction for each simulated case at the north and south transect are presented in Fig. 30. The recirculation is predominantly occurring in the lee of the downstream ridge for each simulated case. For WRF-R the only other location where recirculation is regularly occurring is above the lowest point between the two ridges, where recirculation was seen to occur towards the end of the STP, and in the dip that is upstream of the valley, where reversed flows are present up to 250 m above the surface. While reversed flows are occurring upstream of the valley for the canopy model cases, they tend to be limited to within the canopy itself at locations downstream of terrain features, with more frequent and extensive recirculation occurring over locations with the deepest canopies. This is in line with the findings of Ross and Baker (2013), who found that recirculating flow tended to be restricted to locations within the canopy for partially forested hills. Small regions of frequent reversed flows are present on the windward slope of the upstream ridge, as was measured by the towers in this area, but these tend to be limited to the lower half of the slope where a canopy is present. At the northern transect, in the lee of the upstream ridge, the frequency of reversed flows is more extensive than at the southern transect, similar to the reversed flows seen in Fig. 21. This location at the northern transect is the only place where recirculation is occurring for a large fraction of the STP above the canopy, but only up to approximately $h = 2h_c$. Reversed flows across most of the valley are again limited to within the canopy on slopes that are descending in the direction of the mean flow above the valley. However, the period of recirculation towards the end of the STP above the lowest point of the valley does lead to a small fraction of reversed flows at this location extending well above the canopy.

4.7 Conclusions and Discussion

For periods where the flow is perpendicular to the extensively forested Vale Cobrão, the use of a vertically resolved canopy model in numerical simulations provided significant improvements over the use of standardised, land use category dependent surface roughness. In order to quantify the improvement, the root-mean-squared-error (RMSE) was calculated for the across-valley, along-valley and vertical velocity, the variances in these velocities and across-along-valley, across-vertical and along-vertical momentum flux per unit mass between each simulated case and the measured values for all heights on all of the flux towers listed in Table 3. Before calculating the RMSE, these quantities were all normalised by either the absolute (positive) mean or maximum of the measured values and thresholds of 0.1, 0.5 or 1 were applied to avoid dividing by numbers close to zero. The average of all of these RMSEs was then taken to provide a range of scores for each case.

This average normalised RMSE was 25 to 48% larger for WRF-R than for WRF-C or WRF-T, while for WRF-C it was 3 to 12% larger than for WRF-T. The difference in average RMSE between the results of each simulated case for many of these quantities are small, with the RMSEs for WRF-R being within 10 to 15% of the canopy model cases. However, for the across-valley velocity u and the vertical velocity w, the average RMSE is 150 to 250% larger for WRF-R. The canopy model cases therefore provide a more accurate description of the mean wind speeds over the double ridge system within close proximity to the canopy. The improvement in the accuracy of reproducing wind velocity variances and momentum fluxes is less clear, although the canopy model cases were also shown to provide a magnitude of TKE closer to that seen in the measurements than WRF-R. None of the simulations performed here reproduced the same magnitude of TKE measured at the downstream ridge.

The effect of the double-ridge system on the large-scale flow is not dramatically different between the simulated cases. The wind field well above the ridge-tops and the properties of the flow at the flux towers furthest downstream show very similar values regardless of the method used to represent the canopy. This indicates that for larger scale modelling with more coarse resolutions, the representation of the vegetation at the surface may not be so important. However, the canopy model is providing significant improvements to the reproduction of the flow within the valley, at least for this semi-idealised case of perpendicular flow over a double-ridge system with a fairly constant two-dimensional profile. The increased friction close to the surface where a canopy model is used leads to much slower wind speeds near the ground, more in line with those that were measured. Within the valley the mean wind speed is over-predicted more with increasing height by the canopy model cases and above $h = 60\,\mathrm{m}$ they tend to fall more in line with the over-predictions of WRF-R. In general, the across-valley wind speed, TKE and fraction of time that reversed flows are present for the canopy model cases tend to lie somewhere between the results of WRF-R and the measurements.

The main advantage was in the reproduction of recirculation zones downstream of the ridge-tops. While some recirculation was seen in the lee of the downstream ridge for WRF-R, it was not as

extensive or as frequent as that seen in the results of the simulations using a canopy model. At the upstream ridge, the canopy model cases provide a frequency and extent of recirculation that shows much better agreement with the measurements. However, the fraction of time that reversed flow is present at the flux towers reduces more rapidly with height than is seen in the measurements. The upstream ridge does not induce recirculation in the case of WRF-R, with the flow remaining attached to the lee slope of the ridge at all times. Measured reversed flows are not seen in the results of WRF-R until the middle of the valley system, where the reversed flow fraction tends to be more similar between the simulated cases but with WRF-C and WRF-T performing better close to the ground. Close to the base of the downstream ridge the simulated cases all show a similar frequency of flow reversal and all are consistent with the measurements.

The different canopy distributions used for the canopy model cases do not tend to have a large impact on the wind speeds above. However, the more variable height and density of the canopy used for WRF-T tends to induce less turbulence above than the generally homogeneous canopy used for WRF-C. The difference between the faster flow over the canopy and the much slower flow within the canopy produces a shear layer and hence turbulence above the canopy. Over a flat canopy, this layer is uninterrupted and turbulence builds up as the flow proceeds downstream. If the canopy height then increases, this layer of shear is interrupted and the flow moves in to the top of the elevated section of canopy where TKE and momentum are reduced. The wind shear at canopy top is then reduced and this process results in less turbulence being generated above the canopy. While the more accurate representation of the canopy in WRF-T does clearly modify the flow differently to the simplified canopy used in WRF-C, it does not tend to provide closer results to the measurements. Assigning canopy properties based on land use categories therefore provides significant benefits over a roughness-length approach to representing the surface vegetation and is equivalent to using more high resolution input. This was true even though the vertical resolution of these simulations was 0.2 to 0.5 of the canopy height, which might previously have been considered insufficient to reproduce the dynamics of the flow around a canopy accurately. It is however possible that if measured canopy data had been available over a wider area then the results for WRF-T may have been improved.

It should be noted that this work focussed on a relatively short period of time, over which the conditions were stable and mean wind speed and direction had very little variability. The results presented here also do not include a period of time where the mean flow was coming from the other side of the valley, to the north-east. Menke et al. (2019) investigated the presence of recirculating flows with the wind coming from both directions, but these results were averaged over the entire period of the Perdigão experiment. This experiment provides a good intermediary step between idealised simulations and real case studies in more complex terrain. It would be of interest to study the implications of using such a method in numerical simulations of a more complex valley system, if such data were available for comparison. However, there is some difficulty in disentangling the impact of the terrain on the flow from that of the canopy. It would, therefore, also be advantageous for more data to be collected about flows over a wider distribution of topographies and canopies

than is currently available for comparison with even idealised numerical simulations.

4.8 Acknowledgements

This work used the ARCHER UK National Supercomputing Service (http://www.archer.ac.uk) to carry out the numerical simulations and data processing was carried out using the University of Hertfordshire high-performance computing facility. The flux-tower data were provided by NCAR/EOL under the sponsorship of the National Science Foundation (https://data.eol.ucar.edu/).

4.9 References

K. W. Ayotte. Computational modelling for wind energy assessment. *Journal of Wind Engineering and Industrial Aerodynamics*, 96:1571–1590, 2008. doi:10.1016/j.jweia.2008.02.002.

S. Belcher, I. Harman, and J. Finnigan. The wind in the willows: Flows in forest canopies in complex terrain. *Annual Review of Fluid Mechanics*, 44(1):479–504, 2012. doi:10.1146/annurev-fluid-120710-101036.

J. Berg, J. Mann, A. Bechmann, M. S. Courtney, and H. E. Jørgensen. The bolund experiment, part i: Flow over a steep, three-dimensional hill. *Boundary-Layer Meteorology*, 141(219), 2011. doi:10.1007/s10546-011-9636-y.

A. R. Brown, J. M. Hobson, and N. Wood. Large-eddy simulation of neutral turbulent flow over rough sinusoidal ridges. *Boundary-Layer Meteorology*, 98:411–441, 2001. doi:10.1023/A:1018703209408.

X. Cheng, J. Gulliver, and D. Zhu. Application of displacement height and surface roughness length to determination boundary layer development length over stepped spillway. *Water*, 6(12):3888–3912, 2014. doi:10.3390/w6123888.

T. L. Clark and S. J. Mitchell. Three-dimensional simulations of air flow and momentum transfer in partially harvested forests. *Boundary-Layer Meteorology*, 125:505–524, 2007. doi:10.1007/s10546-007-9199-0.

J. W. Deardorff. Stratocumulus-capped mixed layers derived from a three-dimensional model. *Boundary-Layer Meteorology*, 18:495–527, 1980. doi:10.1007/BF00119502.

S. Dupont and Y. Brunet. Edge flow and canopy structure: A large-eddy simulation study. *Boundary Layer Meteorology*, 126:51–71, 2008a. doi:10.1007/s10546-007-9216-3.

S. Dupont and Y. Brunet. Influence of foliar density profile on canopy flow: A large-eddy simulation study. *Agricultural and Forest Meteorology*, 148:976–990, 2008b. doi:10.1016/j.agrformet.2008.01.014.

S. Dupont and Y. Brunet. Coherent structure in canopy edge flow: a large-eddy simulation study. *Journal of Fluid Mechanics*, 630:93–128, 2009. doi:10.1017/S0022112009006739.

S. Dupont, Y. Brunet, and J. Finnigan. Large-eddy simulation of turbulent flow over a forested hill: Validation and coherent structure identification. *Quarterly Journal of the Royal Meteorological Society*, 134(1):1911–1929, 2008. doi:10.1002/qj.328.

H. Fernando, J. Mann, J. Palma, J. Lundquist, R. Barthelmie, M. BeloPereira, W. Brown, F. Chow, T. Gerz, C. Hocut, P. Klein, L. Leo, J. Matos, S. Oncley, S. Pryor, L. Bariteau, T. Bell, N. Bodini, M. Carney, M. Courtney, E. Creegan, R. Dimitrova, S. Gomes, M. Hagen, J. Hyde, S. Kigle, R. Krishnamurthy, J. Lopes, L. Mazzaro, J. Neher, R. Menke, P. Murphy, L. Oswald, S. Otarola-Bustos, A. Pattantyus, C. Rodrigues, A. Schady, N. Sirin, S. Spuler, E. Svensson, J. Tomaszewski, D. Turner, L. van Veen, N. Vasiljevic, D. Vassallo, S. Voss, N. Wildmann, and Y. Wang. The perdigão: Peering into microscale details of mountain winds. *Bulletin of the American Meteorological Society*, 2019. doi:10.1175/BAMS-D-17-0227.1.

J. Finnigan and S. Belcher. Flow over a hill covered with a plant canopy. *Quarterly Journal of the Royal Meteorological Society*, 130(596):1–29, 2004. doi:10.1256/qj.02.177.

J. Finnigan, K. Ayotte, I. Harman, G. Katul, H. Oldroyd, E. Patton, D. Poggi, A. Ross, and P. Taylor. Boundary-layer flow over complex topography. *Boundary-Layer Meteorology*, 177:247–313, 2020. doi:10.1007/s10546-020-00564-3.

N. J. Froelich, C. S. B. Grimmond, and H. P. Schmid. Nocturnal cooling below a forest canopy: Model and evaluation. *Agricultural and Forest Meteorology*, 151:957–968, 2011. doi:10.1016/j.agrformet.2011.02.015.

E. Grant, A. Ross, B. Gardiner, and S. Mobbs. Field observations of canopy flows over complex terrain. *Boundary-Layer Meteorology*, 156(2):231–251, 2015. doi:10.1007/s10546-015-0015-y.

E. Grant, A. Ross, and B. Gardiner. Modelling canopy flows over complex terrain. *Boundary-Layer Meteorology*, 161(3):417–437, 2016. doi:10.1007/s10546-016-0176-3.

M. J. Iacono, J. S. Delamere, E. J. Mlawer, M. W. Shephard, S. A. Clough, and W. D. Collins. Radiative forcing by long-lived greenhouse gases: Calculations with the aer radiative transfer models. *Journal of Geophysical Research: Atmospheres*, 113(D13), 2008. doi:10.1029/2008JD009944.

A. Jarvis, H. I. Reuter, A. Nelson, and E. Guevara. Hole-filled srtm for the globe version 4, available from the cgiar-csi srtm 90m database, 2008. URL `https://cgiarcsi.community/data/srtm-90m-digital-elevation-database-v4-1/`. Accessed 28th February 2019.

J. Kaimal and J. Finnigan. *Atmospheric boundary layer flows. Their structure and measurements*. Oxford University Press, New York, USA, 1994.

M. H. Kobayashi, J. C. F. Pereira, and M. B. B. Siqueira. Numerical study of the turbulent flow over and in a model forest on a 2d hill. *Journal of Wind Engineering and Industrial Aerodynamics*, 53:357–374, 1994. doi:10.1016/0167-6105(94)90091-4.

Z. Liu, T. Ishihara, X. He, and H. Niu. Les study on the turbulent flow fields over complex terrain covered by vegetation canopy. *Journal of Wind Engineering and Industrial Aerodynamics*, 155: 60–73, 2016. doi:10.1016/j.jweia.2016.05.002.

R. Menke, J. Mann, and N. Vasiljevic. Perdigão-2017: multi-lidar flow mapping over the complex terrain site, 2018.

R. Menke, N. Vasiljević, J. Mann, and J. K. Lundquist. Characterization of flow recirculation zones at the perdigão site using multi-lidar measurements. *Atmospheric Chemistry and Physics*, 19(4): 2713–2723, 2019. doi:10.5194/acp-19-2713-2019.

R. Menke, N. Vasiljević, J. Wagner, S. P. Oncley, and J. Mann. Multi-lidar wind resource mapping in complex terrain. *Wind Energy Science*, 5(3):1059–1073, 2020. doi:10.5194/wes-5-1059-2020.

National Centers for Environmental Prediction, National Weather Service, NOAA, U.S. Department of Commerce. Ncep fnl operational model global tropospheric analyses, continuing from july 1999, 2000. URL 10.5065/D6M043C6. Accessed 18th September 2019.

H. G. Ouwersloot, A. F. Moene, and J. J. Attema. Large-eddy simulation comparison of neutral flow over a canopy: sensitivities to physical and numerical conditions, and similarity to other representations. *Boundary-Layer Meteorology*, 162:71–89, 2017. doi:10.1007/s10546-016-0182-5.

J. L. Palma and V. Batista. Perdigão: Digital terrain model in 2 m resolution (2019 version). URL https://doi.org/10.34626/uporto/8t7k-3h34. Accessed 3rd December 2019.

J. L. Palma and V. Batista. Perdigão: Leaf area index map in 2m resolution (2019 version), 2019a. URL 10.34626/uporto/382c-gh41. Dataset published 2021 via Faculty of Engineering, University of Porto. Accessed 3rd December 2019.

J. L. Palma and V. Batista. Perdigão: Canopy height model for 2017 vegetation height in 2m resolution (2019 version), 2019b. URL 10.34626/uporto/4x50-fr07. Dataset published 2021 via Faculty of Engineering, University of Porto. Accessed 3rd December 2019.

J. M. L. M. Palma, A. S. Lopes, V. C. Gomes, C. V. Rodrigues, R. Menke, N. Vasiljević, and J. Mann. Unravelling the wind flow over highly complex regions through computational modeling and two-dimensional lidar scanning. *Journal of Physics: Conference Series*, 1222:012006, 2019. doi:10.1088/1742-6596/1222/1/012006.

E. G. Patton and G. G. Katul. Turbulent pressure and velocity perturbations induced by gentle hills covered with sparse and dense canopies. *Boundary-Layer Meteorology*, 133:189–217, 2009. doi:10.1007/s10546-009-9427-x.

N. Pineda, O. Jorba, J. Jorge, and J. M. Baldasano. Using noaa avhrr and spot vgt data to estimate surface parameters: application to a mesoscale meteorological model. *International Journal of Remote Sensing*, 2004. doi:10.1080/0143116031000115201.

D. Poggi and G. G. Katul. Turbulent flows on forested hilly terrain: the recirculation region. *Quarterly Journal of the Royal Meteorological Society*, 133:1027–1039, 2007. doi:10.1002/qj.73.

A. Ross and T. Baker. Flow over partially forested ridges. *Boundary-Layer Meteorology*, 146: 375–392, 2013. doi:10.1007/s10546-012-9766-x.

A. Ross and S. Vosper. Neutral turbulent flow over forested hills. *Quarterly Journal of the Royal Meteorological Society*, 131(609):1841–1862, 2005. doi:10.1256/qj.04.129.

A. N. Ross. Large-eddy simulations of flow over forested ridges. *Boundary-Layer Meteorology*, 128: 59–76, 2008. doi:10.1007/s10546-008-9278-x.

A. N. Ross. Scalar transport over forested hills. *Boundary-Layer Meteorology*, 141:179–199, 2011. doi:10.1007/s10546-011-9628-y.

A. N. Ross. Boundary-layer flow within and above a forest canopy of variable density. *Quarterly Journal of the Royal Meteorological Society*, 138(666):1259–1272, 2012. doi:10.1002/qj.989.

R. H. Shaw and E. G. Patton. Canopy element influences on resolved- and subgrid-scale energy within a large-eddy simulation. *Agricultural and Forest Meteorology*, 115:5–17, 2003. doi:10.1016/S0168-1923(02)00165-X.

R. H. Shaw and U. Schumann. Large-eddy simulation of turbulent flow above and within a forest. *Boundary-Layer Meteorology*, 61:47–64, 1992. doi:10.1007/BF02033994.

W. C. Skamarock, J. B. Klemp, J. Dudhia, D. O. Gill, Z. Liu, J. Berner, W. Wang, J. G. Powers, M. G. Duda, D. M. Barker, and X. Y. Huang. A description of the advanced research wrf version 4. *NCAR Technical Note NCAR/TN-556+STR*, page 145, 2019. doi:10.5065/1dfh-6p97.

H. Tan and S. Ling. *Quasi-steady micrometeorological Atmospheric Boundary Layer over a Wheat Field*. Therm Inc., Ithaca, New York, USA, 1960.

N. Tani. The wind on the cultivated field (in japanese, english summary. *Journal of Agricultural Meteorology*, 16(3):89–93, 1963. doi:10.2480/agrmet.16.89.

P. A. Taylor and H. W. Teunissen. The askervein hill project: Overview and background data. *Boundary-Layer Meteorology*, 39:15–39, 1987. doi:10.1007/BF00121863.

G. Thompson, P. R. Field, R. M. Rasmussen, and W. D. Hall. Explicit forecasts of winter precipitation using an improved bulk microphysics scheme. part ii: Implementation of a new snow parameterization. *Monthly Weather Review*, 136(12):5095–5115, 2008. doi:10.1175/2008MWR2387.1.

J. Tolladay and C. Chemel. Numerical modelling of neutral boundary-layer flow across a forested ridge. *Boundary-Layer Meteorology*, 2021. doi:10.1007/s10546-021-00628-y.

UCAR/NCAR-Earth Observing Laboratory. Ncar/eol quality controlled 5-minute isfs surface flux data, geographic coordinate, tilt corrected. version 1.1, 2019. URL `https://data.eol.ucar.edu/dataset/536.011`. Accessed 1st February 2019.

Z. Uchijima and J. Wright. An experimental study of air flow in a corn plant-air layer. *Bulletin of the National Institute of Agricultural Science*, 11(1):19–66, 1963.

A. Verhoef, K. McNaughton, and A. Jacobs. A parameterization of momentum roughness length and displacement height for a wide range of canopy densities. *Hydrology and Earth System Sciences*, 1(1):81–91, 1997. doi:10.5194/hess-1-81-1997.

J. Wagner, T. Gerz, N. Wildmann, and K. Gramitzky. Long-term simulation of the boundary layer flow over the double-ridge site during the perdigao 2017 field campaign. *Atmospheric Chemistry and Physics*, 2019. doi:10.5194/acp-19-1129-2019.

T. Watanabe. Large-eddy simulation of coherent turbulence structures associated with scalar ramps over plant canopies. *Boundary-Layer Meteorology*, 112:307–341, 2004. doi:10.1023/B:BOUN.0000027912.84492.54.

J. Wilson, J. Finnigan, and M. Raupach. A first-order closure for diturbed plant-canopy flows, and its application to winds in a canopy on a ridge. *Quarterly Journal of the Royal Meteorological Society*, 124(547):705–732, 1998. doi:10.1002/qj.49712454704.

X. Xu, C. Yi, and E. Kutter. Stably stratified canopy flow in complex terrain. *Atmospheric Chemistry and Physics*, 15:7457–7470, 2015. doi:10.5194/acp-15-7457-2015.

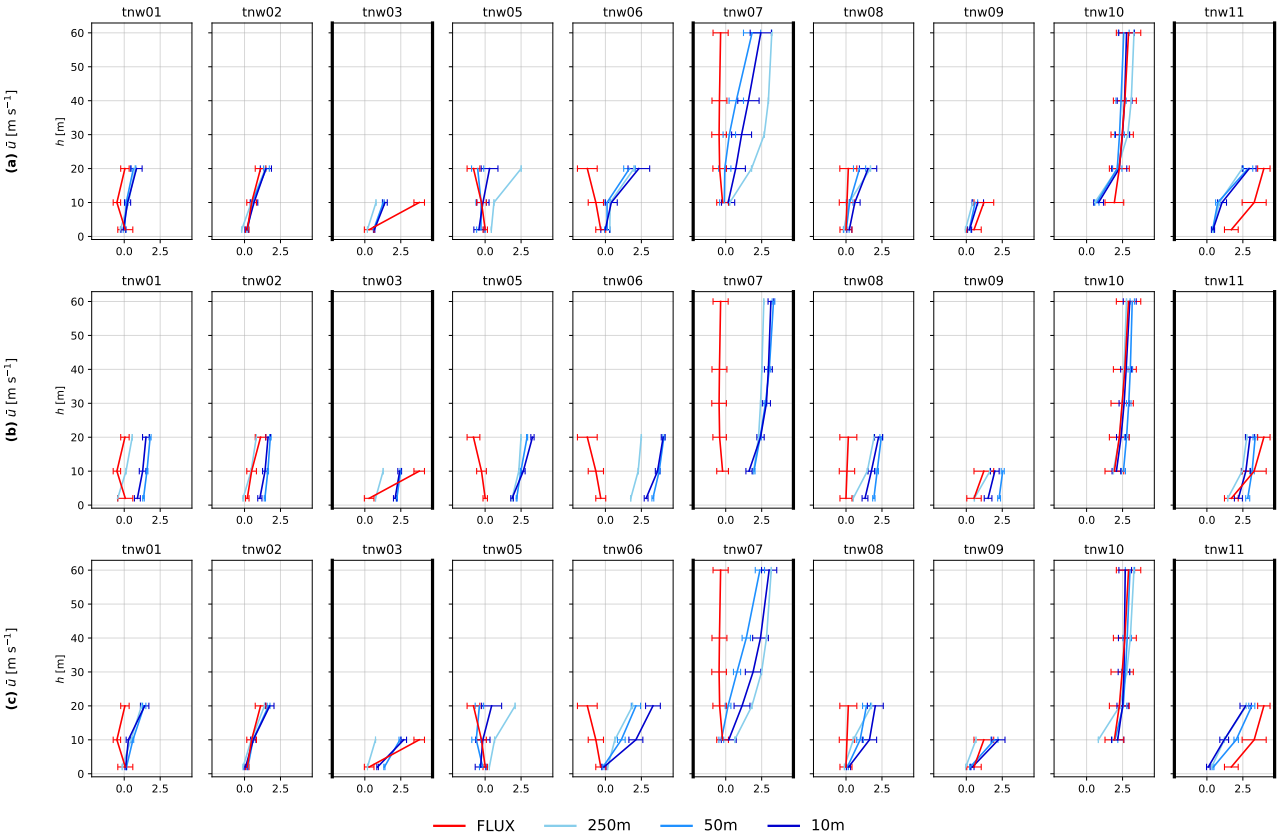

Figure 31: Mean across-valley wind velocity $\bar{u}$ [ms^{-1}] over the selected time period (STP) at towers in the northern transect for (a) WRF-C, (b) WRF-R and (c) WRF-T compared against the flux tower measurements. Error bars show the standard deviation over the STP for each instrument. The towers at the ridge-tops and at the lowest point within the valley are marked with thick black lines

4.10 Additional material: Effects of resolution

Something not discussed in this article was the results of the outermost two domains of the simulation. This was because analysis of the differences in the simulated flows for the different domains was beyond the scope of the article, however it is interesting to investigate this a little further. The innermost domain had a horizontal resolution of 10 m, while the two outer domains had resolutions of 50 m and 250 m. Comparing the various turbulence statistics recorded at the flux towers to the simulated flows in each domain is complex and would require a separate paper to be analysed thoroughly. As an example, the mean across-valley component of velocity over the STP $\bar{u}$ and the TKE k for the towers on the northern transect are presented in Fig. 31 and Fig. 32, respectively. The results for the 50 m domain are comparable to those of the 10 m domain in reproducing the flow over the valley for the simulations using a canopy model. For towers within the valley such as tnw05 and tnw07 the 50 m domains of the canopy model cases actually reproduced the average across-valley flow more accurately than the 10 m domain. The 250 m domain performed significantly worse in most positions and the results were more similar to the simulations that used a roughness length at the surface. For the STP as a whole, the TKE was near zero across the whole valley and

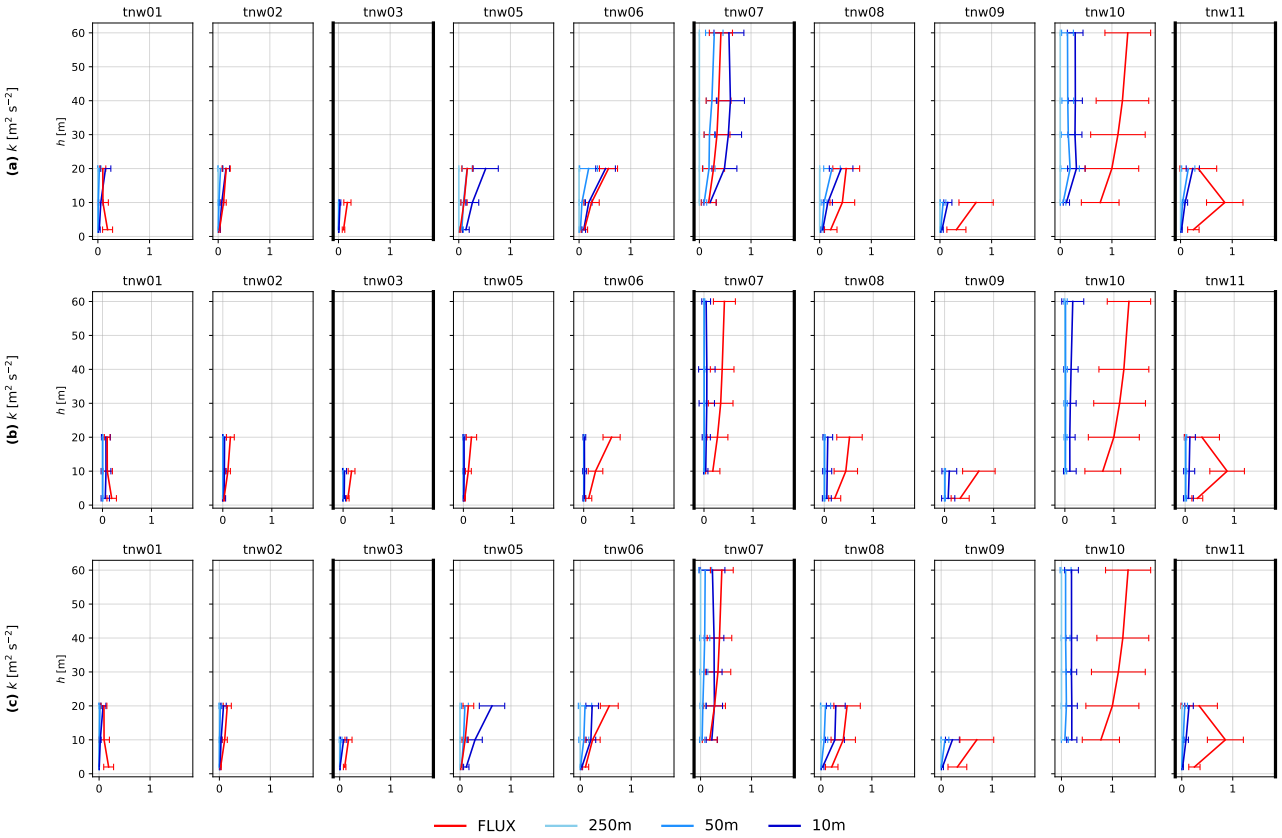

Figure 32: Turbulent kinetic energy per unit mass k [$m^2 s^{-1}$] over the selected time period (STP) at towers in the northern transect for (a) WRF-C, (b) WRF-R and (c) WRF-T compared against the flux tower measurements. Error bars show the standard deviation over the STP for each instrument. The towers at the ridge-tops and at the lowest point within the valley are marked with thick black lines

the mean across-valley flow was over-predicted. The results from the $250\,$m domain for WRF-R did however provide more accurate reproduction of the mean across-valley velocity at many positions across the valley when compared to the higher resolution domains. The deficiencies of the canopy model simulations with a $250\,$m horizontal resolution would indicate that the use of a canopy model is only beneficial when simulating at higher resolutions. The exact resolution required is likely to be dependent on the geometry of the terrain and the extent and height of the canopy cover at the site. As mentioned in Sect. 3, the only way to determine the resolutions required for different hill geometries and canopy properties would be to collect experimental data for a range of cases that could then be compared to the results of simulations using a wide range of different resolutions.

SECTION 5

Concluding remarks

The aim of this work was to implement a canopy model which gives a true vertical extent to a forest canopy in the WRF model and determine whether such a model could provide benefits over default methods for a real-world case study in forested complex terrain. After the model had been implemented it was tested against a benchmark wind-tunnel experiment for a neutral boundary-layer flow over an idealised two-dimensional forested ridge. The first article presented in Sect. 3 confirmed that this model was able to reproduce the results of this experiment and also investigated the sensitivity of the model to the horizontal resolution of the simulation. The flow velocity in the stream-wise direction over this ridge was found to be closer to the counterpart wind-tunnel measurements when the canopy model was used. Insufficient drag at the surface where the canopy is represented using an increased roughness length at the surface leads to an over-estimation of the wind speed above the canopy, which becomes larger as the flow proceeds downstream over the ridge. Using the roughness-length method led to deficiencies in the vertical velocity variance and turbulent kinetic energy above the canopy, with vertical turbulent structures also having an insufficient vertical extent. When the canopy model was used, the horizontal extent of the recirculation region was consistent regardless of the horizontal resolution used in the simulations. This was not true for the simulations where the canopy was represented using an increased roughness length at the surface. In this case the horizontal extent of the recirculation region was found to increase as the horizontal grid spacing was increased.

When using a roughness-length parameterisation and vertical resolutions smaller than that of the canopy elements being represented, the surface must be elevated to the displacement height of the canopy. The idea of a displacement height is ambiguous for a forest canopy, where non-zero velocities can be measured down to ground level. There are also issues with representing the edges of the canopy because the surface would have to be reduced to ground level again, creating a step in the terrain that would lead to erroneous effects. Simulations with a bottom grid level taller than the canopy were also performed for this idealised ridge using the roughness-length parameterisation, but this was not found to provide any benefits over simulations where the surface was elevated. For the simulation using a canopy model the discrepancies between the experimental measurements and the simulated values of stream-wise velocity and turbulence statistics were reduced as the horizontal grid spacing was reduced. A finer resolution did not however improve the results of simulations that used the roughness-length parameterisation. This method does not properly model the flow in and around the canopy, so reducing the horizontal grid spacing increases the number of grid cells over which errors can accumulate. Such accumulation of errors was also assumed to be the cause of

discrepancies in the wake region when using a canopy model to represent the canopy. The lack of improvement with increasing resolution in this wake region indicates that further improvements may be required to the canopy model. However, representing the complex structure of a forest canopy (or even the more simple artificial canopy used in the wind tunnel) as a porous block is always likely to lead to inconsistencies.

These results confirmed the findings of previous research that a change in roughness length at the surface can not replicate the effects of a relatively tall canopy in the modulation of the flow speed over a ridge. An explicit treatment of the canopy represents a significant improvement but also requires a fine spatial resolution in the horizontal and vertical dimensions to model the turbulent flow in a large-eddy-simulation mode. The high resolutions also lead to a requirement for a fine temporal resolution to avoid numerical instabilities. For the case considered, where $L_c/L = 0.36$ and $h_c/H = 0.33$, it appears that a horizontal resolution of $0.024\,L$ ($0.066\,L_c$, 2 m for this case) and a vertical resolution of 0.1 to $0.2\,h_c$ (1 to 2 m for this case) were appropriate to reproduce the flow over a forested ridge using a canopy model with vertical extent. Further research will be required to determine the sensitivity of this canopy model to a wider range of hill geometries, canopy properties and extents. However, this will require considerably more experimental data on canopy flows in complex terrain to be collected. While there is currently insufficient data to carry out such research, the benefits of using a canopy model over the roughness-length parameterisation are clear.

Given that the canopy model can provide much better approximation of idealised flows like those simulated in Sect. 3, it was of interest to explore whether such benefits could be transferred in to numerical simulations of a real-world case study at coarser horizontal and vertical resolution. In Sect. 4 this was tested against a case study of perpendicular stable flow over an extensively forested double-ridge valley system. The use of a vertically resolved canopy model in numerical simulations provided significant improvements over the use of standardised, land use category dependent surface roughness. The velocity of the flow in the across-valley and vertical directions were reproduced significantly more accurately by the canopy model near the surface. The improvement in the accuracy of reproducing wind velocity variances and momentum fluxes is less clear. Although the simulations using a canopy model had a magnitude of TKE closer to that seen in the measurements than the surface roughness case, none of the simulations reproduced the same magnitude of TKE measured at the downstream ridge.

The wind field well above the ridge-tops and the properties of the flow near the surface at the flux towers furthest downstream were very similar regardless of the method used to represent the forest canopy. While this indicates that the representation of the canopy may be less important for larger scale simulations with coarser resolution, the canopy model provided more accurate reproduction of the flow within the valley. One of the main deficiencies of using surface roughness to represent the canopy was insufficient friction at the surface, much the same as the idealised case simulated in Sect. 3. The wind speeds near the surface were much more accurately reproduced when using a canopy model due to the additional friction of the vertically resolved canopy. With increasing height

the influence of this drag reduces and more than $60\,\mathrm{m}$ above the ground the wind speeds were over-predicted regardless of the method used to represent the canopy. The across-valley wind speed, TKE and fraction of time that reversed flows are present for the canopy model cases tended to lie somewhere between the results of the simulations using a roughness length and the measurements. Simulations using a canopy model were significantly better at reproducing the recirculation zones that occur downstream of the ridge-tops. Very little recirculation was seen when the canopy was represented only by an increased roughness length at the surface, with the flow remaining attached to the upstream of the two ridges at all times. The extent of the recirculation zones were much better reproduced in simulations using a canopy model. The frequency of flow reversal decreased more rapidly with height than was seen in the measurements, but near the ground the canopy model provided results in good agreement with the measurements.

The other aim of this study was to determine whether using high-resolution data for the height and density of the canopy cover at the site could produce better results in simulations than those where the canopy properties were set using lower resolution land use categories. While these two different methods of representing the canopy modified the flow over the valley differently, the higher-resolution canopy data did not provide a more accurate reproduction of the measured flow. It was however found that simulating a canopy with more variable height and density tends to produce less turbulence immediately above the canopy than a canopy with constant height and density. Over a canopy of constant height a shear layer develops at the top of the canopy, but this is distorted by a more variable canopy and the reduction in shear leads to less turbulence above the canopy.

The different representations of the canopy do not tend to have as much of an impact on the mean flow above. The results of the simulation using high-resolution canopy data were often more in line with those of the simulations using surface roughness to represent the canopy. This is likely because the lowest grid levels were approximately $6\,\mathrm{m}$ tall and so regions of canopy shorter than this height were only represented at the bottom level of the simulations. Assigning canopy properties based on land use categories therefore provides significant benefits over a roughness-length approach to representing the surface vegetation and is equivalent to using more high resolution input, at least for the case considered. This was true even though the vertical resolution of these simulations was 0.2 to 0.5 of the canopy height, which might previously have been considered insufficient to reproduce the dynamics of the flow around a canopy accurately. It is possible that a finer resolution near the surface could lead to better results for the high-resolution canopy data case, but increasing the vertical resolution was not possible without the simulations becoming unstable. Whether or not this is the case, the canopy model was found to provide significantly more accurate reproduction of the flow over this double-ridge system than default surface-roughness based methods.

While the canopy model applied here has been shown to be more effective, it did require small spatial resolution and hence small time steps to avoid numerical instabilities forming in simulations. The code that handles the canopy model is not hugely complex and should not add greatly to computation time if these instabilities could be diagnosed and avoided. With further investigation

it may have been possible to rectify this, perhaps by reducing canopy height and/or density at the edges of patches of forest to smooth the transition between free air and the canopy momentum sink. However, this would also change the dynamics and could lead to less accurate reproduction of the flow in and around the canopy. Another feature of the model that requires more testing is the effectiveness of the model over standard methods when lower resolutions are used. The data presented in Sect. 3 and 4 was taken from domains with resolutions no larger than $10\,\mathrm{m}$. In Sect. 4.10 the resolution is explored at a basic level and it appears that the model still provides good results at a resolution of $50\,\mathrm{m}$, at least for the case considered. Numerical weather prediction simulations are often carried out at resolutions on the order of hundreds or thousands of metres. So, if the model is to be used in such cases then understanding the effects it has at those resolutions will be important.

As the canopy model provides the most significant improvements near the surface, its use is advantageous to wind energy site selection and forestry professionals. The more accurate reproduction of the flow within the valley studied in Sect. 4 also suggests that a canopy model might be important when investigating air quality in valleys for processes such as cold air pooling. It would be of interest to study the implications of using a canopy model in numerical simulations of a more complicated valley system, if such data were available for comparison. However, there is some difficulty in disentangling the impact of the terrain on the flow from that of the canopy. Wind-tunnel experiments are often carried out using a single artificial canopy and hill geometry and inter-comparison between such experiments is difficult given the range of scales and wind speeds used. A study comparing a range of hill geometries and canopy properties and distributions with consistent incoming flow properties would therefore be advantageous to develop the canopy model further. It would also be useful for a consistent canopy and hill structure to be tested under different inflow and stability conditions. Such experimental data could then be used to disentangle the effect of the terrain and the canopy on the flow. It could also be compared to simulations with a range of resolutions in the horizontal and vertical to determine the best configuration to balance processing time and accuracy of the results for different scales of terrain elements. While analytical and numerical systems are powerful tools, they are only possible if there is sufficient experimental data against which to compare their effectiveness under a range of different conditions.

SECTION 6

References

Weather research and forecasting model description, a. URL https://www.mmm.ucar.edu/weather-research-and-forecasting-model. Accessed on 22nd February 2018.

Weather research and forecasting model users site, b. URL http://www2.mmm.ucar.edu/wrf/users/. Accessed on 22nd February 2018.

R. S. Arthur, J. D. Mirocha, K. A. Lundquist, and R. L. Street. Using a canopy model framework to improve large-eddy simulations of the neutral atmospheric boundary layer in the weather research and forecasting model. *Monthly Weather Review*, 147(1):31–52, 2019. doi:10.1175/MWR-D-18-0204.1.

K. Ayotte, J. Finnigan, and M. Raupach. A second-order closure for neutrally stratified vegetative canopy flows. *Boundary-Layer Meteorology*, 90(2):189–216, 1999. doi:10.1023/A:1001722609229.

K. W. Ayotte. Computational modelling for wind energy assessment. *Journal of Wind Engineering and Industrial Aerodynamics*, 96:1571–1590, 2008. doi:10.1016/j.jweia.2008.02.002.

J. Bastin, Y. Finegold, C. Garcia, D. Mollicone, M. Rezende, D. Routh, C. M. Zohner, and T. W. Crowther. The global tree restoration potential. *Science*, 365:76–79, 2019a. doi:10.1126/science.aax0848.

J.-F. Bastin, Y. Finegold, C. Garcia, D. Mollicone, M. Rezende, D. Routh, C. M. Zohner, and T. W. Crowther. The global tree restoration potential. *Science*, 365:76–79, 2019b. doi:10.1126/science.aax0848.

S. Belcher, I. Harman, and J. Finnigan. The wind in the willows: Flows in forest canopies in complex terrain. *Annual Review of Fluid Mechanics*, 44(1):479–504, 2012. doi:10.1146/annurev-fluid-120710-101036.

S. E. Belcher and N. Wood. Form and wave drag due to stably stratified turbulent flow over low ridges. *Quarterly Journal of the Royal Meteorological Society*, 122:863–902, 1996. doi:10.1002/qj.49712253205.

S. E. Belcher, T. M. J. Newley, and J. C. R. Hunt. The drag on an undulating surface induced by the flow of a turbulent boundary layer. *Journal of Fluid Mechanics*, 249:557–596, 1993. doi:10.1017/S0022112093001296.

S. E. Belcher, J. J. Finnigan, and I. N. Harman. Flows through forest canopies in complex terrain. *Ecological Applications*, 18:1436–1453, 2008. doi:10.1890/06-1894.1.

J. V. Boussinesq. Essai sur la théorie des eaux courantes. *Mémoires présentés par divers savants à l'Académie des Sciences*, XXIII(1):1–680, 1877.

A. R. Brown, J. M. Hobson, and N. Wood. Large-eddy simulation of neutral turbulent flow over rough sinusoidal ridges. *Boundary-Layer Meteorology*, 98:411–441, 2001. doi:10.1023/A:1018703209408.

Y. Brunet, J. Finnigan, and M. Raupach. A wind tunnel study of air flow in waving wheat: Single-point velocity statistics. *Boundary-Layer Meteorology*, 70(1–2):95–132, 1994. doi:10.1007/BF00712525.

S. P. Burns, J. Sun, D. H. Lenschow, S. P. Oncley, B. B. Stephens, Y. Chuixiang, D. E. Anderson, J. Hu, and R. K. Monson. Atmospheric stability effects on wind fields and scalar mixing within and just above a subalpine forest in sloping terrain. *Boundary-Layer Meteorology*, 138:231–262, 2011. doi:10.1007/s10546-010-9560-6.

H. Charnock. Wind stress on a water surface. *Quarterly Journal of the Royal Meteorological Society*, 81(350):639–640, 1955. doi:10.1002/qj.49708135027.

X. Cheng, J. Gulliver, and D. Zhu. Application of displacement height and surface roughness length to determination boundary layer development length over stepped spillway. *Water*, 6(12):3888–3912, 2014. doi:10.3390/w6123888.

T. L. Clark and S. J. Mitchell. Three-dimensional simulations of air flow and momentum transfer in partially harvested forests. *Boundary-Layer Meteorology*, 125:505–524, 2007. doi:10.1007/s10546-007-9199-0.

C. J. Desmond, S. J. Watson, S. Aubrun, S. Ávila, P. Hancock, and A. Sayer. A study on the inclusion of forest canopy morphology data in numerical simulations for the purpose of wind resource assessment. *Journal of Wind Engineering and Industrial Aerodynamics*, 126:24–37, 2014. doi:10.1016/j.jweia.2013.12.011.

S. Dupont and Y. Brunet. Edge flow and canopy structure: A large-eddy simulation study. *Boundary Layer Meteorology*, 126:51–71, 2008a. doi:10.1007/s10546-007-9216-3.

S. Dupont and Y. Brunet. Influence of foliar density profile on canopy flow: A large-eddy simulation study. *Agricultural and Forest Meteorology*, 148:976–990, 2008b. doi:10.1016/j.agrformet.2008.01.014.

S. Dupont and Y. Brunet. Coherent structure in canopy edge flow: a large-eddy simulation study. *Journal of Fluid Mechanics*, 630:93–128, 2009. doi:10.1017/S0022112009006739.

S. Dupont, Y. Brunet, and J. Finnigan. Large-eddy simulation of turbulent flow over a forested hill: Validation and coherent structure identification. *Quarterly Journal of the Royal Meteorological Society*, 134(1):1911–1929, 2008. doi:10.1002/qj.328.

H. Fernando. Fluid dynamics of urban atmospheres in complex terrain. *Annual Review of Fluid Mechanics*, 42(1):365–389, 2010. doi:10.1146/annurev-fluid-121108-145459.

H. Fernando, J. Mann, J. Palma, J. Lundquist, R. Barthelmie, M. BeloPereira, W. Brown, F. Chow, T. Gerz, C. Hocut, P. Klein, L. Leo, J. Matos, S. Oncley, S. Pryor, L. Bariteau, T. Bell, N. Bodini, M. Carney, M. Courtney, E. Creegan, R. Dimitrova, S. Gomes, M. Hagen, J. Hyde, S. Kigle, R. Krishnamurthy, J. Lopes, L. Mazzaro, J. Neher, R. Menke, P. Murphy, L. Oswald, S. Otarola-Bustos, A. Pattantyus, C. Rodrigues, A. Schady, N. Sirin, S. Spuler, E. Svensson, J. Tomaszewski, D. Turner, L. van Veen, N. Vasiljevic, D. Vassallo, S. Voss, N. Wildmann, and Y. Wang. The perdigão: Peering into microscale details of mountain winds. *Bulletin of the American Meteorological Society*, 2019. doi:10.1175/BAMS-D-17-0227.1.

J. Finnigan. Turbulence in plant canopies. *Annual Reviews of Fluid Mechanics*, 32:519–571, 2000. doi:10.1146/annurev.fluid.32.1.519.

J. Finnigan and S. Belcher. Flow over a hill covered with a plant canopy. *Quarterly Journal of the Royal Meteorological Society*, 130(596):1–29, 2004. doi:10.1256/qj.02.177.

J. Finnigan and Y. Brunet. *Wind and Trees: Turbulent airflow in forests on flat and hilly terrain*. Cambridge University Press, Cambridge, UK, 1995.

J. J. Finnigan and D. Hughes. A wind tunnel study of stably stratified flow on a ridge covered with a tall plant canopy, 2008.

J. J. Finnigan and P. J. Mulhearn. Modelling waving crops in a wind tunnel. *Boundary-Layer Meteorology*, 14:253–277, 1978. doi:10.1007/BF00122623.

N. J. Froelich, C. S. B. Grimmond, and H. P. Schmid. Nocturnal cooling below a forest canopy: Model and evaluation. *Agricultural and Forest Meteorology*, 151:957–968, 2011. doi:10.1016/j.agrformet.2011.02.015.

A. J. Garrett. Drainage flow prediction with a one-dimensional model including canopy, soil and radiation parameterizations. *Journal of Applied Meteorology and Climatology*, 22:79–91, 1983. doi:10.1175/1520-0450(1983)022<0079:DFPWAO>2.0.CO;2.

J. A. Gillies, W. G. Nickling, and J. King. Drag coefficient and plant form response to wind speed in three plant species: Burning bush (euonymus alatus), colorado blue spruce (picea pungens glauca.), and fountain grass (pennisetum setaceum). *Journal of Geophysical Research: Atmospheres*, 107:4760, 2002. doi:10.1029/2001JD001259.

E. Grant, A. Ross, B. Gardiner, and S. Mobbs. Field observations of canopy flows over complex terrain. *Boundary-Layer Meteorology*, 156(2):231–251, 2015. doi:10.1007/s10546-015-0015-y.

E. Grant, A. Ross, and B. Gardiner. Modelling canopy flows over complex terrain. *Boundary-Layer Meteorology*, 161(3):417–437, 2016. doi:10.1007/s10546-016-0176-3.

F. Hosoi and K. Omasa. Estimating vertical leaf area density profile of tree canopies using three-dimensional portable lidar imaging. *Proceedings of the ISPRS Workshop Laser-scanning 09, Paris, France*, 38:152–157, 2009.

J. C. R. Hunt, S. Leibovich, and K. J. Richards. Turbulent shear flows over low hills. *Quarterly Journal of the Royal Meteorological Society*, 114:1435–1470, 1988. doi:10.1002/qj.49711448405.

P. S. Jackson and J. C. R. Hunt. Turbulent wind flow over a low hill. *Quarterly Journal of the Royal Meteorological Society*, 101:929–955, 1975. doi:10.1002/qj.49710143015.

J. Kaimal and J. Finnigan. *Atmospheric boundary layer flows. Their structure and measurements.* Oxford University Press, New York, USA, 1994.

G. Katul, L. Mahrt, D. Poggi, and C. Sanz. One- and two-equation models for canopy turbulence. *Boundary-Layer Meteorology*, 113(1):81–109, 2004. doi:10.1023/B:BOUN.0000037333.48760.e5.

Y. Kitamura. Estimating dependence of the turbulent length scales on model resolution based on a priori analysis. *Journal of the Atmospheric Sciences*, 72(1):750–762, 2014. doi:10.1175/JAS-D-14-0189.1.

M. H. Kobayashi, J. C. F. Pereira, and M. B. B. Siqueira. Numerical study of the turbulent flow over and in a model forest on a 2d hill. *Journal of Wind Engineering and Industrial Aerodynamics*, 53:357–374, 1994. doi:10.1016/0167-6105(94)90091-4.

B. Lalic and D. Mihailovic. An empirical relation describing leaf-area density inside the forest for environmental modeling. *Journal of Applied Meteorology*, 43(4):641–645, 2004. doi:10.1175/1520-0450(2004)043<0641:AERDLD>2.0.CO;2.

B. Launder and D. Spalding. *Mathematical models of turbulence*. Academic Press, London, UK, 1972.

B. Launder and D. Spalding. The numerical computation of turbulent flows. *Computational Methods in Applied Mechanical Engineering*, 3(2):269–289, 1974. doi:10.1016/0045-7825(74)90029-2.

A. Leonard. Energy cascade in large-eddy simulations of turbulent fluid flows. In F. Frenkiel and R. Munn, editors, *Turbulent Diffusion in Environmental Pollution*, volume 18 of *Advances in Geophysics*, pages 237–248. Elsevier, 1975. doi:10.1016/S0065-2687(08)60464-1.

Y. R. Li, X. C. Wang, C. K. Wang, F. Liu, and Q. Z. Zhang. Spatial variation in diurnal courses of stem temperature of betula platyphylla and fraxinus mandshurica and its influencing factors. *Chinese Journal of Applied Ecology*, 28:3197–3207, 2017. doi:10.13287/j.1001-9332.201710.008.

Z. Liu, T. Ishihara, X. He, and H. Niu. Les study on the turbulent flow fields over complex terrain covered by vegetation canopy. *Journal of Wind Engineering and Industrial Aerodynamics*, 155: 60–73, 2016. doi:10.1016/j.jweia.2016.05.002.

J. Lumley. Computational modeling of turbulent flows. *Advances in Applied Mechanics*, 18(1): 123–176, 1978. doi:10.1016/S0065-2156(08)70266-7.

Y. Ma and H. Liu. An advanced multiple-layer canopy model in the wrf model with large-eddy simulations to simulate canopy flows and scalar transport under different stability conditions. *Journal of Advances in Modeling Earth Systems*, 11(7):2330–2351, 2019. doi:10.1029/2018MS001347.

P. Martano. Estimation of surface roughness length and displacement height from single-level sonic anemometer data. *Journal of Applied Meteorology*, 39:708–715, 1999.

P. Mason. On the parameterization of orographic drag. In *Seminar on Physical Parameterization for Numerical Models of the Atmosphere, 9-13 September 1985*, volume 2, pages 139–166, Shinfield Park, Reading, 1985. ECMWF, ECMWF. URL https://www.ecmwf.int/node/11010.

F. R. Menter. Two-equation eddy-viscosity turbulence models for engineering applications. *AIAA Journal*, 32(8):1598–1605, 1994. doi:10.2514/3.12149.

M. Meybeck, P. Green, and C. Vörösmarty. A new typology for mountains and other relief classes: An application to global continental water resources and population distribution. *Mountain Research and Development*, 21(1):34–45, 2001. ISSN 02764741, 19947151. URL http://www.jstor.org/stable/3674130.

A. S. Monin and A. M. Obukhov. Basic laws of turbulent mixing in the surface layer of the atmosphere. *Tr. Akad. Nauk SSSR Geofiz. Inst.*, 24:163–187, 1954. English translation by John Miller, 1959.

K. N. Musselman and J. W. Pomeroy. Estimation of needleleaf canopy and trunk temperatures and longwave contribution to melting snow. *Journal of Hydrometeorology*, 18:555–572, 2017. doi:10.1175/JHM-D-16-0111.1.

C. L. Navier. Sur les lois des mouvements des fluides, en ayant égard à l'adhésion des molecules. *Annales de Chimie et de Physique*, XIX(244), 1821.

C. L. Navier. Sur les lois du mouvement des fluides. *Mémoires de L'Académie Royale des Sciences de L'Institut de France*, VI(389), 1827.

H. G. Ouwersloot, A. F. Moene, and J. J. Attema. Large-eddy simulation comparison of neutral flow over a canopy: sensitivities to physical and numerical conditions, and similarity to other representations. *Boundary-Layer Meteorology*, 162:71–89, 2017. doi:10.1007/s10546-016-0182-5.

J. L. Palma and V. Batista. Perdigão: Leaf area index map in 2m resolution (2019 version), 2019a. URL 10.34626/uporto/382c-gh41. Dataset published 2021 via Faculty of Engineering, University of Porto. Accessed 3rd December 2019.

J. L. Palma and V. Batista. Perdigão: Canopy height model for 2017 vegetation height in 2m resolution (2019 version), 2019b. URL 10.34626/uporto/4x50-fr07. Dataset published 2021 via Faculty of Engineering, University of Porto. Accessed 3rd December 2019.

E. Patton. Turbulent flow over isolated ridges; influence of vegetation. 2006.

E. G. Patton and G. G. Katul. Turbulent pressure and velocity perturbations induced by gentle hills covered with sparse and dense canopies. *Boundary-Layer Meteorology*, 133:189–217, 2009. doi:10.1007/s10546-009-9427-x.

J. Pinard and J. Wilson. First- and second-order closure models for wind in a plant canopy. *Journal of Applied Meteorology*, 40(1):1762–1768, 2001. doi:10.1175/1520-0450(2001)040<1762:FASOCM>2.0.CO;2.

D. Poggi and G. G. Katul. Turbulent flows on forested hilly terrain: the recirculation region. *Quarterly Journal of the Royal Meteorological Society*, 133:1027–1039, 2007. doi:10.1002/qj.73.

L. Prandtl. 7. bericht über untersuchungen zur ausgebildeten turbulenz. *Zeitschrift für Angewandte Mathematik und Mechanik*, 5(2):136–139, 1925. doi:10.1002/zamm.19250050212.

C. P. Quine, M. P. Coutts, B. Gardiner, and D. G. Pyatt. Forests and wind: management to minimize damage. *Forestry Commission Bulletin*, 114:24, 1995.

M. Raupach, J. Finnigan, and Y. Brunet. Coherent eddies and turbulence in vegetation canopies: The mixing-layer analogy. *Boundary-Layer Meteorology*, 78(3–4):351–382, 1996. doi:10.1007/BF00120941.

M. R. Raupach, E. F. Bradley, and H. Ghadiri. A wind tunnel investigation into the aerodynamic effect of forest clearings on the nesting of abbott's booby on christmas island: Progress report on a study commissioned by the australian national parks and wildlife service, 1987.

O. Reynolds. Iv. on the dynamical theory of incompressible viscous fluids and the determination of the criterion. *Philosophical Transactions of the Royal Society of London. (A.)*, 186:123–164, 1895. doi:10.1098/rsta.1895.0004.

A. Ross and T. Baker. Flow over partially forested ridges. *Boundary-Layer Meteorology*, 146: 375–392, 2013. doi:10.1007/s10546-012-9766-x.

A. Ross and S. Vosper. Neutral turbulent flow over forested hills. *Quarterly Journal of the Royal Meteorological Society*, 131(609):1841–1862, 2005. doi:10.1256/qj.04.129.

A. N. Ross. Large-eddy simulations of flow over forested ridges. *Boundary-Layer Meteorology*, 128: 59–76, 2008. doi:10.1007/s10546-008-9278-x.

A. N. Ross. Scalar transport over forested hills. *Boundary-Layer Meteorology*, 141:179–199, 2011. doi:10.1007/s10546-011-9628-y.

A. N. Ross. Boundary-layer flow within and above a forest canopy of variable density. *Quarterly Journal of the Royal Meteorological Society*, 138(666):1259–1272, 2012. doi:10.1002/qj.989.

F. Schlegel, J. Stiller, A. Bienert, H.-G. Maas, R. Queck, and C. Bernhofer. Large-eddy simulation study of the effects on flow of a heterogeneous forest at sub-tree resolution. *Boundary-Layer Meteorology*, 154:27–56, 2015. doi:10.1007/s10546-014-9962-y.

R. H. Shaw and E. G. Patton. Canopy element influences on resolved- and subgrid-scale energy within a large-eddy simulation. *Agricultural and Forest Meteorology*, 115:5–17, 2003. doi:10.1016/S0168-1923(02)00165-X.

R. H. Shaw and U. Schumann. Large-eddy simulation of turbulent flow above and within a forest. *Boundary-Layer Meteorology*, 61:47–64, 1992. doi:10.1007/BF02033994.

R. H. Shaw, G. Den Hartog, and H. H. Neumann. Influence of foliar density and thermal stability on profiles of reynolds stress and turbulence intensity in a deciduous forest. *Boundary-Layer Meteorology*, 45:391–409, 1988. doi:10.1007/BF00124010.

W. C. Skamarock, J. B. Klemp, J. Dudhia, D. O. Gill, Z. Liu, J. Berner, W. Wang, J. G. Powers, M. G. Duda, D. M. Barker, and X. Y. Huang. A description of the advanced research wrf version 4. *NCAR Technical Note NCAR/TN-556+STR*, page 145, 2019. doi:10.5065/1dfh-6p97.

J. Smagorinski. General circulation experiments with the primitive equations. *Monthly Weather Review*, 91:99–164, 1963. doi:10.1175/1520-0493(1963)091<0099:GCEWTP>2.3.CO;2.

G. G. Stokes. *On the Theories of the Internal Friction of Fluids in Motion, and of the Equilibrium and Motion of Elastic Solids*, volume 1 of *Cambridge Library Collection - Mathematics*, pages 75–129. Cambridge University Press, 2009. doi:10.1017/CBO9780511702242.005.

H. Sun, T. L. Clark, R. B. Stull, and T. Andrew Black. Two-dimensional simulation of airflow and carbon dioxide transport over a forested mountain: Part i: Interactions between thermally-forced circulations. *Agricultural and Forest Meteorology*, 140(1):338–351, 2006. doi:10.1016/j.agrformet.2006.03.023.

H. Tan and S. Ling. *Quasi-steady micrometeorological Atmospheric Boundary Layer over a Wheat Field*. Therm Inc., Ithaca, New York, USA, 1960.

N. Tani. The wind on the cultivated field (in japanese, english summary. *Journal of Agricultural Meteorology*, 16(3):89–93, 1963. doi:10.2480/agrmet.16.89.

M. Tewari, W. Wang, J. Dudhia, M. A. LeMone, K. Mitchell, M. Ek, G. Gayno, J. Wegiel, and R. Cuenca. Implementation and verification of the united noah land surface model in the wrf model. *20th Conference on Weather Analysis and Forecasting/16th Conference on Numerical Weather Prediction*, pages 11–15, 2004.

M. Tischmacher and B. Ruck. Interaction of gusts and forest edges – an experimental wind-tunnel study. *Forestry: An International Journal of Forest Research*, 86(5):523–532, 2013. doi:10.1093/forestry/cpt029.

R. Treuhaft, G. Asner, B. Law, and S. Van Tuyl. Forest leaf area density profiles from the quantitative fusion of radarand hyperspectral data. *Journal of Geophysical Research*, 107(D21):4568, 2002. doi:10.1029/2001JD000646.

Z. Uchijima and J. Wright. An experimental study of air flow in a corn plant-air layer. *Bulletin of the National Institute of Agricultural Science*, 11(1):19–66, 1963.

A. Verhoef, K. McNaughton, and A. Jacobs. A parameterization of momentum roughness length and displacement height for a wide range of canopy densities. *Hydrology and Earth System Sciences*, 1(1):81–91, 1997. doi:10.5194/hess-1-81-1997.

J. Wagner, T. Gerz, N. Wildmann, and K. Gramitzky. Long-term simulation of the boundary layer flow over the double-ridge site during the perdigao 2017 field campaign. *Atmospheric Chemistry and Physics*, 2019. doi:10.5194/acp-19-1129-2019.

T. Watanabe. Large-eddy simulation of coherent turbulence structures associated with scalar ramps over plant canopies. *Boundary-Layer Meteorology*, 112:307–341, 2004. doi:10.1023/B:BOUN.0000027912.84492.54.

J. Wilson, J. Finnigan, and M. Raupach. A first-order closure for diturbed plant-canopy flows, and its application to winds in a canopy on a ridge. *Quarterly Journal of the Royal Meteorological Society*, 124(547):705–732, 1998. doi:10.1002/qj.49712454704.

N. Wood. The onset of separation in neutral, turbulent flow over hills. *Boundary-Layer Meteorology*, 76:137–164, 1995. doi:10.1007/BF00710894.

T. Xu, S. M. Bateni, S. A. Margulis, L. Song, S. Liu, and Z. Xu. Partitioning evapotranspiration into soil evaporation and canopy transpiration via a two-source variational data assimilation system. *Journal of Hydrometeorology*, 17:2353–2370, 2016. doi:10.1175/JHM-D-15-0178.1.

X. Xu, C. Yi, and E. Kutter. Stably stratified canopy flow in complex terrain. *Atmospheric Chemistry and Physics*, 15:7457–7470, 2015. doi:10.5194/acp-15-7457-2015.

T. Yamada. A numerical model study of turbulent airflow in and above a forest canopy. *Journal of the Meteorological Society of Japan. Ser. II*, 60:439–454, 1982. doi:10.2151/jmsj1965.60.1_439.

W. Yue, M. B. Parlange, C. Meneveau, W. Zhu, R. v. Hout, and J. Katz. Large-eddy simulation of plant canopy flows using plant-scale representation. *Boundary-Layer Meteorology*, 124:183–203, 2007. doi:10.1007/s10546-007-9173-x.